University of Nevada, Reno

Anisotropic Deformation and Failure in Magnesium Alloy

A dissertation submitted in partial fulfillment of the

requirements for the degree of

Doctor of Philosophy in Mechanical Engineering

by

Yuqian Wang

Dr. Yanyao Jiang/Dissertation Advisor

December 2021

THE GRADUATE SCHOOL

We recommend that the dissertation
prepared under our supervision by

YUQIAN WANG

entitled

Anisotropic Deformation and Failure in Magnesium Alloy

be accepted in partial fulfillment of the
requirements for the degree of

DOCTOR OF PHILOSOPHY

Yanyao Jiang, Ph.D.
Advisor

Matteo Aureli, Ph.D.
Committee Member

Pradeep Menezes, Ph.D.
Committee Member

Bin Li, Ph.D.
Committee Member

Dhanesh Chandra, Ph.D.
Graduate School Representative

David W. Zeh, Ph.D., Dean
Graduate School

December, 2021

Abstract

Magnesium (Mg) alloys are the lightest metallic materials that could be widely applied to load-bearing structural components. They are typically manufactured via two different forms: casted and wrought (rolled, extruded and forged). Wrought Mg alloys without casting defects possess superior mechanical properties to these of the casted counterparts. Due to their hexagonal closed-packed (HCP) crystal structure, Mg alloys have limited slip systems at room temperature. Twinning can be activated as an additional deformation mode to accommodate plastic deformation. Dislocation slips and twinning as well as their interactions result in some unique mechanical responses of Mg alloys under monotonic and cyclic loading. Moreover, for wrought Mg alloys, a strong basal texture is often introduced during the rolling and extrusion processes, leading to the *c*-axis of most grains being aligned perpendicular to the rolled direction (RD) or extrusion direction (ED). The strong texture and the pronounced variation of critical resolved shear stress (CRSS) of different deformation modes result in significant mechanical anisotropy of Mg alloys. The underlying deformation mechanisms stimulate profuse interests in both academia and industry. However, current state-of-the-art research lacks a systematic investigation of the anisotropic deformation and failure in Mg alloys. This dissertation aims to understand the monotonic deformation and fracture, cyclic deformation and fatigue behavior, as well as the associated orientation-dependent principal microscopic mechanisms.

In this study, monotonic tension, monotonic compression, and cyclic fully reversed strain-controlled tension-compression experiments were carried out on rolled AZ31B Mg alloy specimens taken from five different material orientations (θ = 0º, 22.5º, 45º, 67.5º and

90º) with respect to the rolled direction (RD). The deformation behavior was analyzed from the stress-strain response. Electron back-scattered diffraction (EBSD) analysis was performed to characterize the microstructural evolution and failure mechanisms.

The anisotropic fracture behavior of Mg alloys was explored for the first time by statistical slip trace analysis. Significant anisotropy is observed in the monotonic deformation and tensile fracture behavior. At the macroscopic scale, under tension at θ = 0º, 67.5º and 90º, a brittle-like fracture is shown where irregular-shaped surfaces composed of ridges and islands are observed. For tension at θ = 0º, a microstructural analysis in the vicinity of microcracks confirms that a crack forms at the tip and/or boundary of compression and compression-tension (C-T) double twins. For the cases of tension at θ = 67.5º and 90º, microcrack initiation is due to high-angle grain boundary cracking, which is likely caused by stress concentration due to impingements of none co-zone twin-twin boundaries and tertiary tension-compression-tension twins on the high-angle grain boundaries (HAGBs). In contrast, shear fracture displaying a relatively flat fracture surface is exhibited from tension at θ = 22.5º and 45º. A microstructural analysis reveals that fracture at these two material orientations is a result of localized shearing accommodated by basal slips from which both crack initiation and propagation are originated.

The detailed characteristic cyclic plastic deformation was investigated by performing fully reversed strain-controlled tension-compression cyclic experiments. Significant anisotropy is exhibited in cyclic plastic deformation. Cyclic hardening was observed for all five material orientations at a high strain amplitude. A particular focus is put on the elastic limit range, which represents the activation stress for basal slips or twinning/detwinning during cyclic loading. For the material orientation $\theta \neq 45º$, the cyclic

deformation exhibits a pronounced tension-compression asymmetry. The different deformation mechanism during the tension and compression reversals is intrinsically reflected by the evolution behavior of elastic limit range on the number of loading cycles and applied strain magnitude. The elastic limit range on the loading reversal which is favorable for twinning signifies the activation stress of basal slips and being independent on the loading cycles and the strain amplitude. In contrast, the value of elastic limit range on the loading reversals which is favorable for detwinning is closely related to the twin volume fraction at the peak stress prior to the loading reversal. A strong material dependence can be observed in the elastic limit range during cyclic loading, which reveals a highest value at $\theta = 0^{o}$ and lowest value at $\theta = 45^{o}$.

Unique deformation behavior can be captured during cyclic loading in the $\theta = 45^{o}$ material orientation. The values of elastic limit range on the tension and compression reversals are approximately identical irrespective of the number of loading cycles and loading magnitude. Twinning occurs in one group of grains and simultaneously detwinning occurs in another group of grains during loading and reversed loading. Low percentage of grains are favorable for twinning for the 45^{o} orientation comparing with the other material orientations.

Results obtained from fully reversed strain-controlled tension-compression fatigue experiments reveal the material orientation effect on the fatigue behavior. Fatigue lives range from few loading cycles to over 10^{6} cycles. The strain-life curves of all the material orientations form a relatively narrow band. The strain-life curve obtained from each material orientation is characterized with two distinct kink points which are closely associated with the dominating plastic deformation mechanisms, fatigue properties, and

fatigue cracking behavior. The RD specimens show the highest fatigue strength while the 45º specimens display the lowest fatigue strength among the five material orientations.

Based on the two kink points from the strain-life curves, three different strain amplitudes were prescribed for each material orientation. It is found that both the material orientation and the loading magnitude can affect the fracture features at the initiation and early-stage propagation region on the fracture surface. At the macroscopic scale, fatigue at θ = 0º (RD), 67.5º and 90º (ND) results in brittle-like fracture surfaces, whereas fatigue at θ = 22.5º and 45º displays shear cracking behavior at the local region. For θ = 0º (RD), 22.5º and 45º, both intergranular and transgranular crack growth modes exist irrespective of strain amplitudes. The mechanism of early-stage transgranular crack propagation is different at high and low strain amplitudes. When the strain amplitude is above the upper kink point, transgranular cracking is induced by both basal and non-basal slips. As for the strain amplitude below the upper kink point, transgranular cracking is only induced by basal slip. In contrast, for θ = 90º (ND) and 67.5º, grain boundary cracking is persistent under three different strain amplitudes. However, the early-stage microcrack propagation mode is dependent on the strain amplitude. Transgranular cracking induced by basal and non-basal slips only occurs when the strain amplitude is above the upper kink point.

Dedication

To my beloved family

Acknowledgements

I would like first to express my deepest respect, sincere gratitude, and special thanks to my major advisor, Professor Yanyao Jiang, for providing me the opportunity to become one of his research group and conduct this research. Over the past five years, his professional supervision, patient tutoring, and relentless support, raise me up and make this dissertation possible. He shows me what it means to be an excellent researcher who explores the unknow with enthusiasm, performs the experiments with meticulousness, and presents the results with integrity. I cannot forget the experience, skills, and knowledge I have gained from working with Dr. Jiang, which would be a precious asset in my future career.

Besides my advisor, I would like to thank the rest of my Ph.D. committee members: Prof. Bin Li, Prof. Dhanesh Chandra, Prof. Matteo Aureli and Prof. Pradeep Menezes, not only for their constructive advice and insightful guidance during my Ph.D. study, but also for their inspiring questions and critical comments on my dissertation. Their wisdom shaped my mind and broadened my perspective in my research.

My sincere thanks are also given to Dr. Qin Yu and Dr. Duke Culbertson, for their constructive suggestion and unyielding encouragements. I cannot forget the help they provided throughout my Ph.D. study. I would like to thank my fellow lab mate, Luiz Carneiro, for the stimulating discussions. Additionally, I thank Dr. Joel Desormeau for his assistance in the operation of the SEM and EBSD. As a teaching assistant, I would like to thank the machine shop technicians, Mr. Brian Nagy for his help in machining specimens, and Mr. Seth Draper for helping me set up the labs.

My deep gratitude also goes to my dear friends. Thanks to my friend Dr. Gao for her sustainable encouragement and comfort when I feel frustrated. Thanks to my two lovely roommates, Carotte and Rav, for the constant companionship and joy they offered me during my living in Reno.

Last but not least, I would like to express the deepest appreciation to my dear family. Growing up in a family of engineers helps me strike up the passion and dream for mechanical engineering. The unconditional love and support from my parents endow me the freedom, courage and faith to pursue this dream. They encourage and comfort but never steer. They are my heroes and the best parents a daughter could have. With all the supports from family and friends, I will keep striving for realizing the value of my life with full enthusiasm and faith.

Table of Contents

List of Tables

List of Figures

1 Introduction

Magnesium (Mg) alloys are the lightest structural metallic materials serving as the third-most-used structural metal following iron and aluminum alloys [1]. The density of Mg is 1.74g/cm^3, which is only 22% as that of iron (7.87g/cm^3) and 64% of aluminum (2.7g/cm^3) [2], endowing the Mg alloys remarkably high specific strength. Furthermore, wrought Mg alloys exhibit multiple superior physical properties such as excellent thermal conductivity [3], good recyclability [4], excellent damping capability, desirable biocompatibility [5], and high strength-to-weight ratio [6]. All of these characteristics make wrought Mg alloys promising lightweight structural materials in the applications of aircraft, automotive, bio-implants, and electronics industries [7–9].

Even though wrought Mg alloys show significant potential for a variety of applications, they have not been widely utilized due to several drawbacks. Mg alloys are typically manufactured via two different forms: casted and wrought (rolling, extrusion and forging). Wrought Mg alloys without casting defects possess superior mechanical properties to these of the casted counterparts [5,10]. However, wrought Mg alloys exhibit some difficulties related to its mechanics, such as limited ductility and poor formability at room temperature[1], due to the hexagonal close-packed (HCP) crystal structure. Unlike the body-centered cubic (BCC) and face-centered cubic (FCC) metals with high symmetrical crystal structures that can accommodate strain in any directions, Mg alloys with an HCP crystal structure have limited number of slip systems at room temperature. Twinning can be activated as an additional deformation mechanism to accommodate the local plastic deformation.

For wrought Mg alloys, rolling and extrusion processes often introduce strong basal texture, in which the *c*-axis of most grains are aligned perpendicular to the rolling direction (RD) or extrusion direction (ED). The strong texture, together with the pronounced variation of critical resolved shear stress (CRSS) of different deformation modes, brings about significant mechanical anisotropy of Mg alloys. Dislocation slips and twinning, as well as their interactions, result in some unique mechanical responses under monotonic and cyclic loading, such as anisotropic plastic hardening [11], tension-compression yielding asymmetry [12], and low ductility [13]. A comprehensive understanding of the unusual plastic behavior of wrought Mg alloys is still lacking, which significantly hinders the development and applications of Mg alloys. On the other hand, the compelling need for lightweight and energy-saving materials continues to drive the research and development of Mg alloys.

1.1 Significance and Motivation

The structural components are inevitably subjected to mechanical loading, which will induce failure of the material. Wrought Mg alloys display pronounced anisotropy in their room-temperature mechanical responses. Therefore, for applications to reliable and durable loading-bearing Mg structural components, it is necessary to systemically investigate the inelastic deformation, fracture behavior, and various fatigue-related properties especially their reliance on material orientation.

Over the last three decades, the cyclic deformation and fatigue properties of Mg alloys have been extensively studied. However, investigations regarding the cyclic deformation mechanisms in Mg alloys are qualitatively at the macroscale. Some detailed characteristics

used to describe cyclic plasticity, such as the elastic limit ranges and inflection strain ranges, have not been well explored. Moreover, very few studies have been focused on the anisotropic fatigue properties of Mg. Different observations of fracture mechanisms were made in wrought Mg alloys. The conclusions drawn from prior work are uncompleted since the experiments were limited to monotonic or cyclic loading with specimen orientated either along the RD, the ED, or the transverse direction (TD). The dissimilarity of the loading direction with respect to the texture has not been taken into consideration. When it comes to fatigue damage, there is no clear picture showing the influence of material orientation and loading magnitude on the fatigue damage mechanisms in Mg.

1.2 Research Objectives and Outlines

With the research motivation discussed above, the current research aims to investigate the anisotropic fracture behavior, cyclic deformation, fatigue, and the associated principal microscopic mechanisms. A clear picture of deformation and failure of Mg will be obtained, with emphases on the reliance of material orientation. The following goals were set for this study:

1) Exploring the anisotropic static behavior and the related deformation process in a rolled Mg alloy.
2) Exploring the anisotropic fracture behavior and the associated micro-mechanism under monotonic tension.
3) Analyzing the micro-mechanism responsible for the anisotropic cyclic deformation. Some important characteristics, such as the elastic limit ranges and the inflection strain ranges will be explored.

4) Understanding the anisotropic fatigue behavior of a rolled Mg alloy at different loading magnitudes and the material orientation effect on the macroscopic cyclic stress-strain response.
5) Clarifying the micro-mechanisms associated with the fatigue damage.

To achieve these goals, research efforts were put into two interrelated parts: mechanical experiments and microscopic characterization. The material used throughout the study is a hot rolled AZ31B (Mg-3Al-1Zn) Mg alloy plate. The static properties and deformation were determined by conducting monotonic tension and monotonic compression experiments. The macroscopic profiles of the fracture surfaces after monotonic tension experiments were obtained by using optical microscopy (OM). The microstructure in the vicinity of the microcracks was characterized by using a field emission scanning electron microscope (SEM) and electron backscattered diffraction (EBSD) scanning. Fully reversed strain-controlled tension-compression fatigue experiments were conducted to investigate the fatigue properties and cyclic deformation behavior. The detailed crystallographic analysis were studied to enlighten the mechanisms of fatigue damage.

The content of the dissertation is divided into seven parts:

1. The first part, Chapter two, reviews the fundamental information about Mg including crystallography, primary deformation mechanics, and their effects on the material's mechanical response. The current stage of the art of fracture, cyclic deformation and fatigue in Mg is also described in Chapter two.
2. The second part, Chapter three, introduces the specimen preparation and mechanical experiments, as well as the microstructure characterization procedure.

3. The third part, Chapter four, explores the fracture behavior under monotonic tension. The effects of material orientation on the static properties, deformation evolution, and macroscopic fracture are investigated. Examinations into the micro-mechanisms associated with anisotropic fracture behavior are discussed.
4. The fourth part, Chapter five, investigates the cyclic deformation under fully reversed strain-controlled tension-compression fatigue experiments. Macroscopic cyclic stress-strain responses are reported. The detailed characteristics of cyclic deformation, such as elastic limit range and inflections train ranges are explored. The results obtained from testing 45º material orientation are further discussed.
5. The fifth part, Chapter six, studies the anisotropic fatigue behavior and fatigue damage mechanisms. The influence of material orientation and loading magnitude on fatigue crack initiation and early-stage propagation are investigated.
6. The sixth part, Chapter seven, summarizes the conclusions of the research.

2 Literature Review

2.1 Plastic Deformation in Magnesium

2.1.1 Slips

Studies have been carried out to investigate the activated slip system in Mg and its alloys [14–17]. Slip modes which commonly observed in Mg at room temperature are $\langle 11\bar{2}0\rangle(\langle a\rangle)$ slip on the $\{0001\}$ basal plane, $\langle 11\bar{2}0\rangle(\langle a\rangle)$ slip on the $\{10\bar{1}0\}$ prismatic plane, $\langle 11\bar{2}0\rangle(\langle a\rangle)$ slip on the $\{10\bar{1}1\}$ first-order pyramidal plane, together with the $\langle 11\bar{2}3\rangle(\langle c+a\rangle)$ slip on the $\{10\bar{1}2\}$ second-order pyramidal plane. The slip direction and slip plane are illustrated in Fig. 2.1 for each slip system. The critical resolved shear stress (CRSS) with the slip direction and slip plane for each slip system are summarized in Table 1.

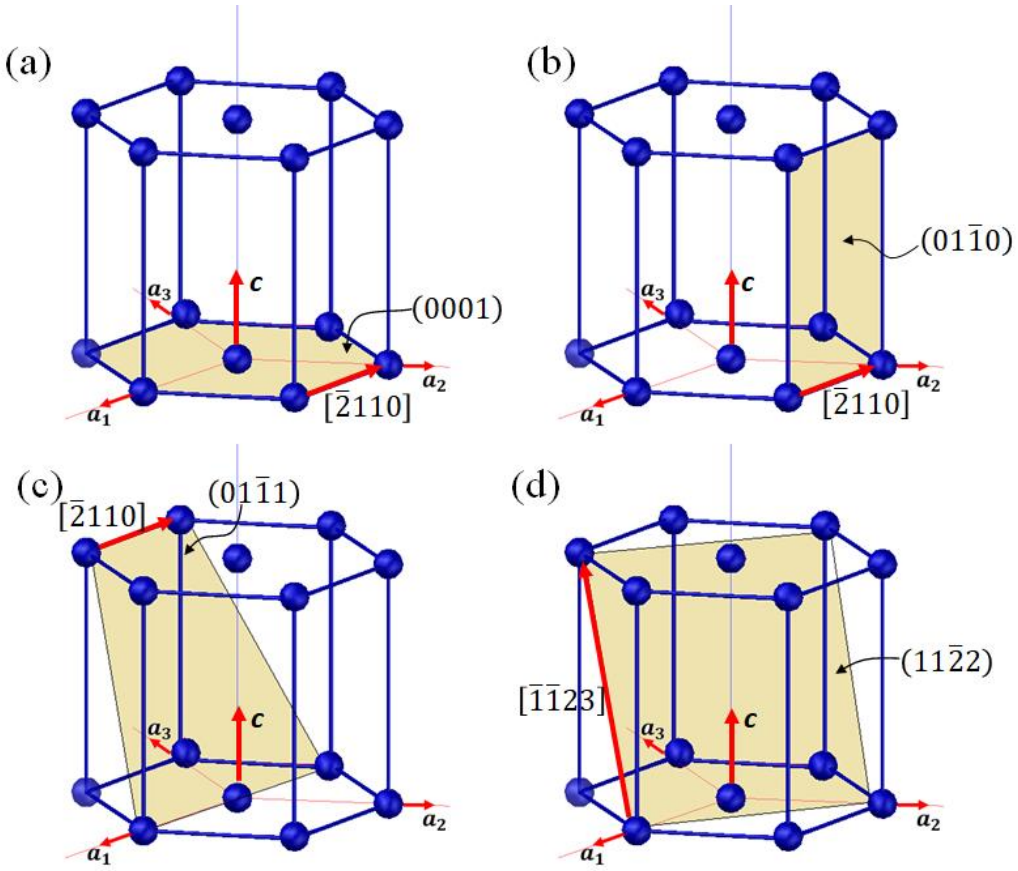

Fig. 2.1: Slip modes in Mg: (a) basal <a> slip, (b) prismatic <a> slip, (c) first-order pyramidal <a> slip and (d) second-order pyramidal <c+a> slip.

Table 1 Slip systems in Mg.

Slip system	Slip plane	Slip direction	Burgers vector	Number of independent slip systems	CRSS(MPa) at room temperature	Reference
Basal	$\{0001\}$	$\langle 11\bar{2}0\rangle$	$\langle a\rangle$	2	0.45-1.07	[18–22]
Prismatic	$\{10\bar{1}0\}$	$\langle 11\bar{2}0\rangle$	$\langle a\rangle$	2	8-39.2	[23–25]
Pyramidal	$\{10\bar{1}1\}$	$\langle 11\bar{2}0\rangle$	$\langle a\rangle$	4	0.51-3.92	[19,20]
Second-order pyramidal	$\{10\bar{2}2\}$	$\langle 11\bar{2}3\rangle$	$\langle c+a\rangle$	5	40	[26]

Figs. 2.1a-c show that the basal $\langle 11\bar{2}0\rangle$(<a>), prismatic $\langle 11\bar{2}0\rangle$(<a>) and first-order pyramidal $\langle 11\bar{2}0\rangle$(<a>) slip systems only allow for plastic accommodation on the basal plane. In order to accommodate the strain along *c*-axis, the second-order pyramidal

$\langle 11\bar{2}3\rangle$(<c+a>) slip needs to be activated. However, the CRSS for non-basal <c+a> slip is much higher than that for the basal slip at room temperature. Tension twinning is usually activated instead of the non-basal <c+a> slip to accommodate the deformation along the *c*-axis.

2.1.2 Twinning

In addition to dislocation slips, twinning is an important deformation mode to accommodate the plastic deformation in Mg alloys. The most commonly observed twinning modes in Mg alloys at room temperature are $\{10\bar{1}2\}\langle\bar{1}011\rangle$ tension (or extension) twinning and $\{10\bar{1}1\}\langle10\bar{1}\bar{2}\rangle$ compression (or contraction) twinning. The twinning plane and twinning direction are illustrated in Fig. 2.2. The twinning plane and twinning direction as well as their CRSS are listed in Table 2.

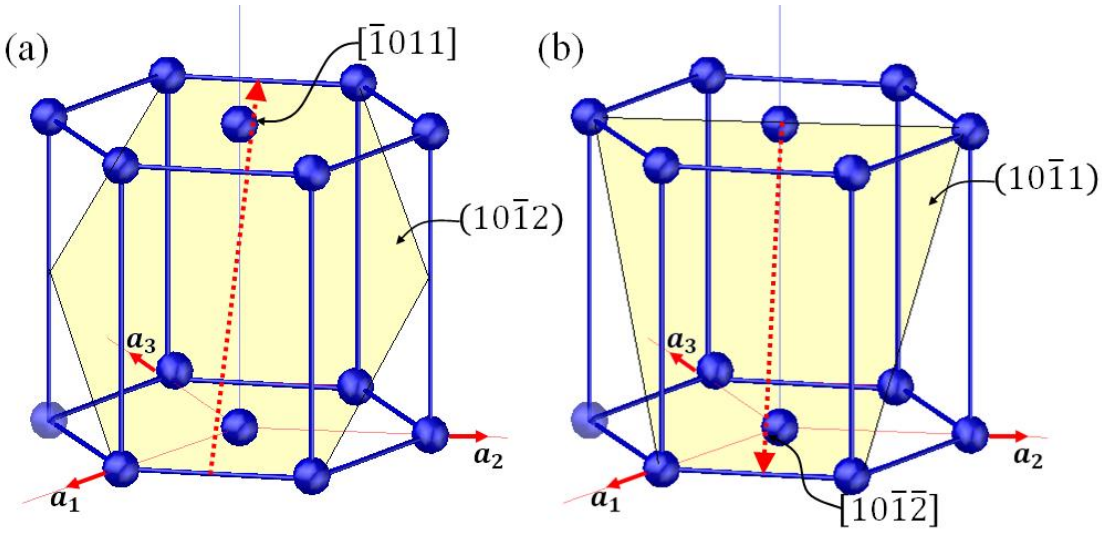

Fig. 2.2: Twinning elements for two primary twinning modes in Mg: (a) $\{10\bar{1}2\}\langle\bar{1}011\rangle$ tension twin and (b) $\{10\bar{1}1\}\langle10\bar{1}\bar{2}\rangle$ compression twin.

Table 2 Twinning elements and CRSS values for tension twin and compression twin in Mg.

Twinning mode	Twinning plane	Twinning direction	Twinning shear	CRSS (MPa)	Reference
Tension twinning	$\{10\bar{1}2\}$	$\langle\bar{1}011\rangle$	0.129	2-5.5	[24] [27–29]
Compression twinning	$\{10\bar{1}1\}$	$\langle10\bar{1}\bar{2}\rangle$	0.138	75-130	[25][30]

When the loading direction favorable for the tension twins (tension along the c-axis of the matrix, or compression parallel to the basal plane) is reversed, the *c*-axis of tension twin domain can be reoriented to align with that of the matrix domain, which is commonly referred to as "detwinning." Both twinning and detwinning can play an important role on the mechanical performances of materials [31–33].

2.2 Current State-of-the-Art

For wrought Mg alloys, a strong basal texture is often resulted from the rolling and extrusion processes. The texture, coupled with the pronounced variation in the CRSSs for different deformation modes, leads to significant mechanical anisotropy of Mg alloys. The anisotropic mechanical properties of Mg alloys have been extensively documented with a concentration on the monotonic responses [34–47] and fatigue properties [48–67]. Fig. 2.3 represents the tensile and compressive stress-strain curves showing typical tension-compression asymmetry occurring when loaded along the RD and ND [51].

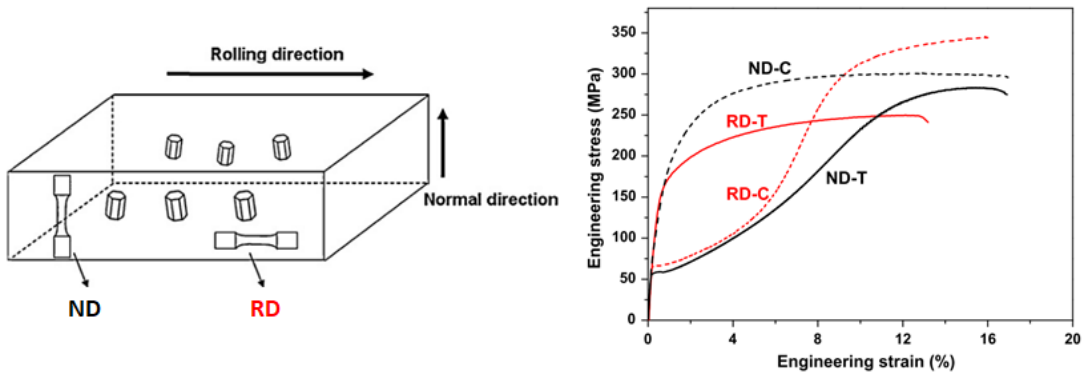

Fig. 2.3: Tensile and compressive engineering stress-engineering stain curves for NDT, NDC, RD-T and RD-C. ND-T and ND-C denote the tensile and compressive curves of a ND sample, respectively, while RD-T and RD-C are for a RD sample [51].

2.2.1 Fracture Behavior and Associated Micro-mechanism

In the last decades, few studies have been devoted to investigating the fracture behavior of Mg alloys along different loading directions with respect to the material texture [68–77]. Most of the prior work focused on studying the fracture behavior under monotonic or cyclic loading with the specimen oriented either along the RD, the ED, or the transverse direction (TD). Various fracture failures were reported depending on the specific material system and the loading direction. For instance, brittle fracture features with fine microscopic voids distributed on the fracture surface were reported in an AZ31B Mg alloy with tension along the RD [77] and in a Mg-5.72Al-2.96Zn-6.05Nd Mg alloy under tension along the ED [69]. However, for a pure Mg under tensile loading, the final fracture tends to show a shearing feature [73]. Similarly, typical shear fracture with different shearing angles was observed under in-plane compression applied to the AZ31B Mg specimens processed with various routes such as rolling, extrusion, and equal channel angular pressing (ECAP) [76].

Pertaining to the fracture mechanisms, the $\{10\bar{1}1\}$ compression twinning and $\{10\bar{1}1\}$-$\{10\bar{1}2\}$ compression-tension (C-T) double twinning were regularly recognized as the potential sites of failure initiation[37,47,76–82]. Once the $\{10\bar{1}1\}$ compression twins are nucleated, they immediately evolve into $\{10\bar{1}1\}$-$\{10\bar{1}2\}$ double twins through secondary $\{10\bar{1}2\}$ tension twins forming inside the primary $\{10\bar{1}1\}$ twins [75]. The misorientation angle/axis pair of $37.5^{\circ}/\langle 1\bar{2}10\rangle$ is commonly observed [78]. Large shear localization is induced within the double twins, which is evidenced by the observation of obvious surface steps[77]. The lack of stress relaxation for the large local shear in the C-T double twinning causes micro-crack formation, usually leading to brittle fracture features [80]. However, certain shear fracture features formed in fine grains were also found to be originated from double twinning [81].

Distinguished from the $\{10\bar{1}1\}$ compression twinning and $\{10\bar{1}1\}$-$\{10\bar{1}2\}$ C-T double twinning which is closely related to failure, the formation of $\{10\bar{1}2\}$ tension twin can accommodate the strain incompatibility caused by localized dislocation slips [83], without inducing visible surface relief [77]. From a study conducted using tensile experiments on a rolled AZ31B along the RD [81], it was reported that the severely strained grains accompanied $\{10\bar{1}1\}$-$\{10\bar{1}2\}$ double twins while the low-strain grains accompanied $\{10\bar{1}2\}$ tension twins. It was reported from another study on the same material by using notched compact specimen that $\{10\bar{1}2\}$ tension twinning helps to retard micro-void growth and coalescence [71]. A different study on Mg single crystal revealed that $\{10\bar{1}2\}$ tension twins can enhance the toughness in the notched fracture specimens [84].

Other than C-T double twinning, fracture in Mg alloys is affected by other microstructural features. For example, the deformation incompatibilities caused by basal slip/tension twin blocked at twin and grain boundaries were considered to nucleate microvoids [73]. The voids grow rapidly along a preferential direction, with final fracture showing a macroscopic shear process [73]. In addition, the second-phase particle was reported to play a detrimental role in the final fracture [72]. As a grain-scale factor, grain refinement can lead to reduced twinning activity and may result in a lower microvoid growth rate [74].

2.2.2 Cyclic Deformation and Fatigue of Mg Alloys

It has been well accepted that tension twin is strongly favorable for those grains with *c*-axes parallel to the tension direction or perpendicular to the compression direction. When the loading direction favorable for the tension twins is reversed, the *c*-axis of tension twin domain can be reoriented to align with that of the matrix domain, which is commonly referred to as "detwinning." Consequently, the twinning and detwinning may alternatively occur during the tension-compression fatigue loading. This pole nature of twinning and initial texture result in significant anisotropic mechanical behavior [39]. A great number of studies were conducted to understand the cyclic deformation and fatigue behavior of Mg alloys [33,49,56,57,60,62,63,65,85–99], with respect to strain amplitude [93,100–102], strain ratio [50], and strain rate [49]. It was established that both the material orientation and the loading magnitude play a significant role in the cyclic deformation and fatigue properties for wrought Mg alloys [48,51–55,58,59,61,64–67,93,103–111].

Effect of loading magnitude on cyclic deformation and fatigue:

The loading magnitude can significantly affect the cyclic plastic deformation, which is further macroscopically reflected by the fatigue properties. The twinning-detwinning process dominates plastic deformation at higher strain amplitudes, whereas dislocation slips dominate the plastic deformation at lower strain amplitudes [88,112,113]. In terms of fatigue behavior, it was reported in earlier studies of a wrought Mg alloy that the strain-life fatigue curve exhibited a smooth transition from the LCF regime to the high cycle fatigue (HCF) regime [87,98,112,114,115]. Regarding the fundamental fatigue mechanism, Matsuzuki and Horibe first observed that the fatigue data of an extruded AZ31 alloy exhibited a bilinear tendency in the Manson–Coffin curve [116], suggesting twinning–detwinning activity dominated plastic deformation at higher strain amplitudes and dislocation slip dominated plastic deformation at lower strain amplitudes. Recent studies on several Mg alloys indicate that there exist two distinguishable kink points in the strain-life fatigue curve from the ultra-low cycle fatigue regime to the HCF regime [117,118]. These two kink points divide the cyclic deformation performance of Mg alloys into three different mechanisms, being associated with a different degree of influence of twinning-detwinning deformation on fatigue [117]. When the strain amplitude is below the lower kink point, dislocation slips lead to fatigue failure during cyclic loading with no persistent twinning-detwinning. When the strain amplitude is above the lower kink point, sustainable twinning-detwinning occurs during the entire cyclic loading history. Detectable kink points in the fatigue curves of an extruded Mg alloy under combined axial-torsion loading show the stress state influence on twinning-detwinning deformation and fatigue [119].

Effect of material orientation on cyclic deformation and fatigue:

The loading direction with respect to the material orientation can intrinsically determine the twinning-detwinning process and significantly influence the cyclic plastic deformation behavior of Mg alloys. For example, Park et al. [51]investigated the cyclic plastic deformation behavior of a rolled AZ31B Mg alloy loaded along RD and ND. It was found that the asymmetric stress-strain hysteresis loops were caused by alternating twinning and detwinning behavior. Wu et al. [54] studied the same material loaded along RD, ND, and TD. It was observed that the different twinning-dewinning mechanisms under tension and compression are determined by the initial texture relative to the loading axis. Jordon et al. [109] studied the fatigue anisotropy of an extruded AZ61 Mg alloy loaded along the ED and TD. It was reported that more significant twinning-detwinning behavior can be observed when loading along the ED comparing with the TD. However, most of the studies only explored the macroscopic tension-compression asymmetry, and very few efforts have been put on the material orientation effect on the degree of involvement of twinning-detwinning activity during cyclic loading. Moreover, the investigations regarding the deformation mechanism in Mg alloys are studied qualitatively, and the detailed characteristics of the cyclic plastic deformation based on the associated micro-mechanisms have not been well investigated. Some important characteristics, such as the elastic limit ranges and the inflection strain ranges, which can represent the cyclic plastic deformation in a quantitative method, have not been well explored. The elastic limit ranges can demarcate the elastic and elastic-plastic deformation, and the inflection strain ranges can indicate the transition of deformation mechanism from twinning/detwinning to non-basal slips during cyclic loading. Dong et al. [120] studied the elastic limit range and inflection strain range for an extruded ZK60 magnesium alloy loaded along the ED. It was reported

that the elastic limit range is closely related to the material microstructure at the peak stress prior to the loading reversal.

Pertaining to the anisotropic fatigue behavior, there are limited experimental results related to the material orientation effect on the fatigue properties and some research results are inconsistent. For rolled Mg alloys under the fully reversed strain-controlled condition, the strain-life curve for specimen loading along the RD was slightly higher than that along the normal direction (ND) [54,59]. From different studies of a rolled AZ31B Mg alloy in the LCF regime [48,64], the strain-life curve of the ND specimens was higher than that of the RD specimens. It was also reported that the strain-life and the stress-life curves of the transverse direction (TD) were slightly higher than those of the RD [66,104]. For a study on a different rolled Mg alloy [105], WE43-T5, the strain-life curves were similar to those for the RD and TD in the LCF regime. Specimens taken from an AM30 Mg extrusion loading along the extrusion direction (ED) and TD exhibit similar strain-life curves in the LCF regime [67]. For an extruded AZ61 [109] and an extruded ZK60 [58], the strain-life curve of the ED was slightly higher than that of the TD.

On the fundamental fatigue damage mechanism of Mg, it was further revealed that the fatigue damage evolution in Mg or its alloys is closely related to the cyclic plastic deformation mechanism, namely twinning/detwinning and dislocation slips [121][122]. The relationship between the dominated deformation and the associated damage mechanisms was elucidated by Wang et al. [130], by conducting asymmetric stress-controlled cyclic tests on extruded AZ31B Mg alloy along the ED. When dislocation slip dominates the plastic deformation, only intergranular cracking exhibits without any twin-induced damage being observed. When the plastic deformation is dominated by

twinning/detwinning and dislocation slips, both intergranular cracking and transgranular cracking can be observed. The intergranular cracking is induced by the combined effect of <c+a> dislocation slips with tension twins, while the transgranular cracking is observed as twin boundary (TB) cracking [123]. With a different damage morphology from TB cracks, twin cracks were also identified when the strain amplitude is 1.00%, by performing fully reversed strain-controlled tension-compression experiments on the same material along the ED [122]. However, for a coarse-grained pure extruded Mg alloy with an average grain size larger than 100μm, Yu et al. [121] concluded that when loaded along the ED with strain amplitude of 0.2%, both intergranular and transgranular propagation modes were observed and early-stage transgranular propagation was induced by both bosal and non-basal slips. While under 1.00%, microcracks were incessantly initiated and inhabited on the grain and twin boundaries [121]. Xu et al. further implied that TB cracking is induced by the interaction between TBs and slip bands [124]. For a rare earth GW83 Mg alloy with a weak texture, the microcracks are initiated mainly at the GBs and predominately propagate along the GBs without any TB cracking when the strain amplitude is high [102]. For a rolled AZ31B in high-cycle fatigue (HCG) regime, Tokaji et al. observed that the crack initiation was in either transgranular or intergranular mode and both initiation modes occurred in nearly equal amounts [125]. Until now, only a few studies were conducted related to the material orientation effect on the material orientation effects on fatigue crack growth [126][127]. It was revealed that the material orientation has a significant influence on the fatigue crack growth rate and crack path.

Most of the cyclic experiments were conducted in two or three typical orientations: RD, TD and ND [48,51,53,54,59,64,66,103–108], and ED and TD for extruded

[52,53,58,65,67,109], and the loading direction is either approximately perpendicular or parallel to the *c*-axis. Despite the significant importance of considering the anisotropic behavior of Mg alloys, there is still a lack of detailed analysis of the plastic deformation characteristics, as well as the fatigue behavior on other material orientations.

2.3 Summary

The macroscopic features of deformation and failure of Mg alloys have been investigated through extensive experiments. A lack of consistency is likely caused by the microstructural diversity of different Mg alloys as well as the dissimilarity of the loading direction with respect to the texture. For the monotonic loading condition, no previous work has been carried out to study the anisotropic fracture behavior along various material orientations. Efforts made on the relationship between the macroscopic fracture behavior and the associated micro-mechanism are very limited. The material orientation plays a critical role in the cyclic deformation and fatigue properties in Mg. The anisotropic fatigue behavior was not comprehensively studied. There is still no quantitative investigation regarding the twinning-detwinning activity during the cyclic loading. The influences of the material orientation and the loading magnitude on the fatigue damage were not comprehensively investigated.

3 Experiments

3.1 Material and Specimen Preparation

3.1.1 Material

The material used in the study is a rolled AZ31B (Mg-3Al-1Zn) Mg alloy. The testing specimens were machined from the rolled plate with a thickness of 76.2 mm (Fig. 3.1c). The rolled direction, normal direction (thickness direction), and transverse direction are referred to as RD (0°), ND (90°), and TD, respectively. A cubic material block was cut from the middle layer of the rolled Mg plate for initial microstructure and texture analysis. Fig. 3.1a shows a three-dimensional stereography of initial microstructure revealed by electron backscatter diffraction (EBSD) scans on three orthotropic planes perpendicular to RD, ND, and TD, respectively. The Mg alloy consists of mostly equiaxed grains with an average grain size of approximately 50 μm, measured by using the Mean Lineal Intercept Method. The material displays a strong texture with the *c*-axis of most grains aligning parallel to the ND (Fig. 3.1b). No twins were detected in the initial microstructure before mechanical testing.

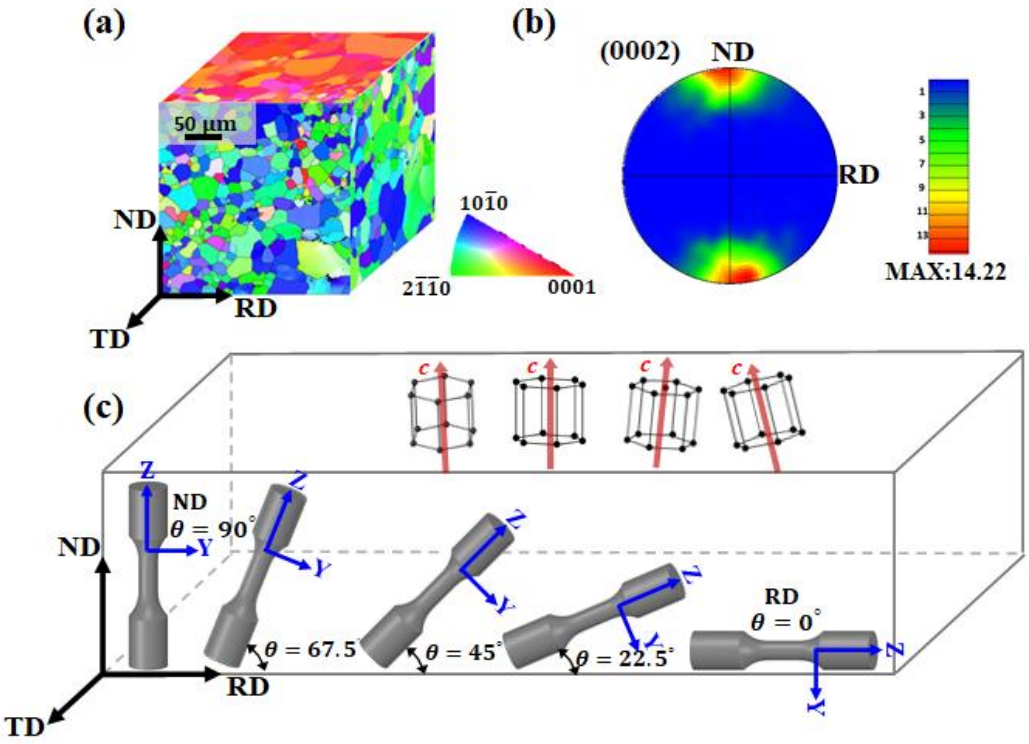

Fig. 3.1: Microstructure of the rolled AZ31B Mg alloy and testing specimens: (a) Three-dimensional stereograph of the as-rolled microstructure, (b) {0001} pole figure and (c) Cylindrical dog-bone shaped specimen with loading axes aligned at five different orientations with θ = 0º (RD), 22.5º, 45º, 67.5º and 90º (ND) relative to the rolled direction.

Solid cylindrical dog-bone shaped specimens were machined from the rolled plate with their loading axes (Z-axes) aligning, respectively, to θ = 0º (RD), 22.5º, 45º, 67.5º and 90º (ND) with respect to the RD (Fig. 3.1c) on the ND-RD plane. To facilitate discussion, the coordinate system XYZ is embedded with the testing specimen following the convention that the YZ plane is parallel to the ND-RD plane and the Z axis is along the axial direction of the specimen. The X-axis is along the TD.

3.1.2 Specimen Designs

Solid cylindrical specimens have a gage length of 14 mm and a diameter of 8.0 mm within the gage section. The schematic of the specimen with dimensions is shown in Fig. 3.2. For each specimen, the plane perpendicular to the TD is marked via a cut from the edge of the specimen along the TD direction, by approximately 0.5 mm. Specimens with a larger diameter of 10 mm are used for monotonic compression experiments as well as some cyclic loading experiments with low fatigue lives, to avoid buckling. The schematic illustration with dimensions of specimen for monotonic compression experiments is shown in Fig. 3.3. Prior to an experiment, the surface within the gage section of the testing specimen was finely polished by using silicon carbide papers with grit No. ranging from P400 up to P1200.

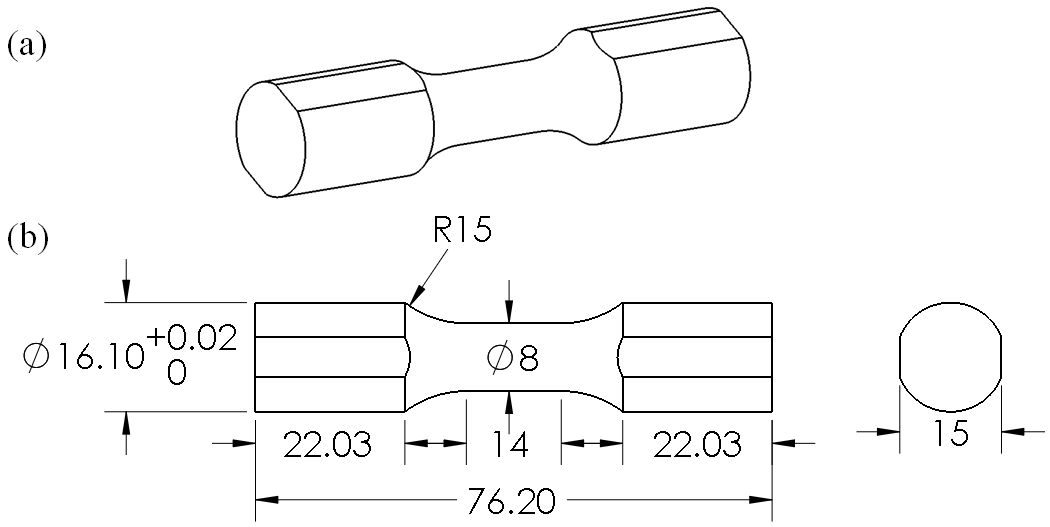

Fig. 3.2: Schematics of specimen for monotonic tension and cyclic loading experiments with dimensions: (a) Schematic illustration and (b) engineering drawing with dimensions.

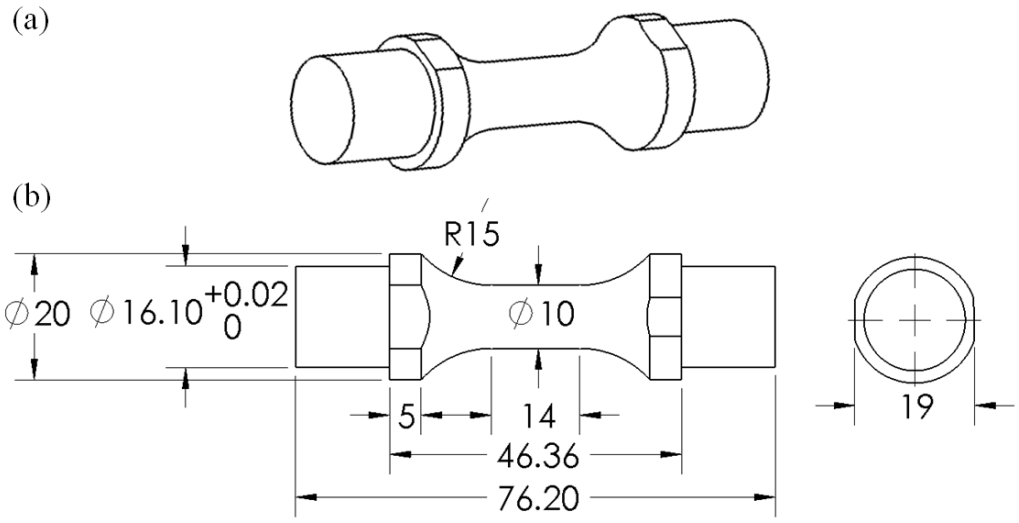

Fig. 3.3: Schematics of specimen for monotonic compression experiments with dimensions: (a) Schematic illustration and (b) engineering drawing with dimensions.

3.2 Mechanical Experiments

In the current study, monotonic tension and monotonic compression experiments are conducted to obtain the static mechanical properties of the material. Fully reversed strain-controlled tension-compression ($R_\varepsilon = -1$) fatigue experiments are conducted to study the cyclic deformation and fatigue property of the material. All the monotonic and cyclic loading experiments were conducted using servo-hydraulic fatigue material testing machines in ambient. The strain was measured by a clip-on extensometer attached to the gage section of the specimen.

The monotonic tension and monotonic compression experiments were conducted with displacement control at an approximate strain rate of $8 \times 10^{-4} s^{-1}$. Both monotonic tension and compression experiments were operated until the specimen was fractured into two parts.

Fully reversed strain-controlled tension-compression fatigue experiments were conducted employing a sinusoidal waveform with strain amplitudes ranging from 0.12% to 6.00%. Loading frequencies ranged from 0.03 Hz to 15 Hz depending on the loading amplitude. The load and engineering strain outputs were recorded automatically by the computer data acquisition system. For each loading cycle, a minimum of 200 data points are recorded. The reported fatigue life was corresponding to the moment when the stress amplitude in a loading cycle dropped by 5% from its peak value.

3.3 Microstructure Characterization

The microstructure characterization is implemented by utilizing SEM and EBSD. After a specimen was failed after experiments, the macroscopic profile of the fracture surface was imaged using a digital microscope. To discern the crack initiation and early-stage growth mechanisms, microstructure in the vicinity of the microcracks was characterized in the region near the macroscopic fracture surface using a field emission SEM and EBSD scanning. The observation plane for SEM and EBSD characterization is illustrated in Fig. 3.4. For the monotonic tension and compression experiments, the samples were cut along the diametral direction near the fracture surface with the scan plane parallel to the YZ plane, which is perpendicular to the TD (refer to Fig. 3.4a). The observation window is located on the YZ plane within a distance of ~0.5 mm to the fracture surface (Fig. 3.4a). As for the fatigue experiments, the samples were also cut along the diametral direction near the fracture surface but following along the fatigue crack propagation direction (Fig. 3.4b). The observation window is located on the diametral plane, with a distance of ~0.5 mm to the initiation site (Fig. 3.4b).

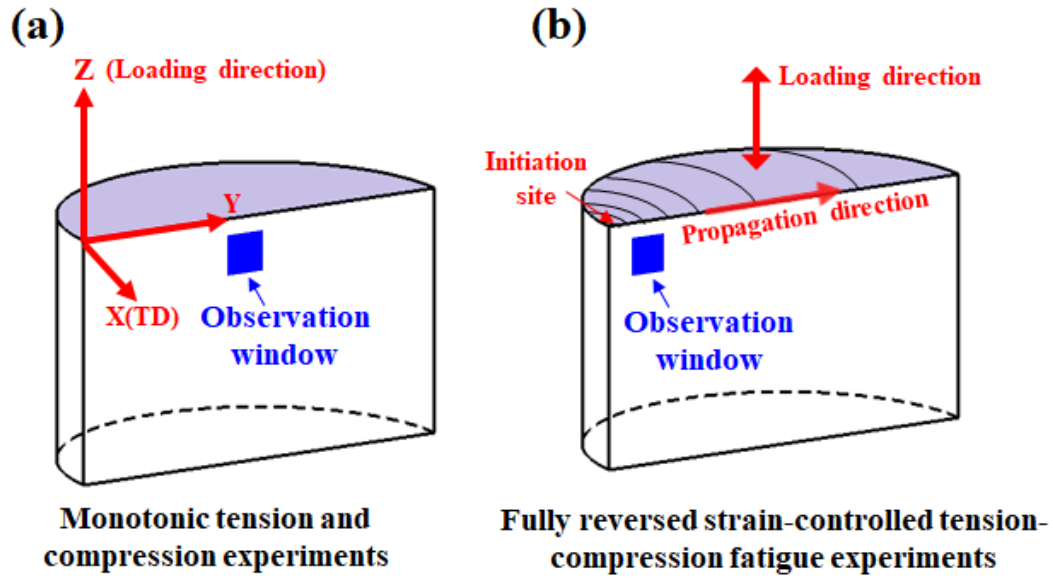

Fig. 3.4: Schematics of the observation plane for SEM and EBSD characterization: (a) Monotonic tension and compression experiments and (b) fully reversed strain-controlled tension-compression fatigue experiments.

The samples were mechanically ground using silicon carbide papers with grit No. from P500 to P1500, followed by polishing using diamond suspension with particle sizes of 6 μm and 1 μm. After a final polishing using alumina with a particle size of 0.05 um, the sample surface was etched with 3% Nital for 8s. The EBSD scans were taken by Joel 7100 F SEM equipped with an Oxford HKL Channel 5 EBSD detector at an acceleration voltage of 25 kV. The working distance was 24 mm. The step size for large scans of 250×250 μm^2 was 0.5 μm. A smaller step size of 0.25 μm was used for high resolution scans specifically to capture the microstructure feature surrounding microcracks.

4 Anisotropic Fracture Behavior of Rolled AZ31B Mg Alloy

4.1 Static Properties

The stress-strain curves under monotonic tension and monotonic compression of the five different orientation specimens are shown in Fig. 4.1 and the static material properties are summarized in Table 3. Engineering stress and engineering strain are used in Fig. 4.1. The true fracture stresses reported in Table 3 are true stresses considering the change of cross section of the testing specimen at fracture. The stress-plastic strain curves shown in Fig. 4.1c with small deformation are used to discuss micro-yielding of the material. To facilitate a comparison, absolute values of the stresses and the strains are used in the stress-strain curves under monotonic compression in Fig. 4.1.

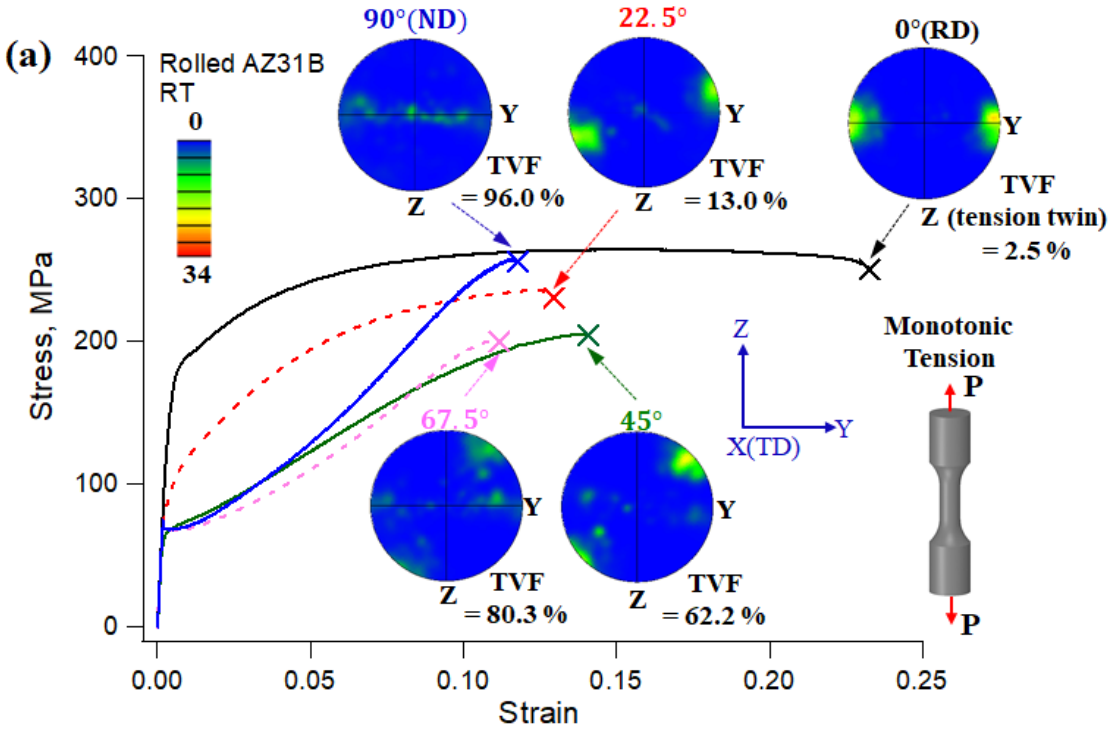
(a)
Rolled AZ31B
RT
0
34
90°(ND)
22.5°
0°(RD)
Y
Z
TVF
= 96.0 %
= 13.0 %
Z (tension twin)
= 2.5 %
67.5°
45°
= 80.3 %
= 62.2 %
Z
Y
X(TD)
Monotonic
Tension
P
Stress, MPa
Strain
0
100
200
300
400
0.00
0.05
0.10
0.15
0.20
0.25

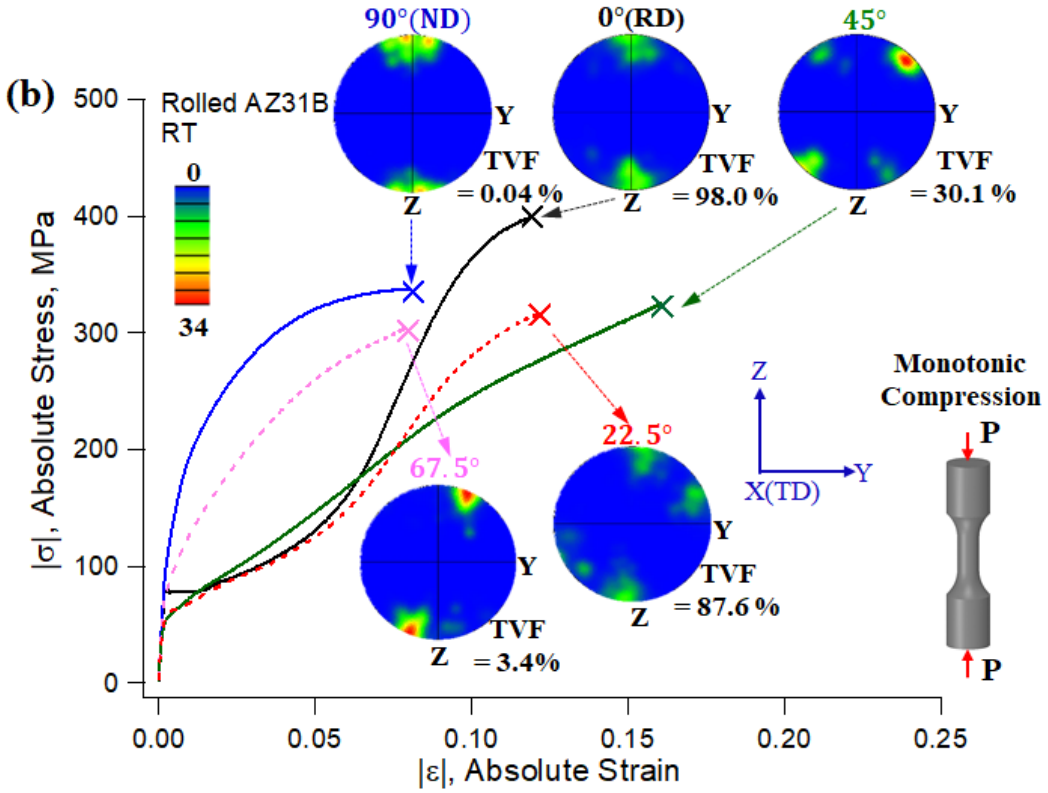
(b)
Rolled AZ31B
RT
0
34
90°(ND)
0°(RD)
45°
Y
Z
TVF
= 0.04 %
= 98.0 %
= 30.1 %
22.5°
67.5°
= 87.6 %
= 3.4%
Z
Y
X(TD)
Monotonic
Compression
P
|σ|, Absolute Stress, MPa
|ε|, Absolute Strain
0
100
200
300
400
500
0.00
0.05
0.10
0.15
0.20
0.25

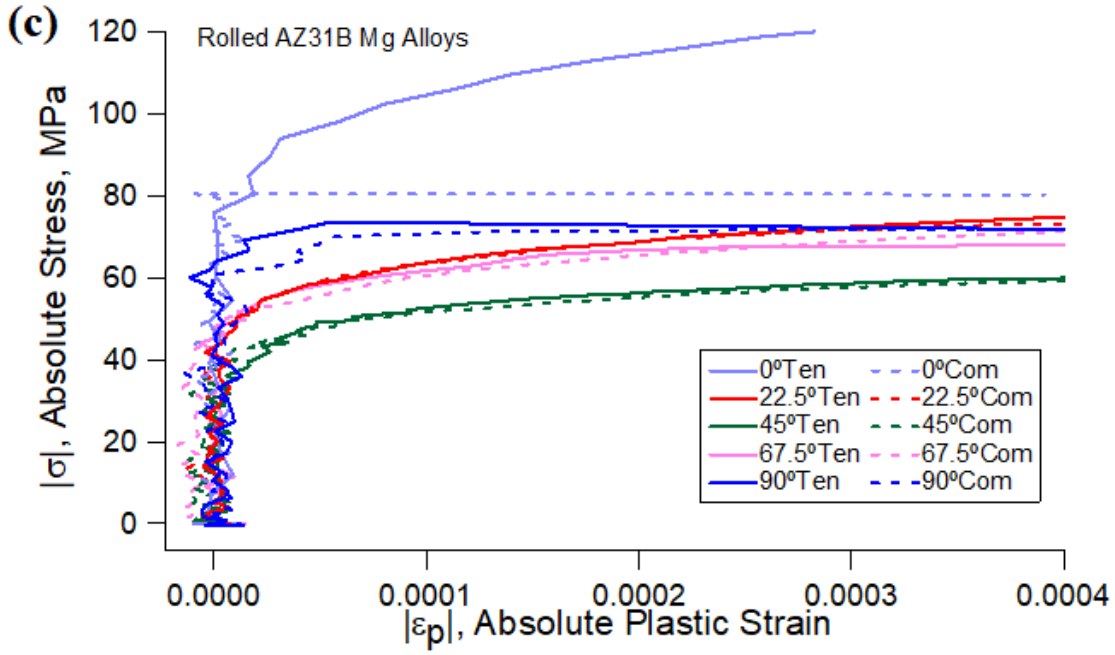

Fig. 4.1: Stress-strain curves of rolled AZ31B Mg alloy under monotonic tension and monotonic compression for five material orientations: (a) engineering stress-engineering strain curves under monotonic tension, (b) engineering stress-engineering strain curves under monotonic compression and (c) stress-plastic strain curves.

Table 3 Static material properties of AZ31B Mg alloy.

Material Orientation	**0º(RD)**	**22.5º**	**45º**	**67.5º**	**90º(ND)**
Elasticity modulus, *E* (GPa)	44.3	44.2	44.3	46.4	47.5
Elastic limit under tension, σ_{et}(MPa)	79.1	39.1	31.8	41.9	57.6
Elastic limit under compression, σ_{ec} (MPa)	79.9	40.2	31.9	41.6	57.0
0.2% offset yield stress in tension, σ_{yt} (MPa)	162.5	92.3	67.3	65.8	67.9
0.2% offset yield stress in compression, σ_{yc} (MPa)	78.0	74.3	69.6	87.1	141.5
Ultimate strength under tension, S_{ut} (MPa)	264.3	235.8	200.6	195.7	257.1
Ultimate strength under compression, S_{uc} (MPa)	415.2	315.4	325.0	307.6	337.1
True fracture stress under tension, σ_{ft} (MPa)	318.9	265.6	234.1	223.1	282.9
True fracture stress under compression, σ_{fc} (MPa)	350.2	278.8	275.5	282.9	311.9
Elongation under tension, e_{ft}	0.233	0.132	0.141	0.113	0.100
Elongation under compression, e_{fc}	0.130	0.122	0.160	0.087	0.085
Reduction in area under tension, *RA* (%)	15.1	12.2	12.7	8.6	9.6

The elasticity moduli are similar in the 0º, 22.5º, and 45º directions, and the values are slightly higher in the other two material orientations. Knowing that the rolled Mg plate has most *c*-axis of the grains parallel to the ND, the elasticity modulus results are consistent with the theoretical values of a single crystal Mg where the elasticity modulus along the *c*-axis is higher than that along a direction perpendicular to the *c*-axis[128,129].

Basal slips are often activated earlier than twinning due to the low critical resolved shear stress. As a result, the symmetrical nature of slips leads to the identical elastic limit under tension and under compression for a given material orientation (Fig. 4.1b). Approximating the rolled plate as a single crystal with its c-axis along the ND, the Schmid factor for basal slips is the largest for the 45º material orientation and, consequently, the elastic limit is the lowest in the 45º orientation. Basal slips in the RD and ND specimens are due to the mis-orientation of some grains of the polycrystalline Mg alloy from the perfect *c*-axis alignment along the ND.

Material strength as measured by the ultimate strength and the true fracture stress exhibits a consistent trend. The ultimate strength and the true fracture stress of the material at a given orientation is larger in compression than these under tension. With respect to the material orientation effect, the true fracture stress, which is based on true stress, is the highest in the RD (0º) followed by ND (90º), 22.5º, 45º, and 67.5º. The order is slightly different in terms of the ultimate strength which is based on the nominal or engineering stress.

The 0.2% offset yield stress is a strong function of material orientation and the dominating plastic deformation mechanism. When θ is less than 45º, the 0.2% offset yield stress is determined by basal slips when subjected to tension loading and it is dictated by

twinning under compression. The opposite holds true for θ larger than 45º. Consequently, the 0.2% offset yield stress under tension continuously decreases asymptotically with increasing θ with little influence of material orientation effect after $\theta > 45º$. The yield stress under compression has an opposite tendency with respect to the material orientation: the value of the yield stress under compression is similar when $\theta < 45º$, and it increases significantly when θ increases from 45º to 90º.

No necking was observed in any of the monotonic tension experiments. Ductility measures in terms of either the elongation or the reduction in area (RA) provide a similar conclusion with regard to the influence of material orientation on ductility. Overall, the RD has the highest ductility and the ND and 67.5º have the lowest. The 22.5º and 45º orientations have similar ductility that falls between these of the RD and ND. Tension-compression asymmetry is observed for the elongations. Except for the 45º orientation, the elongation under tension is higher than that under compression. The current results are consistent in general tendency with those obtained in earlier studies [54][59].

4.2 Deformation Features

Pronounced tension-compression asymmetry due to the strong texture can be observed in Figs. 4.1a-b. The shape of the stress-strain curve under monotonic loading is associated with the deformation mechanisms. The twin volume fraction (TVF) was calculated as the ratio of the $\{10\bar{1}2\}$ tension twin area to the total scanned area and embedded in Figs. 4.1a-b. The information regarding the micro-yielding of the material can be obtained in Fig. 4.1c.

The elastic limits shown in Fig. 4.1c indicate that the activation of basal slips in favorably orientated grains results in the microyielding plastic deformation. It is well

accepted that among all the deformation modes for a Mg alloy at room temperature, the basal slip is the easiest to be activated due to the very low CRSS[130,131]. As a result, basal slips are activated first in early plastic deformation. Due to the fact that the grains favorably oriented for basal slips are a minority population, the activation of basal slip in these grains only induces micro yielding and the overall macroscopic response shows little evidence of yielding[132][133][134].

As the stress exceeds the elastic limit, the linear elastic deformation stage terminates and the material yields. As shown in Fig. 4.1a and Fig. 4.1b, the tensile stress-strain curves for $\theta < 45^{o}$ and the compressive stress-strain curves for $\theta > 45^{o}$ exhibit an overall concave-down shape. The plastic deformation is accommodated mostly by dislocation slips with limited tension twinning. As evidenced in the deformation pole figures and TVFs, the change of texture due to twinning is trivial: TVF = 2.5% for tension at $\theta = 0^{o}$, TVF=13% for tension at θ =22.5%, TVF = 3.4% for compression at $\theta = 67.5^{o}$, and TVF = 0.04% for compression at $\theta = 90^{o}$. In contrast, typical sigmoidal shaped stress-strain curves can be identified for tension at $\theta > 45^{o}$ and compression at $\theta < 45^{o}$, where tension twinning plays a dominating role in plastic deformation. The TVFs of tension twins at fracture can attain as high as 80.3% and 96%, respectively, for tension at $\theta = 67.5^{o}$ and 90^{o} (ND), and as high as 98.0% and 87.6%, respectively, for compression at $\theta = 0^{o}$(RD) and 22.5^{o}. The transformation in the stress-strain curve from a concave-up shape in the initial stage to a later concave-down shape signifies the exhaustion of tension twinning as well as the involvement of non-basal dislocation slips [134,135]. Prismatic slips contribute significantly to the plastic deformation for the $\theta = 67.5^{o}$ and 90^{o} (ND) under tension at the later deformation stage [136].

For the θ = 45º material orientation, the tensile stress-strain curve displays a concave-up shape (up to ~10%) followed by a concave-down shape. Due to the high Schmid factors (SFs) and the low CRSS values, basal slips act as the major deformation mechanism during the whole plastic deformation in this material orientation [136]. As the strain increases, tension twins gradually form, while the pyramidal <c+a> slips, as well as the basal slips are activated in twinned grains to accommodate the plastic deformation [136]. The TVF of tension twins at fracture is 62%. The compressive stress-strain curve exhibits an overall concave-down shape. This observation indicates that fewer tension twins were activated during compressive loading comparing with that under tension, as evidence by the TVF of tension twins at fracture is only 30.1% under compression. The overall tendency of the stress-strain curves for θ = 0º, 45º and 90º is consistent with the observation in previous work [68].

4.3 Macroscopic Fracture Surface

Figure 4.2 shows the macroscopic profiles of the fracture surfaces. The fracture surfaces exhibit two macroscopic features: (1) irregular-shaped brittle-like fracture and (2) flat-surfaced shear fracture. The macroscopic fracture surfaces under tension at θ = 0º, 67.5º, and 90º show irregular-shaped brittle-like features composed of ridges and islands. For the tension at θ = 45º and 22.5º, and compression at all the five material orientations, a flat shear surface is observed with different angles between the loading axis (Z-axis) and projected trace of the fracture surface on the YZ plane (Fig. 4.2). These angles are also indicated in Fig. 4.2.

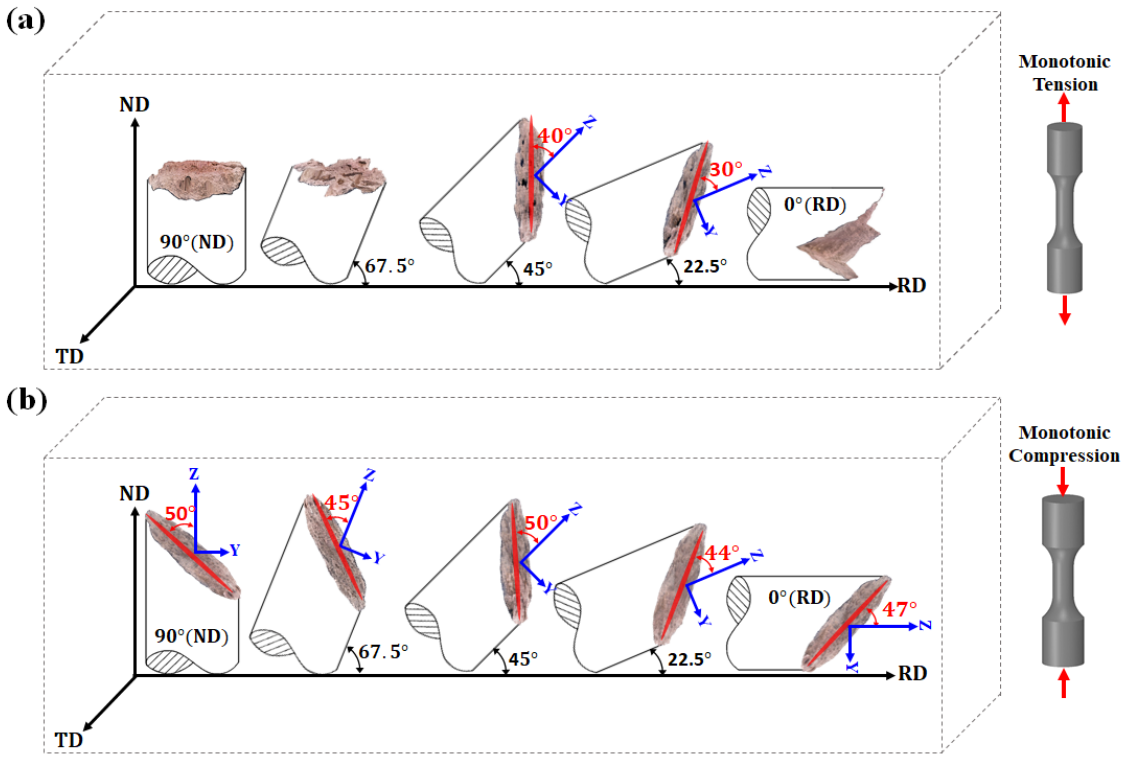

Fig. 4.2: Macroscopic fracture surfaces of rolled AZ31B Mg alloy tested under (a) monotonic tension and (b) monotonic compression along different material orientations at θ = 0º, 22.5º, 45º, 67.5º and 90º with respect to the rolled direction.

4.4 Fracture Mechanisms

To identify the fracture mechanisms, we examined the microcracks and microstructural features in the region near the fracture surface on the YZ plane cut along the diametral direction in the cylindrical testing specimen. Specifically, short microcracks with lengths in tens of microns are used to infer the crack initiation mechanism. Intermediate-sized microcracks spanning across several grains with lengths in hundreds of microns are used to identify early-stage crack growth. For those final fracture surfaces showing flat shear plane (θ = 22.5º and 45º), we further carried out trace analysis for the fracture surface to infer the macro-crack propagation mode.

4.4.1 Tension at θ = 0º (RD)

As seen from Fig. 4.2, tension at $\theta = 0^{o}$ (RD), 67.5º and 90º (ND) exhibits brittle fracture surfaces showing irregular-shaped ridge and island features. The microcracks in the local area near (within a distance of ~0.5 mm) the fracture surface are characterized to investigate the early-stage crack growth mode as well as the crack initiation mechanism.

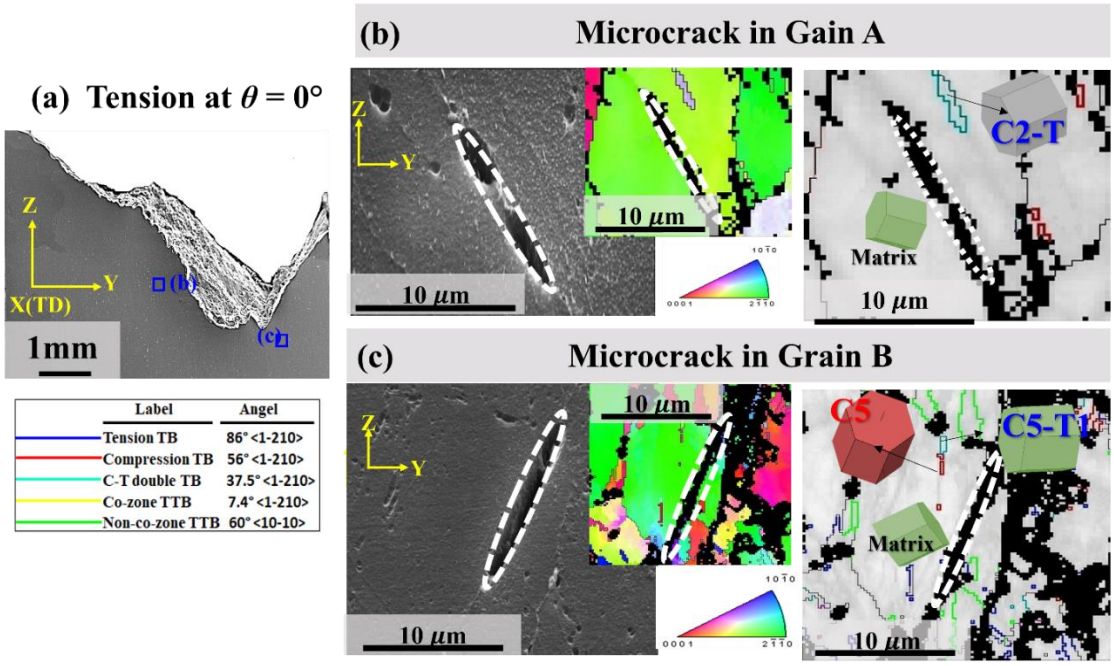

Fig. 4.3: Microcracks observed for the 0° (RD) specimen under tension: (a) SEM image captured in the area near the fracture surface on the YZ plane, which is sectioned by cutting the cylindrical specimen through its diameter, (b,c) SEM image along with EBSD results (IPF and IQ maps) showing the microstructural features surrounding the microcracks. In the IQ map, grain boundaries are denoted by black lines. Tension, compression, and C-T double twin boundaries are colored in blue, red, and light blue respectively. Co-zone and none co-zone twin-twin boundaries are delineated in yellow and green colors.

Figure 4.3 shows the SEM and EBSD characterization area near the fracture surface on the YZ plane. Figs. 4.3b and 4.3c present two microcracks located beneath the fracture surface, both of which are sized approximately 12 μm in length. These microcracks appear

to be of lenticular shape and have sharp crack tips. This microcrack morphology is likely to result from TB cracking [68][137]. EBSD characterization of the microstructure surrounding the microcrack reveals clear development of compression twins and C-T double twins. In Grain A (Fig. 4.3b), a double twin trace shows the same alignment with the microcrack. This indicates the microcrack in Grain A is likely a result of TB cracking by the same C-T double twin variant. Similarly, a compression twin (C5) along with a connected double twin C5-T1 are found in the vicinity of a microcrack in Grain B (Fig. 4.3c). Although there is no direct connection between the occurrence of a microcrack and compression/double twins, the large local shear by compression and C-T double twinning may result in incompatible deformation and may potentially lead to initiation of microcracks. In fact, the results evidenced in our work under tension at θ = 0º (RD) are consistent with those regularly reported in prior studies, confirming that the detrimental role of compression/double twinning on crack initiation [76,77,80–82].

4.4.2 Tension at θ = 22.5º

Different from the cases of tension at θ = 0º (RD), 67.5º and 90º (ND), the fracture surface under tension at θ = 22.5º and 45º show flat shear planes. For tension at θ = 22.5º, the trace of fracture surface projected on the YZ plane forms an angle, α, of 30º with respective to the Z-axis.

To discern a slip/twinning system responsible for the shear cracking, we characterized the grain orientations in a relatively large area near the fracture surface on the YZ plane, which is exposed by cutting the cylindrical specimen along its diameter (Fig. 4.4a). We first carried out SF analysis to determine what slip/twinning systems are most likely operative. In the case of tension at θ = 22.5º, basal slip is the dominant deformation

mechanism due to its extremely low CRSS and their high SF values, most of which is higher than 0.4 (Fig. 4.4b). We further plot all the traces corresponding to the basal plane by projecting the basal plane at every crystal orientation onto the YZ plane. By comparing the histogram of the orientation (β) of the basal-plane traces with the orientation (α) of the fracture-surface trace (Fig. 4.4b), we find that the basal-slip plane traces match well with that of the fracture surface, which indicates shear cracking is accommodated by basal slips. In fact, we have ruled out other less active slip/twinning systems, including prismatic slip, pyramidal <*a*+*c*> slip, tension twinning and compression twining. None of them shows a good agreement of the slip/twin plane traces with the fracture surface trace.

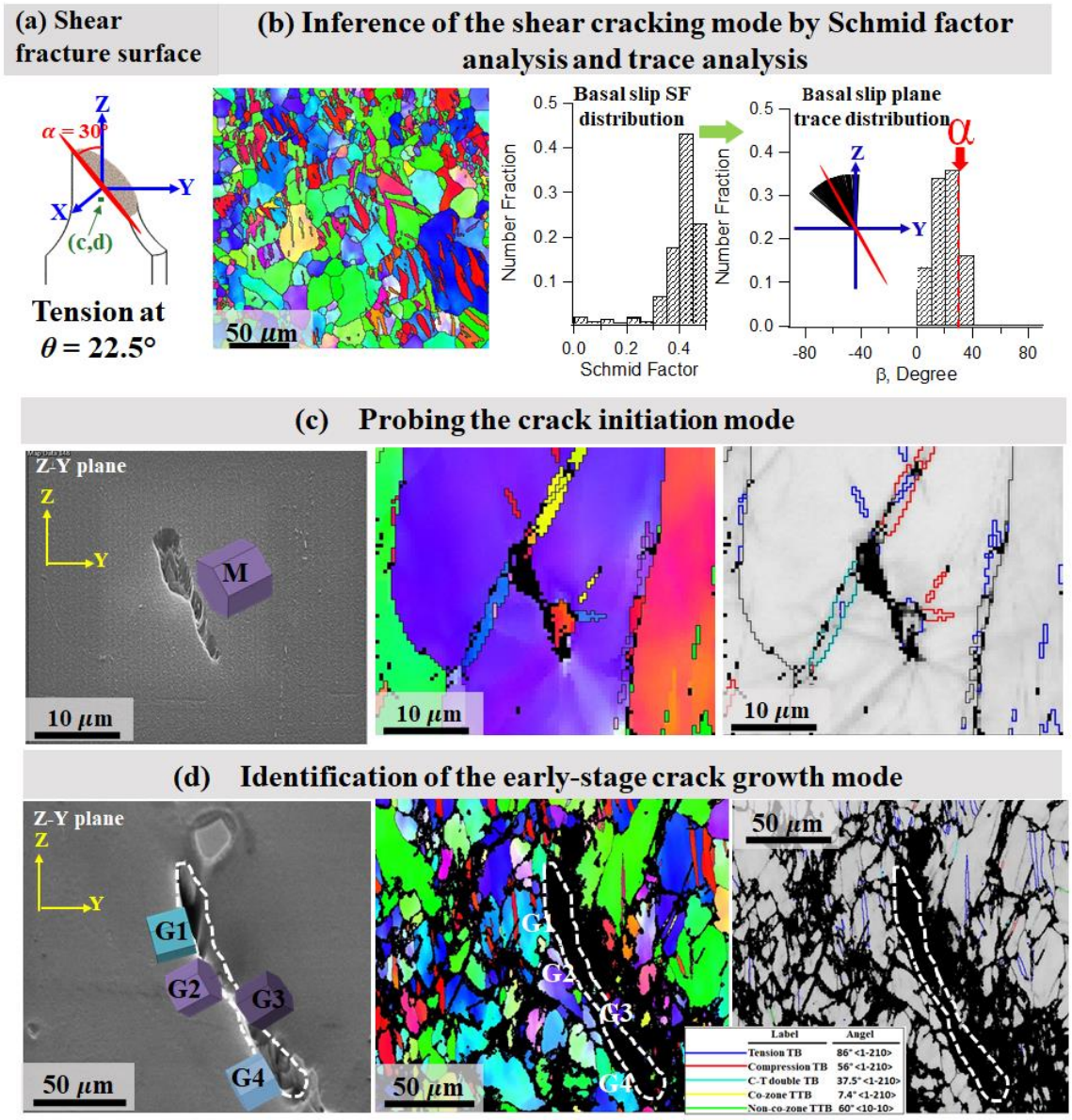

Fig. 4.4: Fracture mechanisms under tension at $\theta = 22.5^{\circ}$. (a) Trace of shear fracture surface forming orientation angles of $\alpha = 30^{\circ}$ to the Z-axis on the YZ plane, (b) inference of the shear cracking mode by Schmid factor analysis and trace analysis of the shear fracture surface, (c) Probing the crack initiation mode by characterizing the short microcrack and (d) identification of the early-stage crack growth mode by characterizing intermediate-sized microcrack. The left, middle, and right images in (c,d) are SEM micrograph, inverse pole figure (IPF) map and image quality (IQ) map, respectively. In the IQ map, grain boundaries are denoted by black lines. Tension, compression, and double C-T twin

boundaries are colored in blue, red, and light blue respectively. Co-zone and none co-zone twin-twin boundaries are delineated in yellow and green colors.

To clarify the crack initiation mode, we characterized the microstructure in the vicinity of short microcracks sized in tens of micros. Fig. 4.4c shows a short microcrack sized approximately within one grain, compression twins and C-T double twins are clearly developed in connection to the microcrack. However, it is interesting to find that the habit plane of the microcrack is persistently the basal plane. We conclude that the microcrack observed on the basal slip band in Fig. 4.4c is likely nucleated from the local damage induced by the impingement of compression and/or double twinning.

To further elucidate the crack propagation mode, in particular during the ealy-growth stage, we characterized the microstructure in the vicinity of intermediate-sized microcrack which spans across several grains, as shown in Fig. 4.4d. The crack propagation path persistently aligns well with the basal slip traces, confirming that the crack extension is dominated by cracking along basal slip bands. GB cracking can be found in the propagation route of the microcrack.

4.4.3 Tension at θ = 45º

The fracture surface under tension at θ = 45º shows similar flat shear plane to that of θ = 22.5º (Fig. 4.5a). However, the trace of the fracture surface forms an angle of 40º to the Z-axis on the YZ plane. It is noticeable that the bulk shear stress resolved on the fracture surface is close to the maximum shear stress in the uniaxial tensile stress state. Therefore, it is hypothesized that the final fracture at θ = 45º is proceeded by shear cracking accommodated by localized shear deformation operated *via* certain dislocation slip/twinning modes. We can apply the same procedures using Schmid analysis and trace

analysis to infer the cracking mechanism. As shown in Fig. 4.5b, the trace of the fracture surface matches well with the basal-slip plane, implying that cracking is mainly driven by the shear deformation localized in basal slip bands.

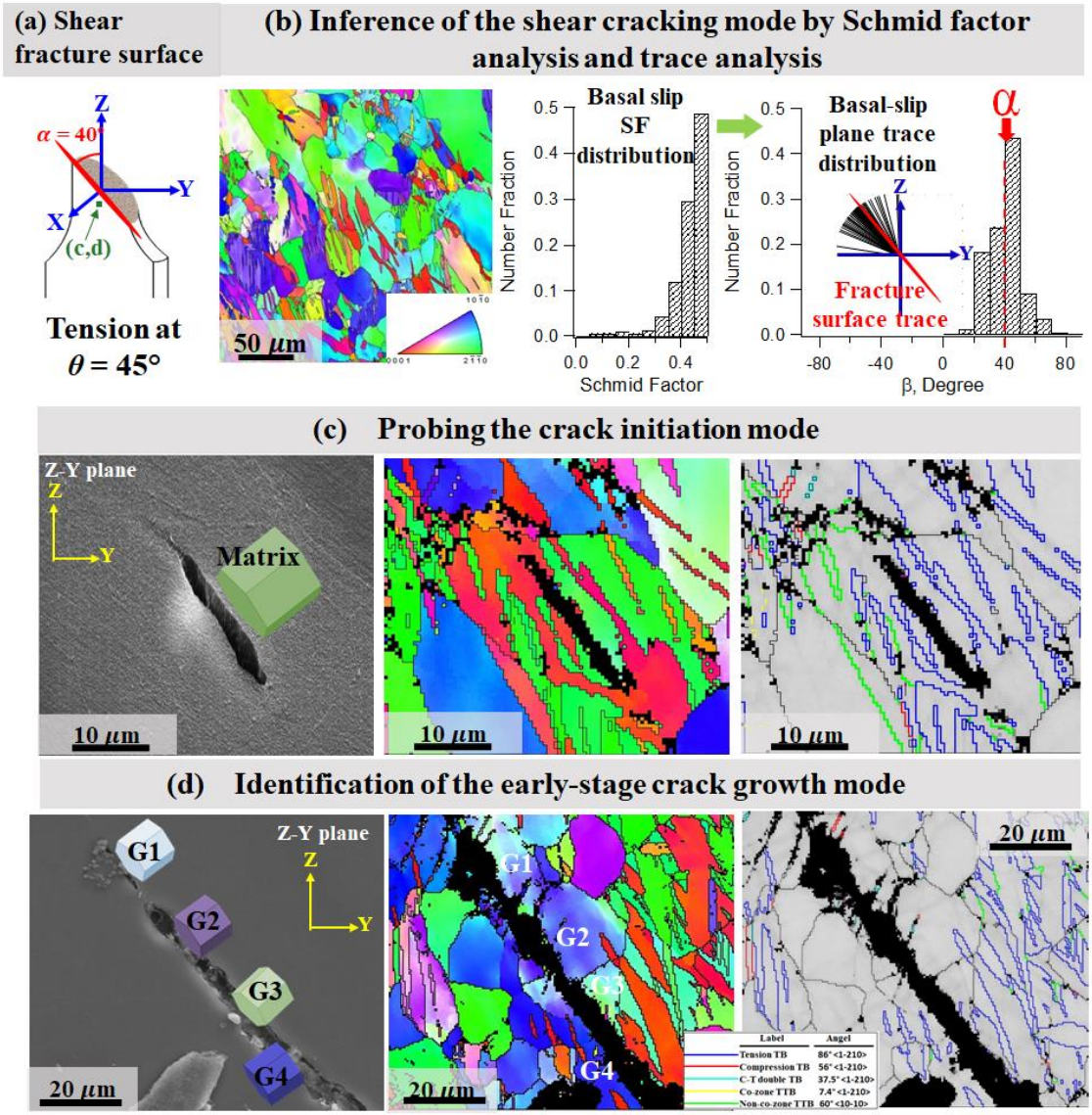

Fig. 4.5: Fracture mechanisms under tension at $\theta = 45^{o}$: (a) Trace of shear fracture surface forming orientation angles of $\alpha = 40^{o}$ to the Z-axis on the YZ plane, (b) inference of shear cracking mode by Schmid factor analysis and trace analysis of the shear fracture surface, (c) probing of the crack initiation mode by characterizing the microcrack and (d) identification of the early-stage crack growth mode by characterizing intermediate-sized

microcrack. The left, middle, and right images in (c,d) are SEM micrograph, inverse pole figure (IPF) map and image quality (IQ) map, respectively. In the IQ map, grain boundaries are denoted by black lines. Tension, compression, and T-C double twin boundaries are colored in blue, red, and light blue respectively. Co-zone and none co-zone twin-twin boundaries are delineated in yellow and green colors.

We further examined the small microcrack sized approximately 20 μm observed in a single grain (Fig. 4.5c). As viewed in the IPF and IQ maps, pronounced tension twins are developed in the grain. However, it is interesting to find that the microcrack persistently resides on the basal-slip plane of the matrix area in the grain. Our observation in Fig. 4.5c indicates that crack initiation under tension at θ = 45º might originate from the local damages induced by impingement of tension twins on the basal slip bands. Unlike the case of tension at θ = 22.5º (Fig. 4.4c), where the microcrack observed on the basal slip band is likely nucleated from the local damage induced by the impingement of compression and/or double twinning. The observation in Fig. 4.4c is reasonable as tension at θ = 22.5º leads to a higher favorability of compression twin and C-T double twinning than tension at θ = 45º.

In Fig. 4.5d, we further examined the microcrack size in lengths spanning from several grains. It is revealed that the microcrack (inclined ~40º to the Z-axis) propagates in transgranular mode through grain G1 and grain G2. Similar to the case of tension at θ = 22.5º (Fig. 4.4c), the propagation route is followed by intergranular cracking on grain boundary (GB) formed between grain G3 and grain G4. This result indicates that the early-stage crack growth is actually proceeded by alternative routes via transgranular cracking along the basal-slip planes and intergranular cracking at GBs.

4.4.4 Tension at θ = 67.5º

As shown in Fig. 4.2, the fracture surfaces obtained from tension at θ = 67.5º and 90º (ND) share similar brittle-like features as that under tension at θ = 0º. This macroscopic fracture feature is consistent with the observation from a previous study on the same material that a serrated brittle-like fracture surface is exhibited under tension along the ND [68]. However, as discussed in Section 4.2, pronounced tension twins are developed after tensile fracture. The TVFs after fracture attain as high as 80.3% and 96% for θ = 67.5º and 90º (ND), respectively. It would be interesting to see whether the fracture mechanisms, in particular the crack initiation mode, are still ascribed to double-twinning induced damage.

Figure 4.6 shows the microcrack characterized in the local area near the fracture surface for tension at θ = 67.5º. Unlike the predominant lenticular-shaped microcracks due to TB cracking under tension at θ = 0º, the microcracks developed in tension at θ = 67.5º are much shorter in length spanning only ~5-15 μm (see the SEM images in Fig. 4.6b) and show relatively blunted crack tips. As shown in Fig. 4.6b, the microcrack is developed mainly at the GB between grain G1 and grain G2 where a triple joint met by grains G1, G2 and G3. The misorientation angles between the neighboring grains are 70º, 68º, and 59º for G1-G2 pair, G2 and G3 pair, G3-G1 pair, respectively. This indicates that the GB cracking is favorable to be initiated from the high angle grain boundaries (HAGBs). Interestingly, significant non co-zone twin-twin boundaries (TTBs) are developed in G1 and G2 and frequently connected to the microcrack, which are considered as the major driving for GB cracking.

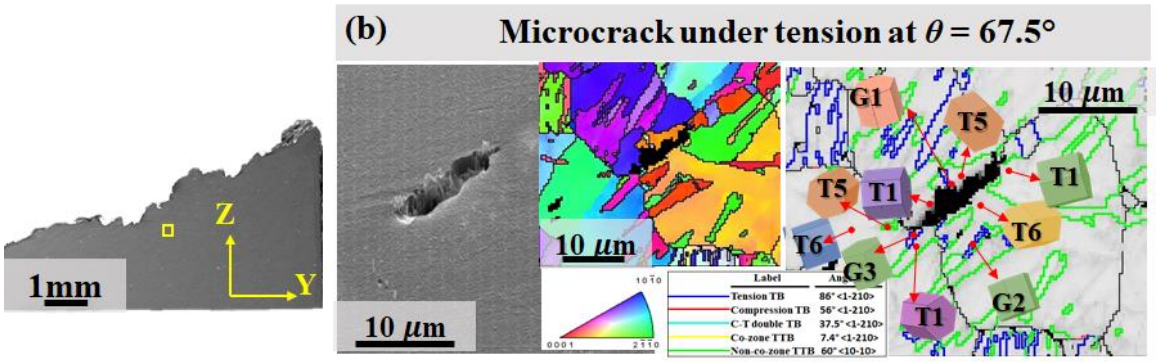

Fig. 4.6: Microcrack observed on the specimens subjected to tension at θ = 67.5º: (a) SEM image captured in the area near the fracture surface on the YZ plane which is sectioned by cutting the cylindrical specimen through the diameter, (b) SEM image and EBSD results (IPF and IQ maps) showing the microstructural features surrounding the microcrack. In the IQ map, grain boundaries are denoted by black lines. Tension, compression, and C-T double twin boundaries are colored in blue, red, and light blue respectively. Co-zone and none co-zone twin-twin boundaries are delineated in yellow and green colors.

4.4.5 Tension at θ = 90º (ND)

Figure 4.7 shows the microcrack characterized in the local area near the fracture surface for tension at θ = 90º (ND). Similar to the microcracks developed in tension at θ = 67.5º, the microcrack indicated in Fig. 4.7 with a short length of 8 μm exhibits blunted crack tips. Further EBSD characterization reveals that the short microcracks are located at triple joints and grain boundaries. For instance in Fig. 4.7b, the microcrack is resulted from GB cracking at high angle grain boundaries between grain G2 and G3, where a triple joint met by grains G1, G2 and G3. Significant none co-zone twin-twin boundaries (TTBs) are developed in G2 and G3 due to the coalescence of fully-expanded tension twins. Moreover, a tension-compression-tension (T-C-T) tertiary twin is observed in G3 with its tip connected to the microcrack. These observations shed lights that the GB impingement of dislocations from the formation of both none co-zone TTBs and T-C-T tertiary twins can

lead to local stress concentration, causing twinning-induced GB damage and triggering GB cracking subsequently.

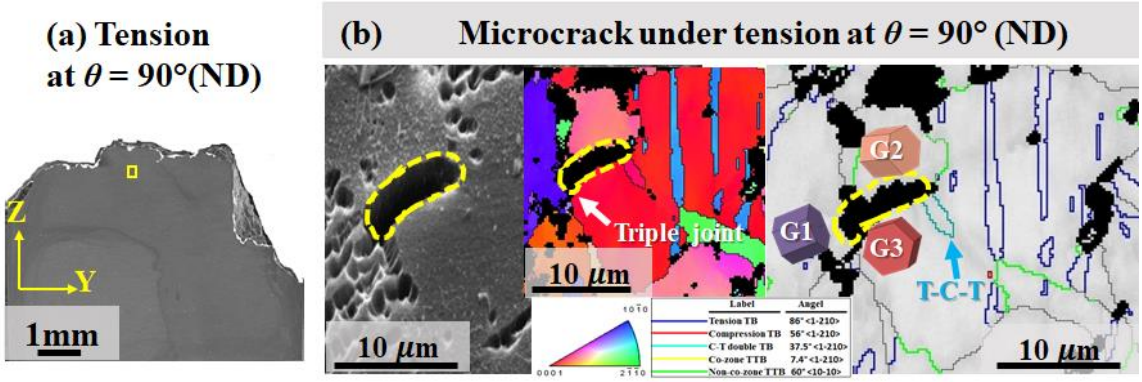

Fig. 4.7: Microcracks observed on the specimens subjected to tension at θ = 90º (ND): (a) SEM image captured in the area near the fracture surface on the YZ plane which is sectioned by cutting the cylindrical specimen through the diameter, (b) SEM image and EBSD results (IPF and IQ maps) showing the microstructural features surrounding the microcrack. In the IQ map, grain boundaries are denoted by black lines. Tension, compression, and C-T double twin boundaries are colored in blue, red, and light blue respectively. Co-zone and none co-zone twin-twin boundaries are delineated in yellow and green colors.

4.5 Further discussion

C-T double twins are commonly considered as a detrimental factor that causes the microcrack nucleation that leads to final failure [76,77,80–82]. Such an understanding reflects one facet of the anisotropic nature of fracture in wrought Mg materials. In fact, double twinning, as a critical fracture mechanism, is typically observed in experiments where tensile loading is unfavorable for extensive tension twinning. The contribution of the current work is to uncover a more comprehensive picture of the tensile fracture behavior in wrought Mg alloy. The major findings are summarized in Fig. 4.8. The final fracture modes are closely related to the deformation modes operated under a specific stress state.

Basically, two fracture modes are categorized: (1) brittle-like cracking which leads to irregular-shaped fracture surface under tension at θ = 0º, 67.5, and 90º; and (2) shear cracking which results in flat macroscopic shear fracture surface under tension at θ = 22.5º and 45º.

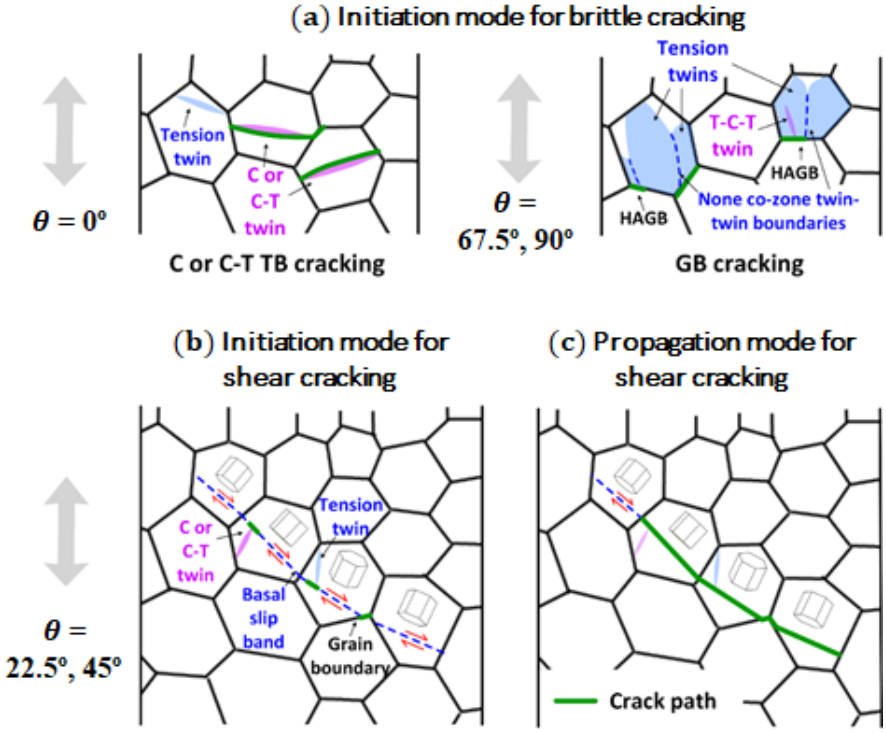

Fig. 4.8: Schematics summarizing the anisotropic fracture mechanisms in rolled Mg alloy. (a) Initiation mode for brittle-like cracking in tension at θ = 0º, 67.5, and 90º. (b) Initiation mode for shear cracking in tension at θ = 22.5º and 45º. (c) Crack propagation mode for shear cracking in tension at θ = 22.5º and 45º. "C or C-T TB" represents "compression or compression-tension twin boundary". "HAGB" denotes "high-angle grain boundary".

The macroscopic fracture surfaces under tension at θ = 0º, 67.5, and 90º show brittle-like features with irregular-shaped ridges and islands. Since there is no preferential crack propagation path, we only focus on the crack initiation modes by charactering microcracks near the fracture surface to reveal the fracture mechanisms in these material orientations.

As shown in Fig. 4.8a, crack initiation mode displays distinctive microstructural origins between the case of θ = 0º and the cases of θ = 67.5º and 90º. For θ = 0º, where tension twinning is unfavored and compression twinning is promoted, crack initiation is commonly detected as cracking at compression and/or C-T double twin boundaries. However, tension at θ = 67.5º and 90º favors extensive tension twinning, which often results in significant twin-twin interaction and even the development of T-C-T tertiary twins. Rather than TB cracking, cracking at high-angle grain boundaries (HAGBs) acts as the dominant crack initiation mode at θ = 67.5º and 90º . Interestingly, C-T-C tertiary twins and none co-zone TTBs with high-angle misorientation are found to be connected to the crack initiation sites, suggesting that the deformation incompatibility induced by the development of these microstructures may serve as the driving force for crack initiation at θ = 67.5º and 90º . It is worth noting that microcracks nucleated by either TB cracking at θ = 0º or GB cracking at θ = 67.5º and 90º are sparsely distributed at multiple locations in the material. Unlike the cases of tension at θ = 22.5º and 45º, there is no preferential crack propagation route for the nucleated microcracks to grow probably due to the large difference in the orientation of these microcracks. That is also the reason why the final fracture surface shows brittle-like features with irregular-shaped ridges and islands.

As shown in Figs. 4.8b and 4.8c, shear cracking occurring under tension at θ = 22.5º and 45º is mainly resulted from the extensive shear deformation accommodated by basal slips which are the dominant deformation modes in these two loading directions. Cracks are nucleated solely from basal slip bands at local damages induced by impingement of tension, compression, and C-T double twins (Fig. 4.8b). Due to the strong basal texture, basal slips under tension at θ = 22.5º, 45º can be easily transmitted across neighboring

grains, most of which have low misorientation angles. The propagation of the nucleated crack, which is driven by the shear deformation localized in basal-slip bands, follows the transmitted basal-slip bands across the neighboring grains (Fig. 4.8c). As a result, the final crack follows a preferential path on the YZ plane whose orientation matches well with that of the basal-plane traces projected on the same observation plane, as characterized in Figs. 4.6 and 4.7.

4.6 Summary

The material orientation effect on the anisotropic deformation and fracture behavior of a rolled AZ31B Mg alloy was investigated by performing monotonic tension and monotonic compression experiments in five material orientation. θ denotes the angle between the axial direction of the testing specimen and the rolled direction of the material. Major experimental observations and mechanisms are summarized as follows:

1) The elastic limit under tension is identical to that under compression for any given material orientation with the highest to lowest following the order 0º (RD), 90º (ND), 67.5º, 22.5º, and 45º. The ultimate strength and true fracture strength are higher under compression than these under tension for a given material orientation. The true fracture stress and ductility are the highest in the RD (0º). Significant tension-compression asymmetry can be identified in the stress-strain curves due to the strong texture. Microyielding is induced by the activation of basal slips.
2) The material orientation affects the tension fracture behavior. Tension at θ = 0º, 67.5, and 90º results in brittle-like fracture surfaces while tension at θ = 22.5º and 45 ° displays macroscopic shear fracture behavior.

3) The microstructural origins of brittle-like cracking are different between the case of tension at θ = 0º and that of tension at θ = 67.5º and 90º. Twin boundary cracking in compression and/or compression-tension double twins is commonly detected in tension at θ = 0º whereas high-angle grain boundary cracking, which is facilitated by the impingements of tension-compression-tension tertiary twins and the none co-zone twin-twin boundaries, acts as the crack initiation mode in tension at θ = 67.5º and 90º
4) Crack initiation under tension at θ = 22.5º and 45º is originated from shear deformation in the basal slip bands at local damages induced by impingement of tension, compression and/or compression-tension twins. Crack extension is driven by localized shear deformation in basal slip bands which can be transmitted across neighboring grains, resulting in a final crack path following basal plane traces.

5 Characteristic Cyclic Plastic Deformation

5.1 Macroscopic Stress-Strain Response

The strain-life curve of a Mg alloy is characterized with two distinct kink points which are closely associated with the dominating plastic deformation mechanism [111]. On this regard, three representative strain amplitudes, 0.30%, 1.00%, 3.00% which correspond to the strain amplitude below the lower kink point, between the lower kink point and the upper kink point, and above the upper kink point, respectively, were chosen for a detailed analysis. Fig. 5.1 shows the stress-strain hysteresis loops obtained from fully reversed strain-controlled tension-compression strain-controlled fatigue experiments. In order to show the evolution of the hysteresis loops with respect to the loading cycles, the stress-strain hysteresis loops of the first 10 cycles, the cycle at a quarter fatigue life, and the cycle at half fatigue life are presented. The stress-strain hysteresis loops corresponding to half-fatigue lives are taken to be the stabilized hysteresis loops. The stabilized stress-strain hysteresis loops with selective strain amplitudes of the five material orientations are shown in Fig. 5.2. A solid circle on a stress-strain hysteresis loop denotes an inflection point which mathematically is the point where the second derivative of the stress with respect to the strain is zero. The inflection points reflect the transition of two dominating plastic deformation mechanisms: from twinning or detwinning to non-basal slips. It can be observed in Figs. 5.1-5.2 that the shape of the stress-strain hysteresis loops is dependent on the material orientation and the applied strain amplitude.

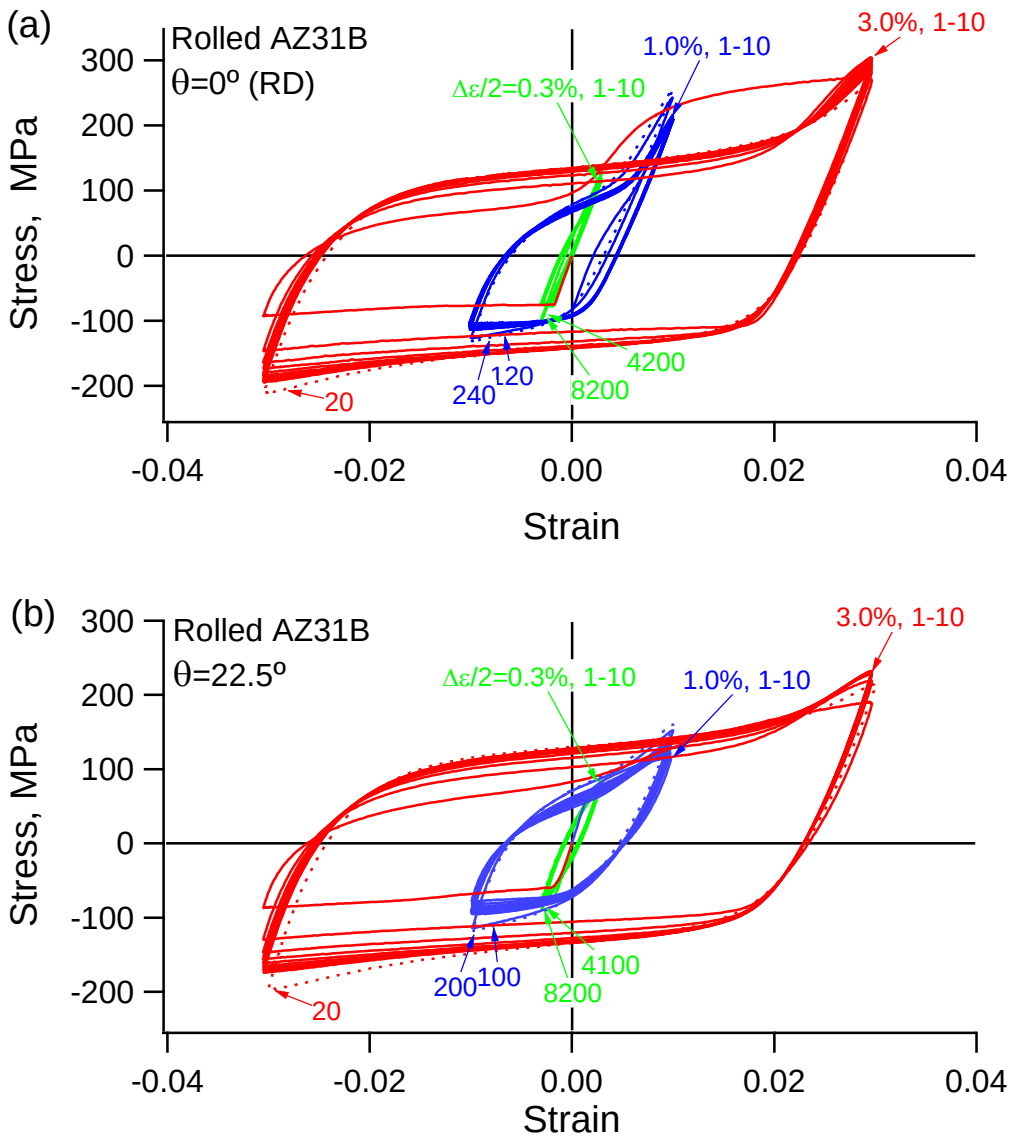
(a)
Rolled AZ31B
θ=0º (RD)
Stress, MPa
Strain
3.0%, 1-10
1.0%, 1-10
Δε/2=0.3%, 1-10
4200
120
240
8200
20
(b)
Rolled AZ31B
θ=22.5º
Stress, MPa
Strain
3.0%, 1-10
Δε/2=0.3%, 1-10
1.0%, 1-10
4100
200
100
8200
20

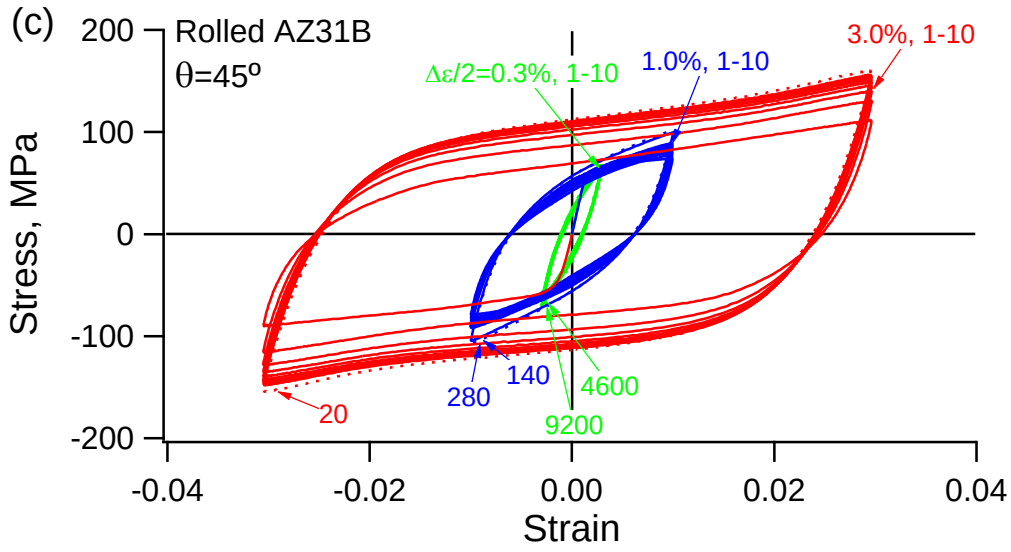
(c)
Rolled AZ31B
θ=45º
Δε/2=0.3%, 1-10
1.0%, 1-10
3.0%, 1-10
20
280
140
4600
9200
Stress, MPa
Strain
200
100
0
-100
-200
-0.04
-0.02
0.00
0.02
0.04

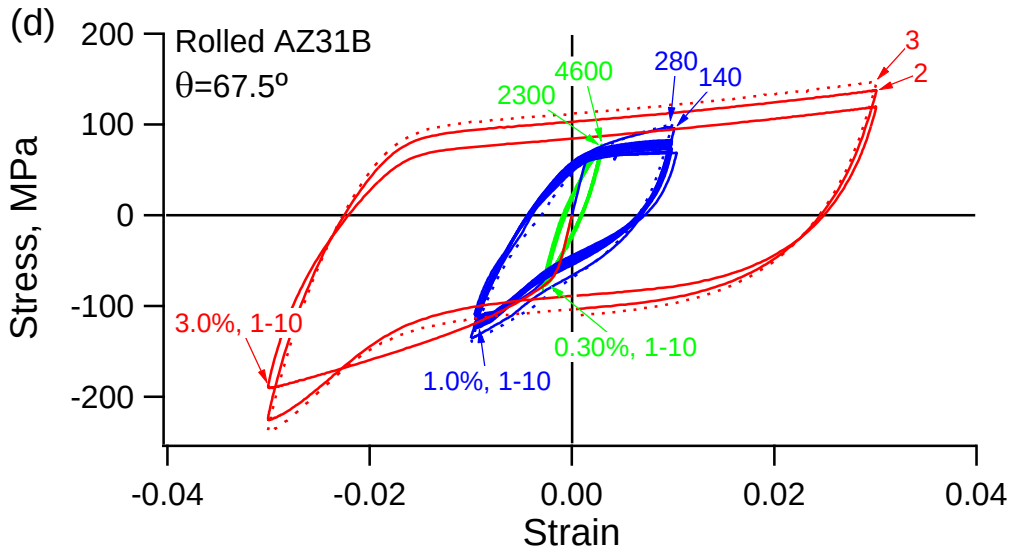
(d)
Rolled AZ31B
θ=67.5º
4600
2300
280
140
3
2
3.0%, 1-10
0.30%, 1-10
1.0%, 1-10
Stress, MPa
Strain
200
100
0
-100
-200
-0.04
-0.02
0.00
0.02
0.04

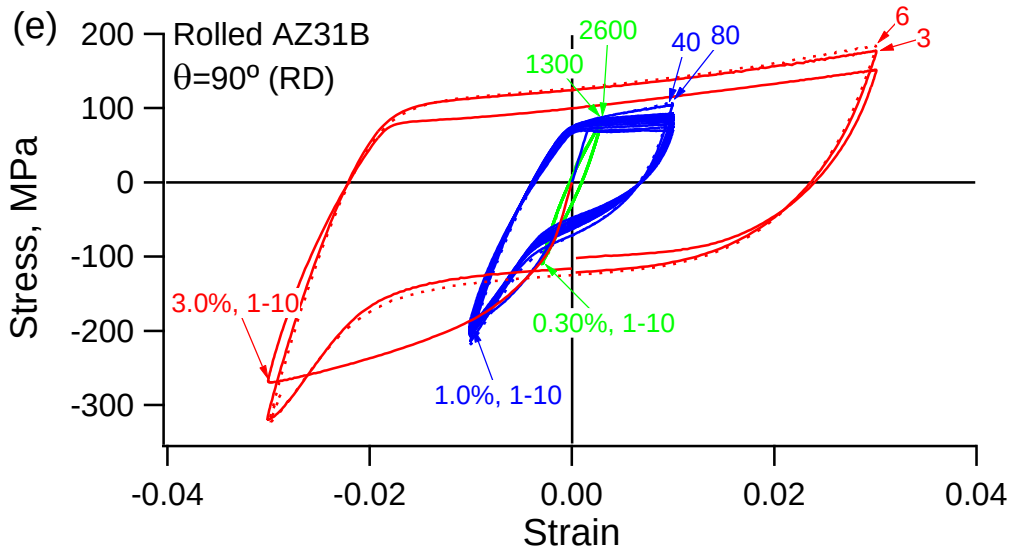

Fig. 5.1: Cyclic stress-strain hysteresis loops obtained from fully reversed strain-comtrolled fatigue experiments: (a) 0º (RD), (b) 22.5º, (c) 45º, (d) 67.5º and (e) 90º(ND).

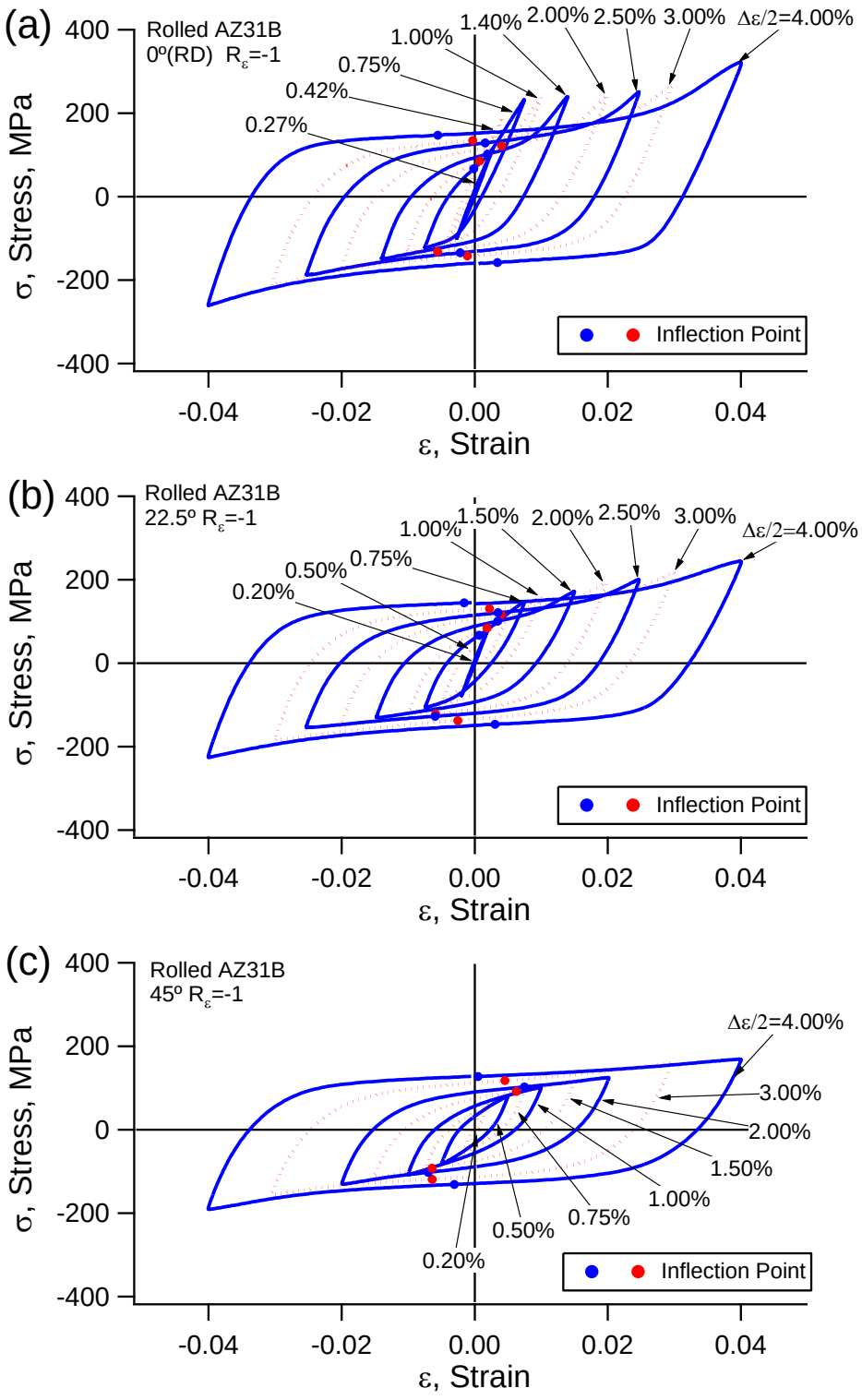
(a)
Rolled AZ31B
0º(RD) Rε=-1
0.27%
0.42%
0.75%
1.00%
1.40%
2.00%
2.50%
3.00%
Δε/2=4.00%
Inflection Point
σ, Stress, MPa
ε, Strain
(b)
Rolled AZ31B
22.5º Rε=-1
0.20%
0.50%
0.75%
1.00%
1.50%
2.00%
2.50%
3.00%
Δε/2=4.00%
Inflection Point
σ, Stress, MPa
ε, Strain
(c)
Rolled AZ31B
45º Rε=-1
Δε/2=4.00%
3.00%
2.00%
1.50%
1.00%
0.75%
0.50%
0.20%
Inflection Point
σ, Stress, MPa
ε, Strain

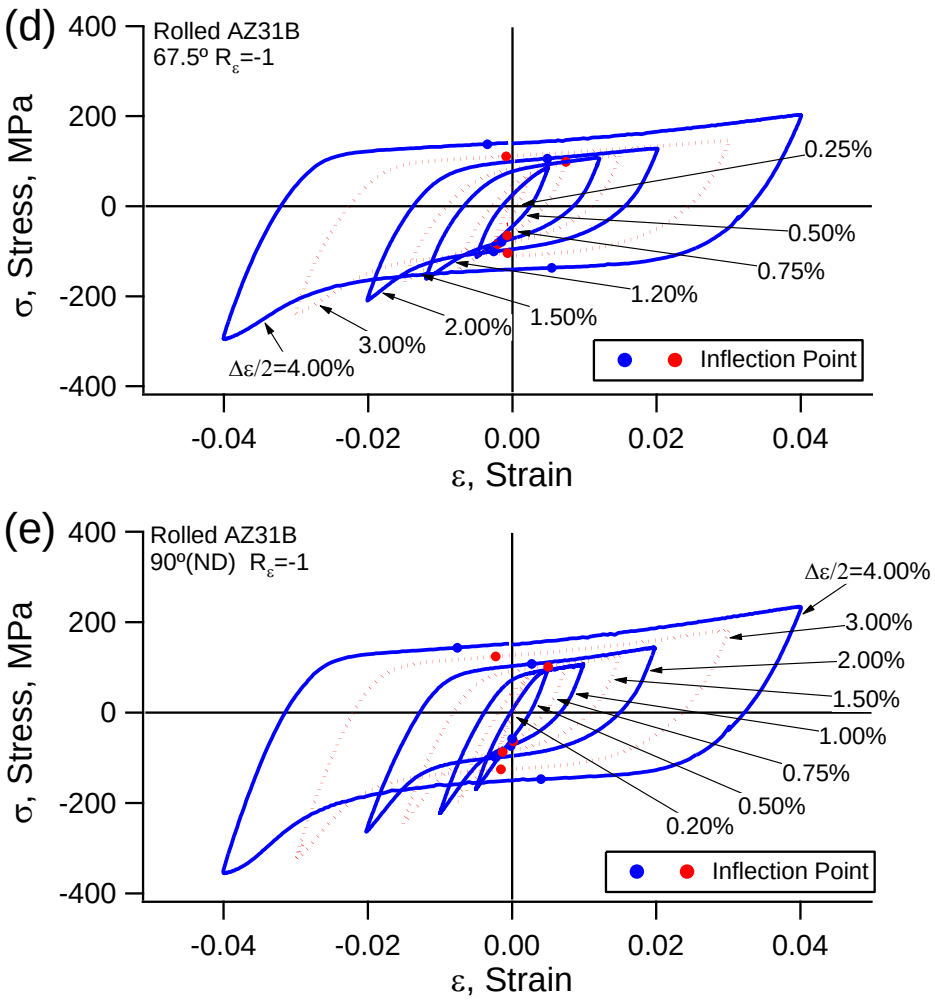

Fig. 5.2: Stabilized stress-strain hysteresis loops: (a) 0º (RD), (b) 22.5º, (c) 45º, (d) 67.5º and (e) 90º(ND).

When the strain amplitude is lower than the lower kink point, a detailed observation of the stress-strain hysteresis loops reveals that the shape is symmetrical with both the upper and lower branches of the stress-strain hysteresis loops being a concave or convex shape for all the five material orientations. No persistent twinning-detwinning occurs during fatigue loading. Such an observation is consistent with that made on extruded Mg alloys tested in the extrusion direction [50,52,58,86,109,117,118,138].

For fully reversed strain-controlled loading with the strain amplitude higher than the lower kink point, the compression reversal results in twinning and the tension reversal results in detwinning when the material orientation θ is less than 45º. When θ is larger than 45º, twinning occurs in the tension reversal and detwinning occurs during compression reversal. When the strain amplitude is higher than the lower kink point but less than the upper kink point, the detwinning loading reversal forms a sigmodal shape while the twinning reversal results in either a concave or convex shape. In this case, a sigmodal shape contains an inflection point which is an indicator of completion of detwinning and start of non-basal slips.

For all the five material orientations when the strain amplitude is above the upper kink point, both the upper and lower branches of the stress-strain hysteresis loop exhibit a sigmodal shape and therefore, there are two inflection points in a stress-strain hysteresis loop. In addition, the shape of the hysteresis loop tends to be more symmetric as the strain amplitude increases. For the material orientation $\theta < 45º$, the compression loading reversal is characterized by twinning and non-basal slips. The inflection point in the lower branch of the hysteresis loop signifies a start of non-basal slips with continuous twinning. During the tension loading reversal, which corresponds to the upper branch of the stress-strain hysteresis loop, detwinning occurs. The inflection point reflects the completion of detwinning and start of non-basal slips. The overall phenomenon is similar to that explained earlier for extruded Mg alloys loaded in the extrusion direction [50,52,58,86,109,116–118,120,122,139–143]. For the material orientation $\theta > 45º$, the inflection points represent the same characteristics but twinning occurs in the tension loading reversal and detwinning occurs in the compression reversals.

The variations of the stress amplitudes and the mean stress with the number of loading cycles under fully reversed strain-controlled loading reveal the cyclic hardening behavior of the material and are shown in Fig. 5.3 for the five material orientations. A glance of the results suggests that noticeable cyclic hardening occurs at a strain amplitude higher than the lower kink point for any material orientation, and a higher strain amplitude results in more significant cyclic hardening. Since a strain amplitude higher than the lower kink point is associated with persistent twinning-detwinning, it can be speculated that twinning-detwinning is the main contributor to the observed cyclic hardening in a Mg alloy. Another general observation from Fig. 5.3 is that positive mean stresses are found in the $\theta < 45^{o}$ material orientations and compressive mean stresses are accompanied in the $\theta > 45^{o}$ material orientations. The $\theta = 45^{o}$ material orientation has virtually zero mean stresses, which is consistent with the near symmetrical stress-strain hysteresis loops of the material orientation as shown in Fig. 5.3c.

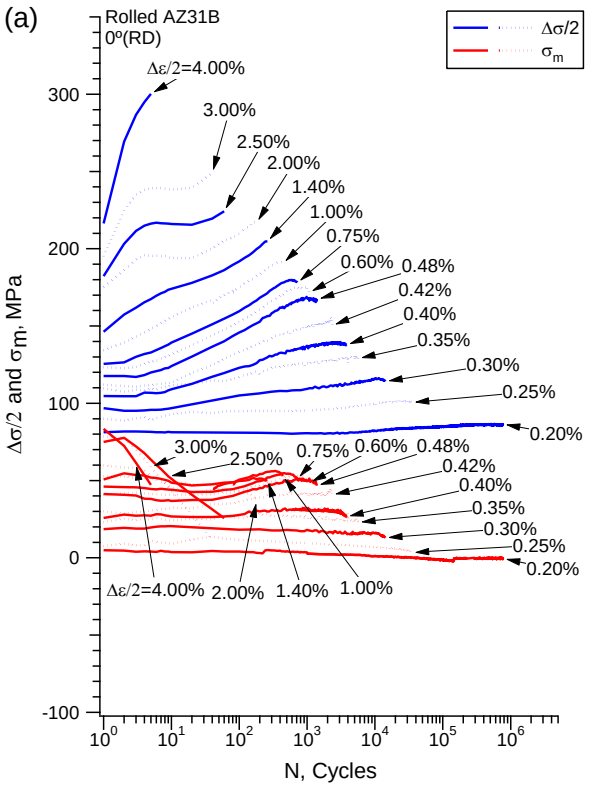
(a)
Rolled AZ31B
0º(RD)
Δσ/2
σm
Δε/2=4.00%
3.00%
2.50%
2.00%
1.40%
1.00%
0.75%
0.60%
0.48%
0.42%
0.40%
0.35%
0.30%
0.25%
0.20%
Δσ/2 and σm, MPa
N, Cycles

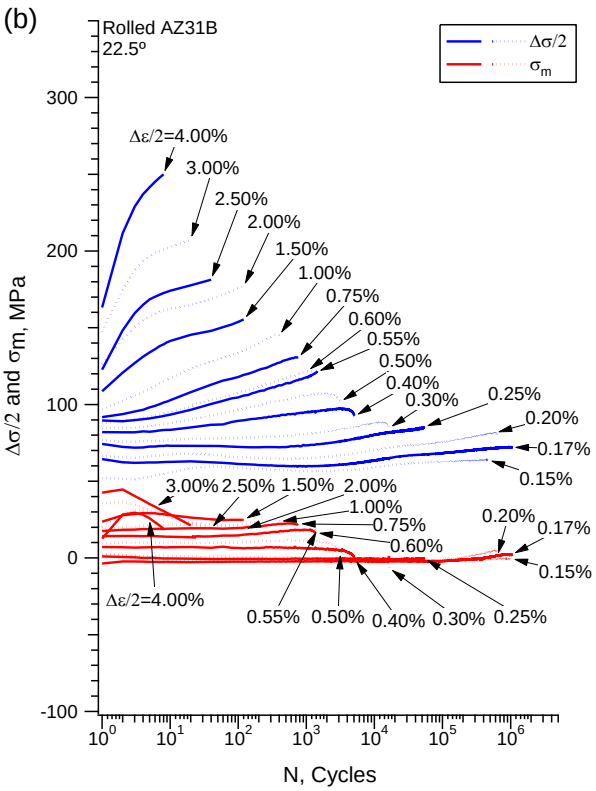
(b)
Rolled AZ31B
22.5º
Δσ/2
σm
Δε/2=4.00%
3.00%
2.50%
2.00%
1.50%
1.00%
0.75%
0.60%
0.55%
0.50%
0.40%
0.30%
0.25%
0.20%
0.17%
0.15%
Δσ/2 and σm, MPa
N, Cycles

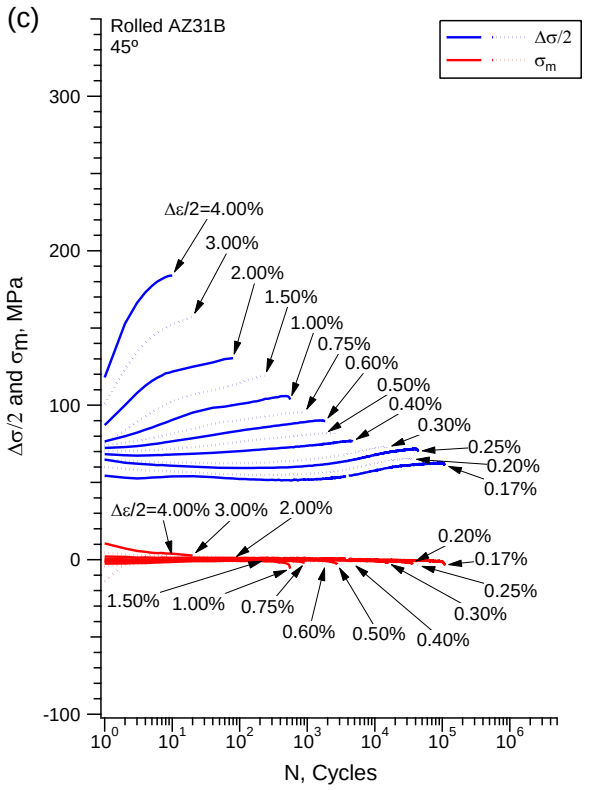
(c)
Rolled AZ31B
45º
Δσ/2
σm
Δσ/2 and σm, MPa
N, Cycles
Δε/2=4.00%
3.00%
2.00%
1.50%
1.00%
0.75%
0.60%
0.50%
0.40%
0.30%
0.25%
0.20%
0.17%

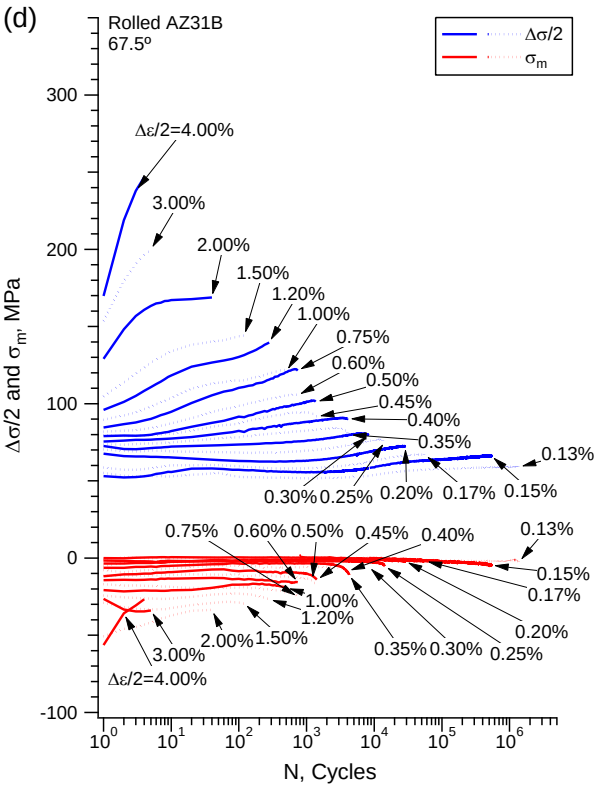
(d)
Rolled AZ31B
67.5º
Δσ/2
σm
Δσ/2 and σm, MPa
N, Cycles
Δε/2=4.00%
3.00%
2.00%
1.50%
1.20%
1.00%
0.75%
0.60%
0.50%
0.45%
0.40%
0.35%
0.30%
0.25%
0.20%
0.17%
0.15%
0.13%

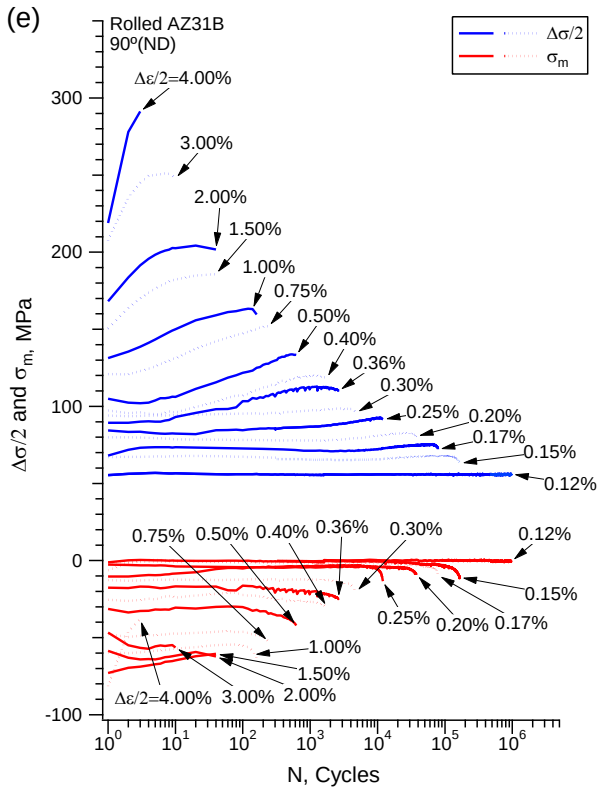

Fig. 5.3: Variations of stress amplitude and mean stress with the number of loading cycles: (a) 0º (RD), (b) 22.5º, (c) 45º, (d) 67.5º and (e) 90º (ND).

The stress-strain hysteresis loops in the RD and in the ND at identical strain amplitudes are similar after 180 degree rotation but not identical. Similarly, the hysteresis loops in the 22.5º and these in the 67.5º at identical strain amplitudes are similar after 180 degree rotation but not identical. Such an observation can be further collaborated with the results of the cyclic stress-plastic strain curves shown in Fig. 5.4 for the five material orientations. The vertical axis in Fig. 5.4 represents the stress amplitude of an experiment and the horizontal axis is the plastic strain amplitude which is equal to the strain amplitude subtracting the elastic strain amplitude. All the quantities are taken from the stress-strain hysteresis loop at approximately half fatigue life for each testing specimen. Overall, the

RD material orientation has the highest cyclic stress-plastic strain curve and the 45º orientation yields the lowest cyclic stress-strain curve.

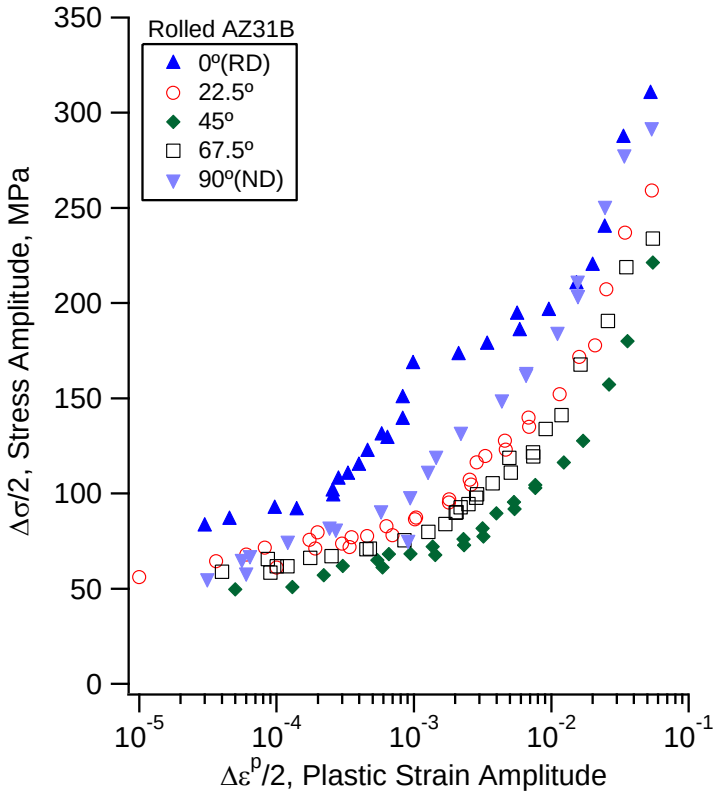

Fig. 5.4: Cyclic stress-plastic strain curves.

5.2 Detailed Plastic Deformation

In order to further explore the detailed plastic deformation, the stress-plastic strain hysteresis loops are examined which can provide insightful information on the cyclic deformation of the material. A schematic illustration of one stress-plastic strain hysteresis loop where the nonlinear elasticity is considered is shown in Fig. 5.5. The plastic strain is defined as follows:

$$\varepsilon_p = \varepsilon - \frac{\sigma}{E} \tag{1}$$

where,

$$E = E_0(1 - \frac{\sigma}{b}) \quad (2)$$

In Eqs. (1) and (2), ε_p is the plastic strain, ε and σ are the true strain and true stress, respectively, E is the elasticity modulus, b is a material constant for nonlinear elasticity of the material, and E_0 is the elasticity modules at the origin of the stress-strain curve. Nonlinear elasticity needs to be considered in order to better analyze the stress-plastic strain response. A simple linear dependence of the elasticity modulus on the applied stress (Eq. (2)) was adopted for considering the nonlinear elasticity of the material. For the rolled Mg alloy under investigation, b is equal to 12,000 MPa and 20,000 MPa can provide a good description of the nonlinearity for θ = 0º, 22.5º, 45º, and θ = 67.5º, 90º, respectively.

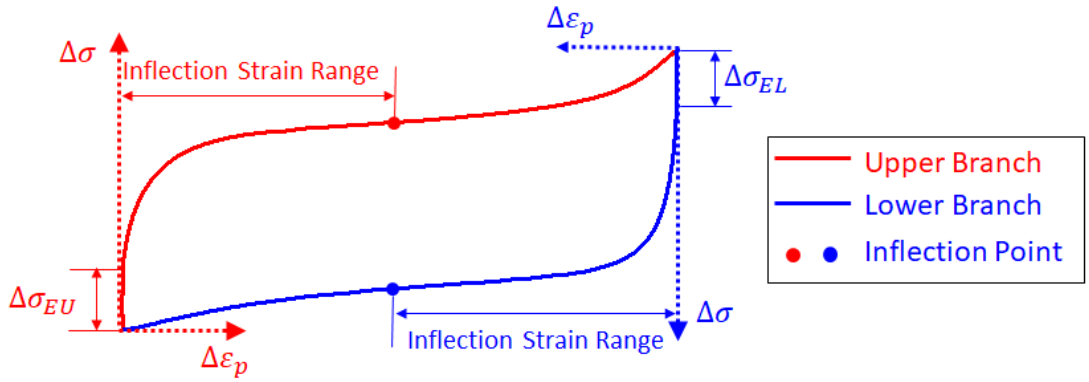

Fig. 5.5: Schematic stress-plastic strain hysteresis loop where the terminology used to describe cyclic plasticity of magnesium alloy are illustrated.

The upper and lower branches are marked by red and blue color, respectively. For the purpose of comparison, the origin of the $\Delta\sigma$-$\Delta\varepsilon_p$ coordinate system is located at the lower tip for the upper branch, and the upper tip for the lower branch. The elastic limit range is defined as the stress range which demarcates the elastic and elastic-plastic deformation during cyclic loading. The elastic limit ranges of the upper and lower branch are denoted by $\Delta\sigma_{EU}$ and $\Delta\sigma_{EL}$, respectively. The inflection point is mathematically defined as the point

where the second derivative of the stress with respect to the plastic strain is zero, signifying the transition of deformation mechanism from twinning/detwinning to non-basal slips during cyclic loading. The inflection strain range is defined as the plastic strain range between the inflection point and the origin of the $\Delta\sigma$-$\Delta\varepsilon_p$ coordinate system.

5.2.1 Stress-Plastic Strain Hysteresis Loops

Fig. 5.6 presents the stabilized stress-plastic strain hysteresis loops corresponding to approximately half fatigue lives at strain amplitudes of 0.30%, 1.00% and 3.00%. The results shown in Fig. 5.6 are consistent with those of stabilized stress-strain hysteresis loops in Fig. 5.2.

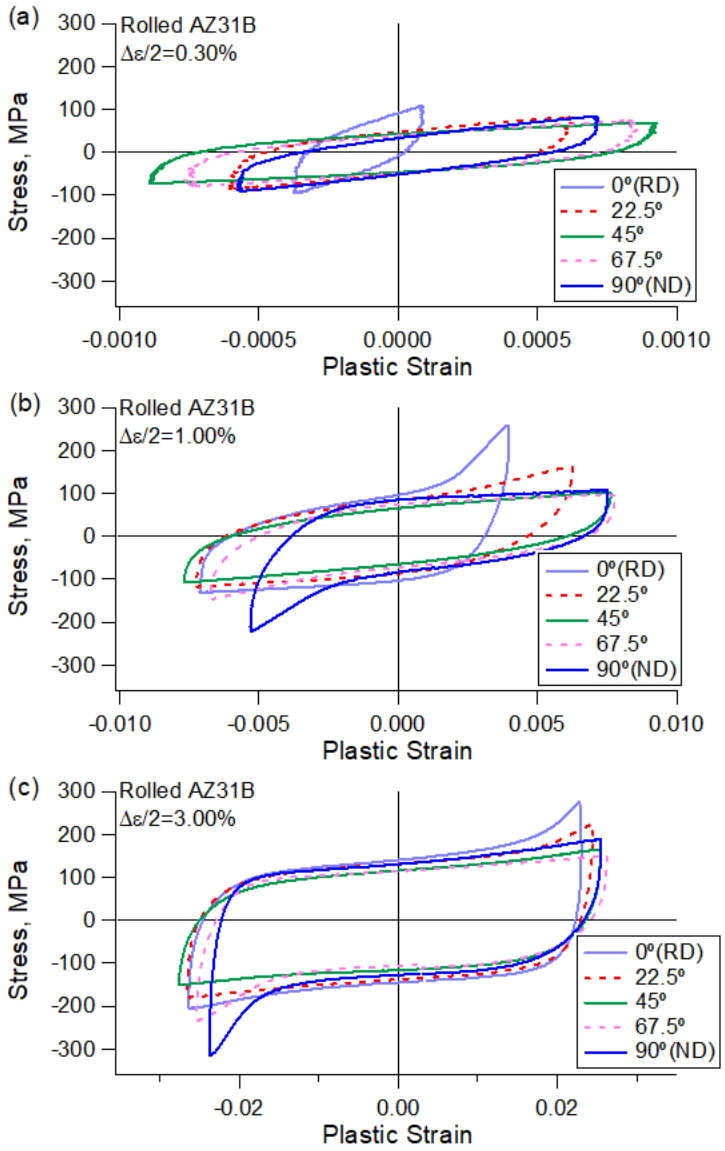

Fig. 5.6: Stabilized stress-plastic strain hysteresis loops of three representative strain amplitudes under fully strain-controlled loading: (a) $\Delta\varepsilon/2=0.30\%$, (b) $\Delta\varepsilon/2=1.00\%$ and (c) $\Delta\varepsilon/2=3.00\%$.

When the strain amplitude is 0.30%, the shape of the stress-plastic strain hysteresis loops is symmetrical with both the upper and lower branches being a concave or convex shape for all the five orientations. These symmetrical stress-plastic strain hysteresis loops indicate that no persistent twinning-detwinning occurs during the cyclic loading and

dislocation slips dominate the deformation mechanism. As the strain amplitude increases to 1.00%, the shape of the upper branches and the lower branches of the stress-plastic strain hysteresis loops is symmetrical only when $\theta = 45^{o}$. When $\theta < 45^{o}$, the lower branch forms a concave-up shape while the upper branch forms a sigmoidal shape. These asymmetrical lower and upper branches indicate that twinning involves in the compression reversal and detwinning involves in the tension reversal followed by the non-basal slips. When $\theta > 45^{o}$, the lower branch and upper branch exhibit a sigmoidal and concave-down shape, respectively. Twinning occurs in the tension reversal and detwinning occurs during compression reversal. Non-basal slips only occur after detwinning. At a large strain amplitude of 3.00%, both the lower branches and the upper branches of the stress-strain hysteresis loop exhibit a sigmoidal shape. The plastic deformation mechanism is similar to that when the strain amplitude is 1.00%, except that non-basal slips occur in both tensile and compressive reversals. For example, when $\theta < 45^{o}$, the compression loading reversal is characterized by twinning followed by non-basal slips, and the tension loading reversal is associated with detwinning followed by non-basal slips.

One salient feature that can be observed in Fig. 5.6 is that the stabilized stress-plastic strain hysteresis loops at $\theta = 45^{o}$ remains symmetrical at all the three representative strain amplitudes. However, the shape of the hysteresis loop with a strain amplitude of 3.00% shows a slight difference as compared with those of strain amplitude of 0.30% and 1.00%. When the strain amplitudes are 0.30% and 1.00%, the lower branches exhibit a concave-up shape while the upper branches exhibit a concave-down shape. When the strain amplitude increases to 3.00%, both the lower and upper branches form a sigmoidal shape.

The tension reversal and the compression reversal are characterized by the same deformation mechanism which will be discussed in the next section.

5.2.2 Stress Range-Plastic Strain Range Curves

In order to understand how the deformation mechanism depends on the loading cycles, the $\Delta\sigma$-$\Delta\varepsilon_p$ curves of selected loading cycles at the three representative strain amplitudes, 0.30%, 1.00% and 3.00%, are plotted in Fig. 5.7, Fig. 5.8, and Fig. 5.9, respectively. For comparison, the origins of the lower branch as well as the upper branch were plotted in the same $\Delta\sigma$-$\Delta\varepsilon_p$ coordinate system.

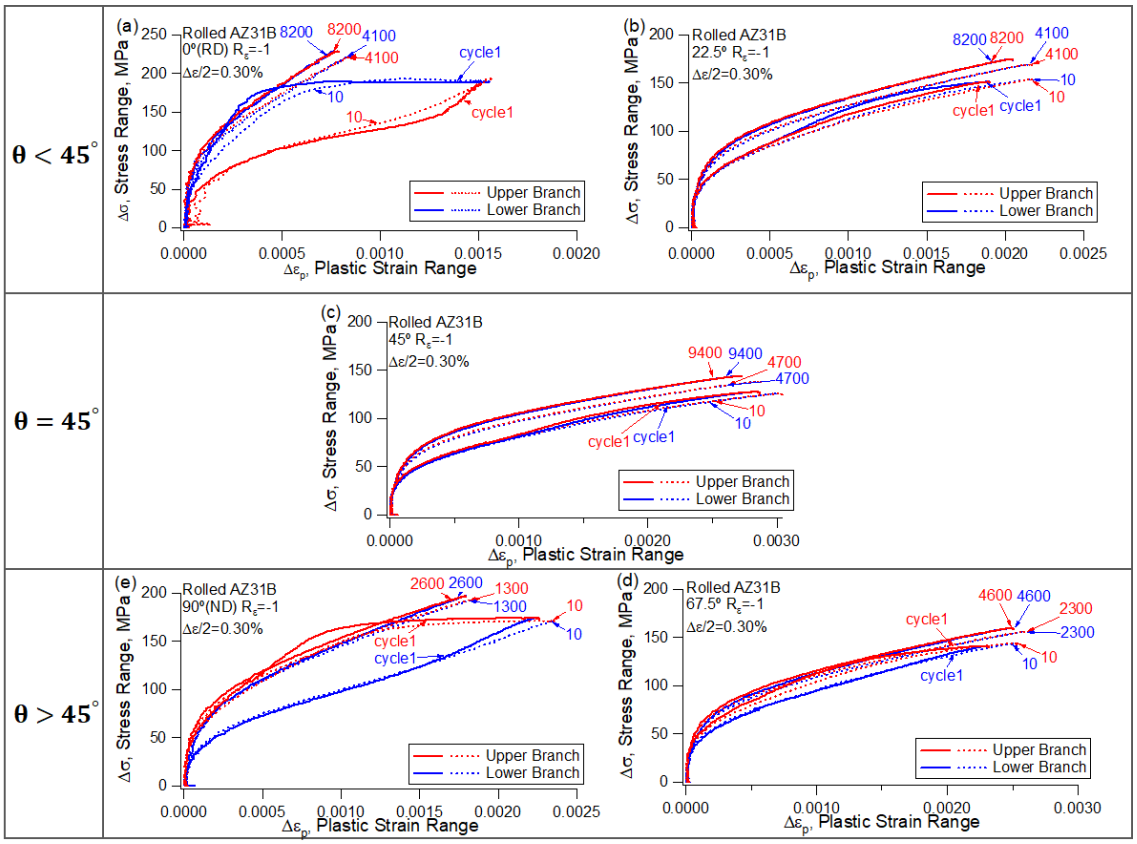

Fig. 5.7: Stress range versus plastic strain range for the selective loading cycles at $\Delta\varepsilon/2$=0.30%: (a) 0º (RD), (b) 22.5º, (c) 45º, (d) 67.5º and (e) 90º (ND).

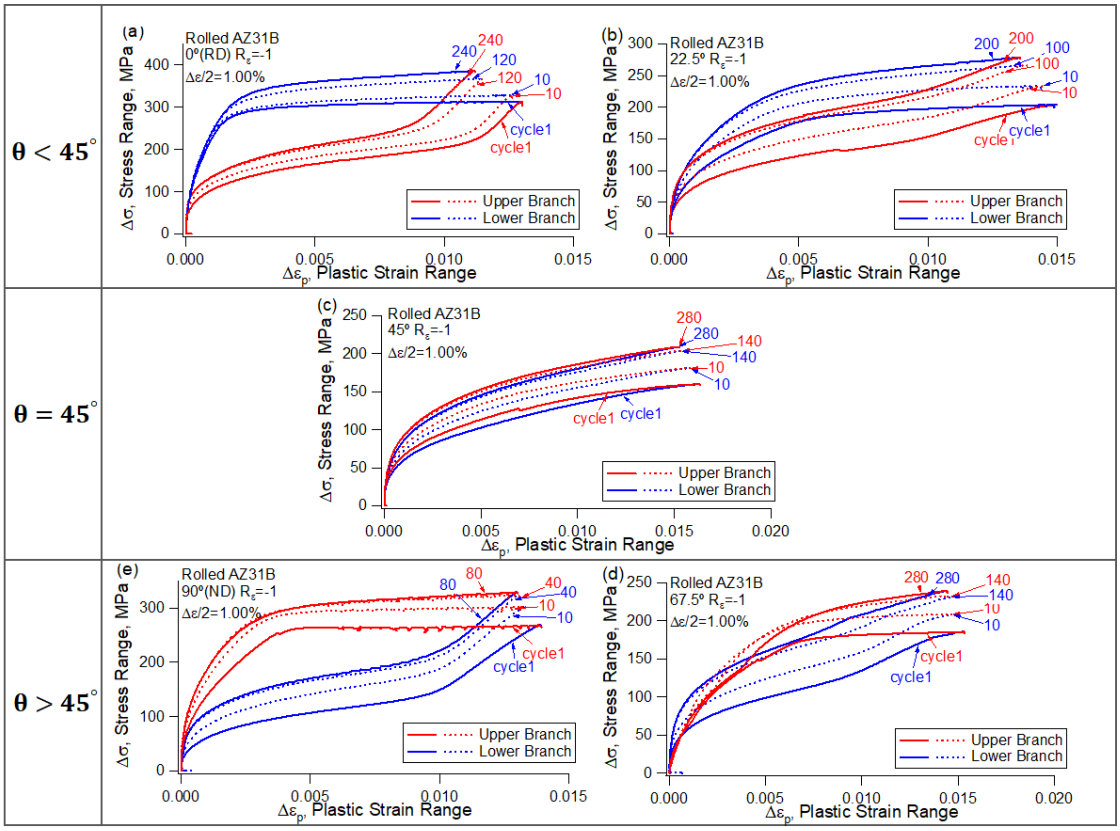

Fig. 5.8: Stress range versus plastic strain range for the selective loading cycles at Δε/2=1.0%: (a) 0º (RD), (b) 22.5º, (c) 45º, (d) 67.5º and (e) 90º (ND).

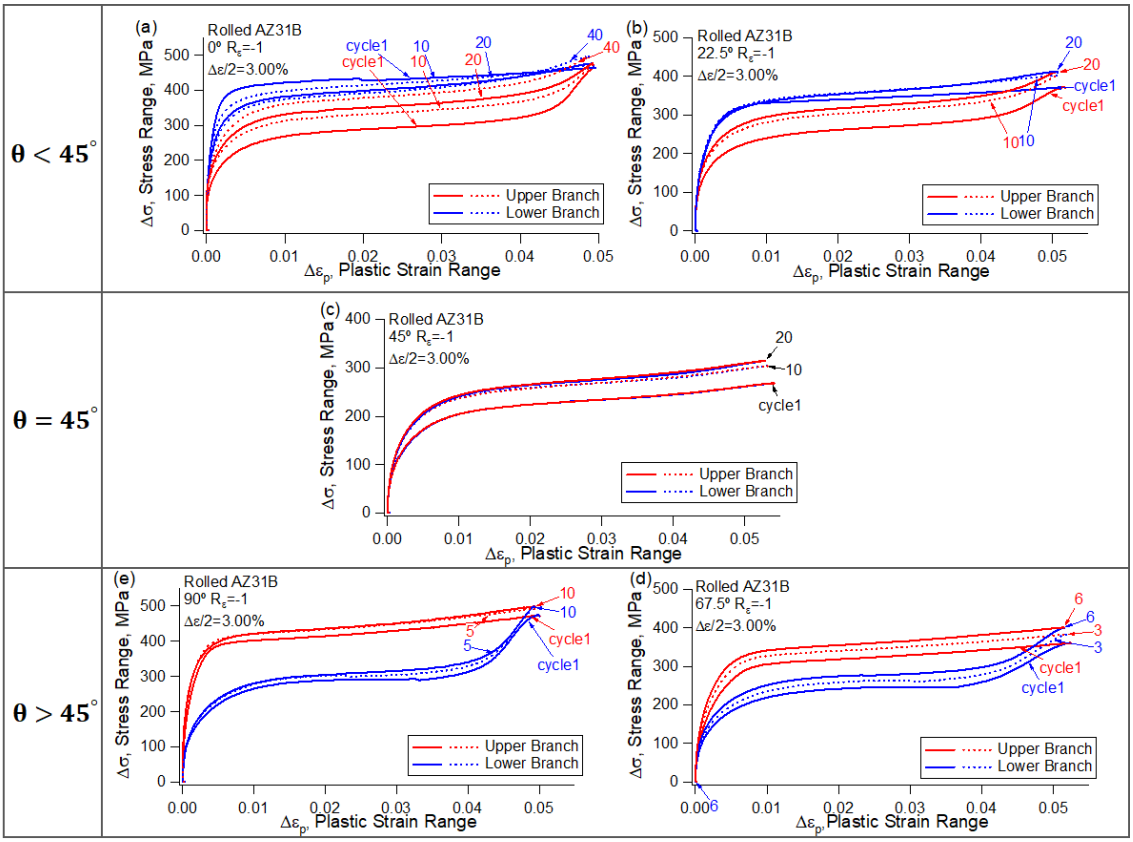

Fig. 5.9: Stress range versus plastic strain range for the selective loading cycles at Δε/2=3.00%: (a) 0º (RD), (b) 22.5º, (c) 45º, (d) 67.5º and (e) 90º (ND).

When the strain amplitude is 0.30%, the upper branches and the lower branches display a prominent asymmetry shape at the initial deformation stage from cycle 1 to cycle 10 when θ = 0º and 90º, as shown in Figs. 5.7a and e. For θ = 22.5º and 67.5º, the shape of the upper branches and the lower branches for the first 10 cycles exhibits a less degree of asymmetry comparing with those of 0º and 90º. That is due to the fact that twinning is more likely to occur under compression reversals in the 0º case and under the tension reversals in the 90º case. The shape tends to be more symmetric with the increase of loading cycles. The asymmetry shape during the initial deformation stage is due to the involvement of twinning-detwinning activity. With the increase of loading cycles, the twinning-

detwinning activity gradually diminishes, resulting in the symmetrical shape for the upper branches and lower branches in the later deformation stage.

Fig. 5.8 shows the stress range versus plastic strain range for the selective loading cycles at different loading directions when the strain amplitude is 1.00%. It can be seen that both the upper and the lower branches display asymmetric shapes at all the loading directions except the 45º orientation, regardless of loading cycle. A sigmoidal shape can be observed at the upper branch for θ < 45º and the lower branch for θ > 45º. Similar to Fig. 5.7, the $\Delta\sigma$-$\Delta\varepsilon_p$ curves for 0º and 90º exhibit a more asymmetrical shape comparing with those for 22.5º and 67.5º. When the applied strain amplitude is above the lower kink point, sustainable twinning-detwinning occurs throughout the whole cyclic loading. More twinning-detwinning activity are involved in the 0º and 90º than in the 22.5º and 67.5º cases.

Fig. 5.9 shows the stress range versus plastic strain range for the selective loading cycles at different loading directions when the strain amplitude is 3.00%. It can be observed that the upper and the lower branches all the cases except θ = 45º display a less asymmetry shape comparing with the result in Fig. 5.8 when strain amplitude is 1.00%. This phenomenon is due to the fact that non-basal slips occur in both tension and compression reversals during a loading cycle for all five material orientations. When the strain amplitude is above the upper kink point, detwinning is always finished followed with non-basal slips while non-basal slips start to occur concurrently with twinning during the subsequent loading reversal.

One noticable charactersitics of the cylic deformation behavior of Mg alloys shown in Figs. 5.8-5.9 is that the upper branches and the lower branchs remain symmetric when the

material orientation θ = 45º despite the different deformation mechanisms involved at the three different strian amplitudes. Only basal slips occur during the cyclic loading at a strain amplitude of 0.30%, resulting in the symmetrical upper branches and lower branches. As the strain amplitude is increased to 1.00% and 3.00%, sustainable twinning-detwinning activity dominated the cyclic deformation. Twinning is more difficult to occur for θ = 45º comparing with the other four material orientations. However, both twinning and detwinning occur during both tension and compression reversals, which leads to the observed symmetrical $\Delta\sigma$-$\Delta\varepsilon_p$ curves in 45º material orientation when the applied strain amplitude is above the lower kink point.

5.2.3 Elastic Limit Ranges

The elastic limit range is defined as the stress range from the start of a loading reversal to the yielding point, and it demarcates the elastic and elastic-plastic deformation during cyclic loading (refer to Fig. 5.5). Observing the elastic limit range values can provide significant information about the characteristics of the cyclic deformation.

The evolution of elastic limit range in the neighborhood near the two kink points in the strain-life curve:

The evolution of the elastic limit ranges with the number of loading cycles at two representative strain amplitude is plotted in Fig. 5.10 for each material orientation. The two representative strain amplitudes were taken from the neighborhood near the two kink points identified in the strain-life curves. For each material orientation in Fig. 5.10, the lower strain amplitude is taken near the lower kink point and the higher strain amplitude is taken near the upper kink points. The results shown in Fig. 5.10 provide detailed information

about how the deformation behavior change with loading cycles in the neighborhood near the kink points.

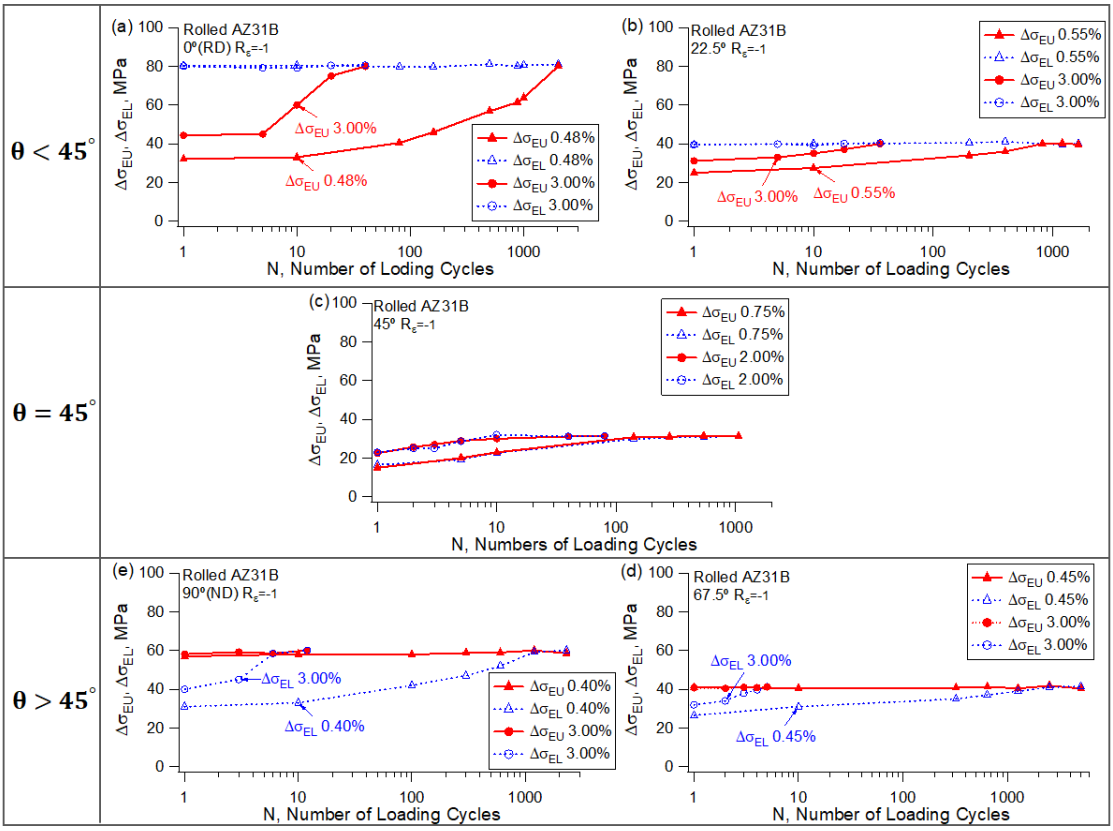

Fig. 5.10: Variations of the elastic limit ranges ($\Delta\sigma_{EU}$ and $\Delta\sigma_{EL}$) with respect to the increasing number of loading cycles at two representative strain amplitudes: (a) 0º (RD), (b) 22.5º, (c) 45º, (d) 67.5º and (e) 90º (ND).

One salient feature that can be observed in Fig. 5.10 is that the $\Delta\sigma_{EL}$ (the elastic limit range of the lower branches) for θ < 45º and $\Delta\sigma_{EU}$ (the elastic limit range of the upper branches) for θ > 45º is a constant value and irrespective of the loading cycles and applied strain amplitude. While on the subsequent loading reversals, the $\Delta\sigma_{EU}$ for θ < 45º and $\Delta\sigma_{EL}$ for θ > 45º is dependent on the loading cycles as well as applied strain amplitude and gradually increases with increasing number of loading cycles. Under fully reversed strain-controlled cyclic loading, twinning can be activated during the compressive loading

reversals for θ < 45º and tensile reversals for θ > 45º, and detwinning can be activated during the subsequent loading reversals. The different deformation mechanisms under tension and compression results in the distinct evolution behavior of the elastic limit range under different loading directions, for the five material orientations.

When the applied strain amplitude is in the neighborhood near the lower kink point, it can be observed in Fig. 5.10 that the elastic limit range values on the tension reversals and compression reversals exhibit a significant difference at the first ten loading cycles when $\theta \neq 45º$. A distinct lower elastic limit range value can be observed on the tension reversals ($\Delta\sigma_{EU}$) for θ < 45º and compression reversals ($\Delta\sigma_{EL}$) for θ > 45º, where detwinning is favorable. The values are gradually increased with increasing number of loading cycles, being stable when the loading cycles exceed half-fatigue lives. For example, when the material orientation is 0º with a strain amplitude of 0.48%, $\Delta\sigma_{EU}$ was approximately 31 MPa for the initial 10 loading cycles and increased to 80 MPa when the loading cycles reached 1,000. This phenomenon indicates that twining-detwinning activity is involved in the earlier loading stage, and gradually diminishes as the number of loading cycles increase.

The EBSD scans on the tested specimens after the fatigue tests at an applied strain amplitude near the lower kink point are shown in Fig. 5.11. It can be observed that residual twins can be barely observed after the fatigue experiments at the strain amplitude near the lower kink point. This observation indicates that twinning/detwinning activity gradually diminished during the cyclic loading. At the loading cycles after the half-fatigue lives, very limited twinning/detwinning is involved during the cyclic loading and basal slips dominate the plastic deformation. It can be inferred that the TVF at the peak strain prior to the loading reversal which is favorable for detwinning gradually decreases as the number of loading

cycles increases. Therefore, the elastic limit range on the subsequent loading reversal increases with the number of loading cycles.

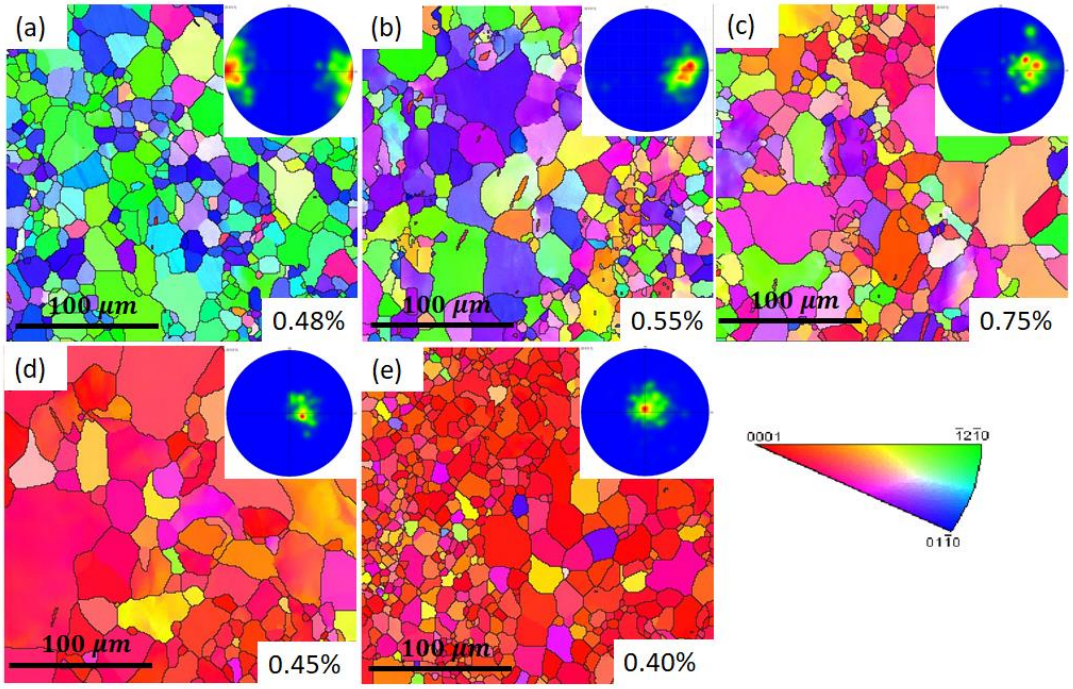

Fig. 5.11: EBSD scans on the tested specimens after the fatigue tests at an applied strain amplitude near the lower kink point: (a) 0º (RD) at Δε/2=0.48%, (b) 22.5º at Δε/2=0.55%, (c) 45º at Δε/2=0.75%, (d) 67.5º at Δε/2=0.45% and (e) 90º (ND) at Δε/2=0.40%.

As the applied strain amplitude is as high as in the neighborhood near the upper kink point, a distinct characteristic can be observed in Fig. 5.10 is that the elastic limit range values on the tension reversals ($\Delta\sigma_{EU}$) for θ < 45º and compression reversals ($\Delta\sigma_{EL}$) for θ > 45º where detwinnng is favorable keep increasing until the number of loading cycles approach the fatigue life cycle. This phenomenon is due to the fact that sustainable twinning-detwinning is involved throughout the whole loading stage when the strain amplitude is as high as the upper kink point. Moreover, the elastic limit ranges indicating the activation stress for detwinning at the first loading cycle is higher than those with lower strain amplitudes. This feature is a result from the fact that more twinning is generated

when the strain amplitude is higher, leading to a higher activation stress for detwinning during the subsequent loading reversal.

The evolution of elastic limit range with the number of loading cycles for the 45º material orientation is shown in Fig. 5.10c. Besides the distinct phenomenon that the upper branch and the lower branch exhibit approximately identical elastic limit ranges values, another silent feature can be observed in Fig. 5.10c is that during the initial 10 loading cycles, the elastic limit range values at the strain amplitude of 2.00% is larger than that of 0.75%. The elastic limit ranges gradually increase with increasing number of loading cycles and keep a stable value of 31 MPa after the number of loading cycles reaches the half-life cycle for both strain amplitudes.

Relationship between the elastic limit range and the applied strain amplitudes:

The elastic limit range as a function of the applied strain amplitude at half-fatigue life is plotted in Fig. 5.12 for the five material orientations. The strain amplitudes corresponding to the lower and upper kink points are marked by two dashed lines. A feature that can be observed in Fig. 5.12 is that $\Delta\sigma_{EL}$ for $\theta < 45^{o}$ and $\Delta\sigma_{EU}$ for $\theta > 45^{o}$ is a constant value and is independent of the applied strain amplitude. In contrast, $\Delta\sigma_{EU}$ for $\theta < 45^{o}$ and $\Delta\sigma_{EL}$ for $\theta > 45^{o}$ depends on the strain amplitude and the relationship between the elastic limit range and the applied strain amplitude displays a check-marker shape. Similar to the results represented in Fig. 5.10, the different evolution feature for the upper and the lower branches is due to the different deformation mechanisms under tension and compression. Moreover, the 45º material orientation exhibits a distinct characteristic. $\Delta\sigma_{EU}$ and $\Delta\sigma_{EL}$ are approximately identical and are dependent on the strain amplitude when $\theta = 45^{o}$.

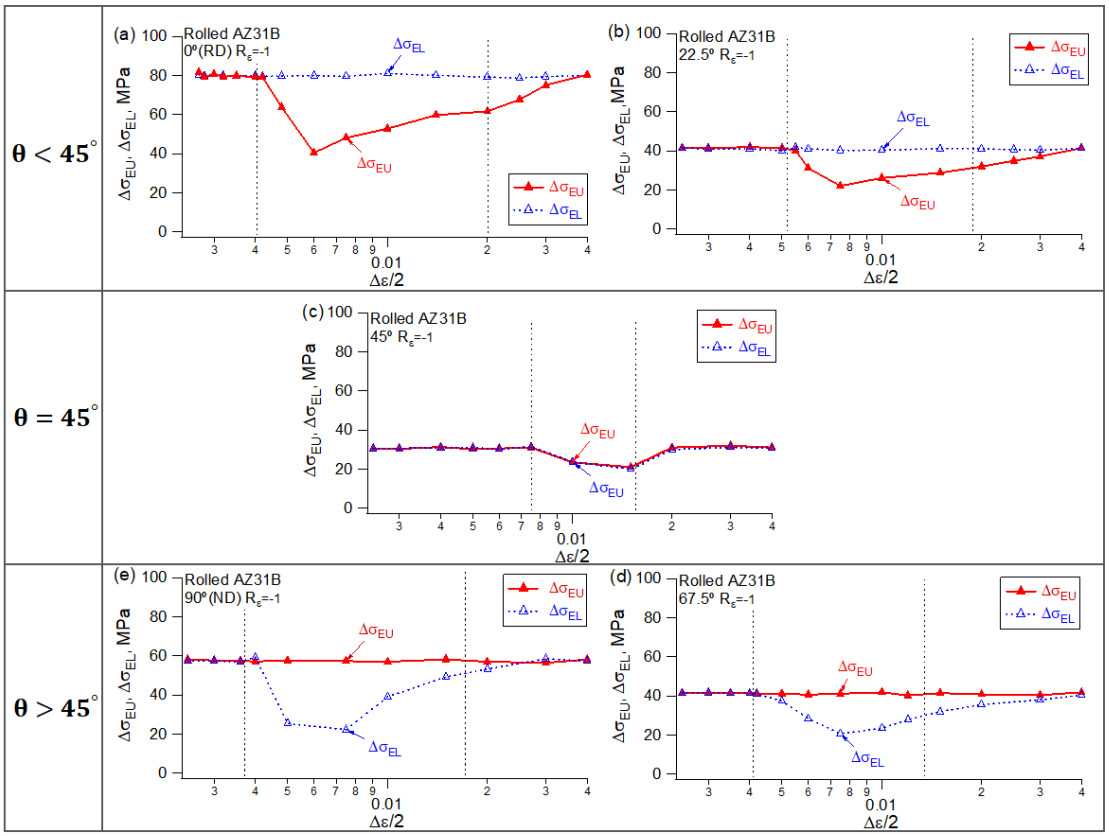

Fig. 5.12: Relationship between the elastic limit range and the applied strain amplitudes at half-fatigue life under fully reversed strain-controlled loading: (a) 0º (RD), (b) 22.5º, (c) 45º, (d) 67.5º and (e) 90º (ND).

When the applied strain amplitude exceeds the lower kink point (the first dashed line), a dramatic drop of $\Delta\sigma_{EU}$ for θ < 45º and $\Delta\sigma_{EL}$ for θ > 45º can be observed in Fig. 5.12. When the strain amplitude is below the lower kink point, the stabilized cyclic plastic deformation is due to basal slips without involving twinning-detwinning for the five material orientations. $\Delta\sigma_{EU}$ and $\Delta\sigma_{EL}$ display approximately the same value, reflecting the activation stress range for basal slip during cyclic loading. Sustainable twinning-detwinning activity occurs as the applied strain amplitude is higher than the lower kink point, resulting the dramatic drop of $\Delta\sigma_{EU}$ for θ < 45º and $\Delta\sigma_{EL}$ for θ > 45º. As the strain amplitude increases, the twin volume fraction (TVF) at the minimum stress for θ < 45º and

maximum stress for $\theta > 45^{o}$ increases. Correspondingly, the twin bands grow and become wider, resulting in a multiplication of twin boundaries. The slips activated in the twins can interact with twin boundaries. Slip dislocations and twin dislocations pile up and pin at the twin boundaries. These pinned dislocations at twin boundaries decrease the mobility of twin boundaries and make the formed twin bands more stable. Such a process makes the detwinning process more difficult in the subsequent loading cycles. Consequently, the detwinning process requires a higher driving force to shrink the twinned area when a greater amount of twin bands with wider shape exist at a larger strain amplitude. Macroscopically shown in Fig. 5.12, the $\Delta\sigma_{EU}$ for $\theta < 45^{o}$ and $\Delta\sigma_{EL}$ for $\theta > 45^{o}$ begin to increase after the dramatic drop. At a strain amplitude of 4.00%, the $\Delta\sigma_{EU}$ for $\theta < 45^{o}$ and $\Delta\sigma_{EL}$ for $\theta > 45^{o}$ go back to the initial constant value and the elastic limit range indicates the activation stress for basal slips.

Fig. 5.12c presents the relationship between the elastic limit range and the applied strain amplitude for the 45º material orientation at the half-fatigue life cycle. In Fig. 5.12c, $\Delta\sigma_{EU}$ and $\Delta\sigma_{EL}$ keep a constant value of approximately 30 MPa when the strain amplitude is below 0.75%. As the strain amplitude increases, the elastic limit range at the half-life cycle begins to drop. The value decreases to 20 MPa when the strain amplitude is 1.5%, and then starts to increase until it reaches a stable value of 30MPa. The unique deformation behavior for $\theta = 45^{o}$ is discussed in section 5.3.

5.2.4 Inflection Strain Ranges

During fully reversed cyclic loading, twinning occurs under the compression reversals for $\theta < 45^{o}$ and tension reversals for $\theta > 45^{o}$. The inflection points on these loading reversals signify the activation of non-basal slips. Therefore, the inflection strain range refelcts the

strain range to reach twinning exhaustion. Fig. 5.13 shows the inflection strain ranges on the upper branches and lower branches at half-live cycle as a function of the appplied strain amplitude for all the five material orientations. The strain values corresponding to the lower and upper kink points were marked by vertial dashed lines in Fig. 5.13. It can be seen that the inflection points exist only when the applied strain amplitude is above the lower kink point. Both the inflection strain ranges on the upper and lower branch increase with the increasing strain amplitudes. With a larger strain amplitude under fully reversed loading, more tension twins are activated, resulting in more tension twins being detwinned during the subsequent loading reversal. Therefore, twinning/detwinning dominates the plastic deformation to a prolonged extent at larger strain amplitudes, resulting in larger inflection strain ranges. It is noticed that when the applied strain amplitude is approaching the upper kink point, the inflection strain ranges on the lower branches are approximately equal to those on the upper branches. For the $\theta = 45^{o}$ material orientation, the inflection points can only be identified when the strain amplitude is as high as 1.5%, indicating that limited twinning-detwinning activity is involved in the cyclic deformation.

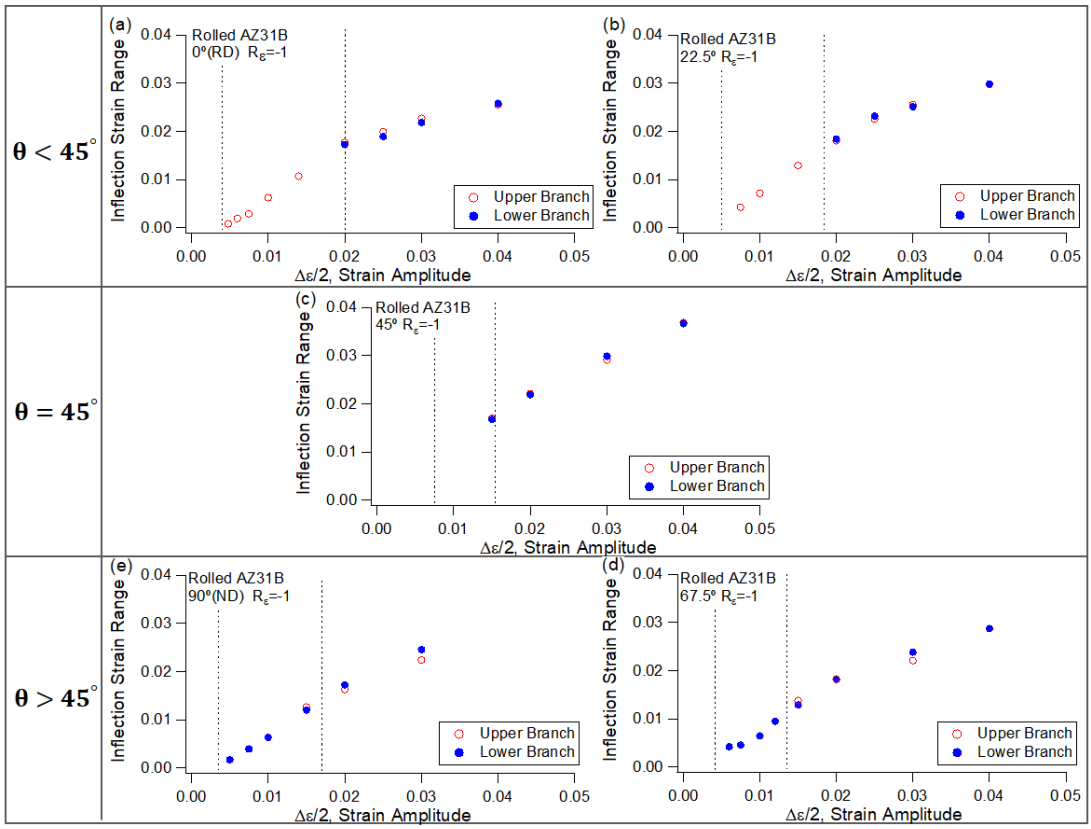

Fig. 5.13: Inflection strain ranges as a function of the applied strain amplitudes under fully reversed strain-controlled loading: (a) 0º (RD), (b) 22.5º, (c) 45º, (d) 67.5º and (e) 90º (ND).

5.3 θ = 45º Material Orientation

The results obtained from testing 45º material orientation deserve a further discussion. There are six crystallographic equivalent tension twin variants in an HCP Mg crystal. Associated with each variant, there is a corresponding value that correlates to the resolved shear stress of the twin plane along the twin direction. This value, called Schmid factor (SF), is often used in twin variant selection analysis [144,145]. When analyzing a grain, the largest SF among those of the six variants is used when discussing twinning. Assuming a perfect *c*-axis alignment in the ND of the rolled plate (refer to Fig. 3.1), the maximum SF of the six $\{10\bar{1}2\}$ tension twinning variants is 0.25 for the 45º orientation. While still large

enough to activate twinning, this value is the smallest among the five material orientations and, as a result, twinning is more difficult to occur for the 45º material orientation.

Fig. 5.14 shows the EBSD results after the 45º orientation specimens were loaded at a strain amplitude of 2.0% for 40 loading cycles and terminated at 2.00% and -2.00%, respectively, before unloading to zero stress. Accounting for the distribution of *c*-axis of the grains in the rolled polycrystalline Mg alloy, three grain orientation types are examined by EBSD based on their favorability to twin: grains that are favorable for twinning under compression (G_1, G_2, G_7, G_8), grains that are not favorable for twinning under both compression and tension (G_3, G_4, G_9, G_{10}), and grains that are favorable for twinning under tension (G_5, G_6, G_{11}, G_{12}). Grains favorable for twinning typically have a SF larger than 0.25 based on the statistics among approximately 70 grains examined in the observation areas shown in the EBSD IPF maps (Fig. 5.14). With high positive SF values, twinning occurs in G_1 and G_2 under compression. Simultaneously with the occurrence of twinning in G_1 and G_2, detwinning is expected to occur in G_5 and G_6. This is because twinning is very likely to have occurred in G_5 and G_6 during the previous tension loading reversal due to their high SF values. In G_5, a few residual twins are visible, and the twins formed during tensile loading in G_6 are expected to have been completely detwinned at the end of the compression reversal. No twinning-detwinning occurs in G_3 and G_4. Similar observations can be made from the results terminated at 2.00% (tension) after 40 loading cycles. G_{11} and G_{12}, due to large positive SF values, experience twinning under tensile loading, and during the same tensile loading reversal, detwinning occurs in G_7 and G_8. An analysis of the twin in G_8 indicates that it is a residual twin formed during previous compression

loading. No twinning or detwinning occurs in G_9 and G_{10} during the entire loading cycle due to the small SF values.

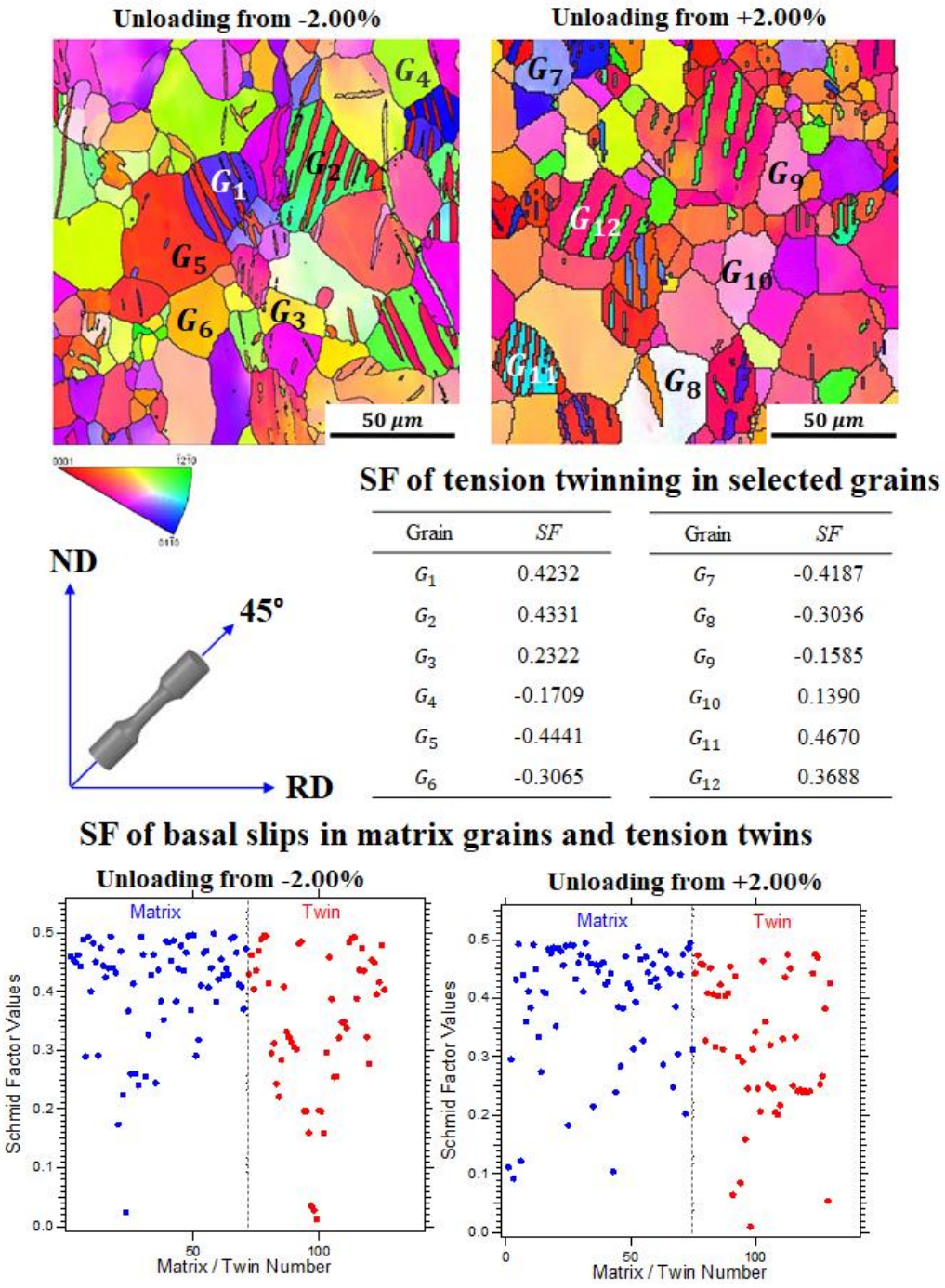

Grain	*SF*	Grain	*SF*
G_1	0.4232	G_7	-0.4187
G_2	0.4331	G_8	-0.3036
G_3	0.2322	G_9	-0.1585
G_4	-0.1709	G_{10}	0.1390
G_5	-0.4441	G_{11}	0.4670
G_6	-0.3065	G_{12}	0.3688

Fig. 5.14: EBSD IPF maps, maximum SFs of tension twinning in representative grains, and SF distributions of basal slips in matrix grains / tension twins for the $\theta = 45^{o}$ specimen after loaded at a strain amplitude of 2.0% for 40 cycles.

To summarize, there are several major differences in terms of twinning and detwinning between the θ = 45º specimens and the specimens of other material orientations. Due to smaller SF, twinning is more difficult to occur in the θ = 45º specimens than the specimens of other material orientations. For the material orientation other than θ = 45º, twinning occurs in the grains with orientations favorable for twinning during a loading reversal and detwinning occurs in the same group of grains during the reversed loading reversal. With the θ = 45º material orientation, twinning and detwinning occur simultaneously under both tension and compression. Twinning occurs in a group of grains oriented favorably for twinning under tension (such as G_5, G_6, G_{11} and G_{12} in Fig. 5.14) and simultaneously, detwinning occurs in a second group of grains oriented favorably for twinning under compression (such as G_1, G_2, G_7, and G_8 in Fig. 5.14). During the compression loading reversal, twinning occurs in the second group of grains and concurrently, detwinning occurs in the first group of grains. Therefore, both twinning and detwinning occur during both tension and compression loading reversals. The TVF measured for the microstructure unloading from -2.00% and 2.00% is 7.77% and 7.35%, respectively. This observation indicates that the twinning-detwinning activity is approximately identical during the tension and compression reversals for θ = 45º material orientation.

In Fig. 5.14, the SF distributions of basal slip in matrix grains and $\{10\bar{1}2\}$ tension twins are plotted for the microstructure unloading from -2.00% and 2.00%. It can be observed that the SF of basal slip tension twins exhibits a similar distribution with that in the matrix grains. The results in Fig. 5.14 indicate that for θ = 45º, the texture with tension twins can exhibit the same basal slip activation behavior with the initial texture without tension twins,

As a consequence, the compression and tension loading reversals exhibit almost identical mechanical response during cyclic loading, which results in the observed symmetric stress-strain hysteresis loops (Fig. 5.2c), and identical elastic limit range values for the lower and upper branch (Fig. 5.10c and Fig. 5.12c), irrespective of the number of loading cycles and applied strain amplitude.

Another uniqueness of the θ = 45º orientation is the less percentage of grains being twinned and detwinned during the fully reserved strain-controlled tension-compression. At a strain amplitude of 2.00% after 40 loading cycles, based on the statistics of 70 grains in the observation area shown in Fig. 5.14, approximately 30% of the total grains experience twinning, 30% of the total grains undergo detwinning, and the rest grains experience no twinning or detwinning. In contrast, for the ND specimen, approximately 90% of the grains undergo twinning at a strain of 2.0% under tension and the same group of grains experience detwinning during compression.

5.4 Summary

The plastic deformation characteristics was analyzed for a rolled AZ31B magnesium alloy under uniaxial cyclic loading along five different orientations with respect to the rolled direction (RD): 0º (RD), 22.5º, 45º, 67.5º, 90º (ND). The following conclusions can be drawn from the study,

1) The stress-strain hysteresis loop is symmetric when strain amplitude is lower than the lower kink point. When the strain amplitude is in between the upper and lower kink points, the asymmetric stress-strain hysteresis loop contains one inflection point which signifies completion of detwinning and start of non-basal slips. When the strain

amplitude is higher than the upper kink point, the stress-strain hysteresis loop tends to be symmetric with both upper and lower branches having a sigmodal shape.

2) Cyclic hardening is proportional to the loading amplitude and is observed for all the five material orientations when the strain amplitude is higher than the lower kink point. Positive mean stresses are shown in the $\theta < 45^{o}$ material orientations and compressive mean stresses are found in the $\theta > 45^{o}$ material orientations. The $\theta = 45^{o}$ material orientation has virtually zero mean stresses.
3) The elastic limit range represents the activation stress for basal dislocation slips or twining/detwinning, which is intrinsically depending on the microstructure at the peak stress prior to the loading reversal.
4) On the compression reversals for $\theta < 45^{o}$ and tension reversals for $\theta > 45^{o}$, the elastic limit range is independent of the number of loading cycles and the applied strain amplitude, which signifies the activation stress for basal slips during the cyclic loading.
5) On the tension reversals for $\theta < 45^{o}$ and compression reversals for $\theta > 45^{o}$, the elastic limit range is dependent on the number of loading cycles and the applied strain amplitude. The elastic limit range values reflect the activation stress for basal slip or twinning/detwinning, which is depending on the twin volume fraction at the peak stress prior to the loading reversal.
6) At the material orientation $\theta = 45^{o}$, twinning occurs in one group of grains and simultaneously detwinning occurs in another group of grains during loading and during reversed loading. The Schmid factor for twinning is statistically low in the 45^{o} orientation specimens, thus low percentage of grains favorable for twinning, as compared with the other material orientations. The values of elastic limit ranges

indicating the activation stress of basal slips are approximately identical on the tension reversals and compression reversals, irrespective of the number of loading cycles and the applied strain amplitude.

7) The elastic limit range during cyclic loading also demonstrates a strong material orientation dependence, with its highest value at $\theta = 0^{o}$ and lowest value at $\theta = 45^{o}$. The $\theta = 45^{o}$ orientation exhibits the highest inflection strain ranges.

6 Anisotropic Fatigue Behavior

6.1 Fatigue Results and Kink Points

Fully reversed strain-controlled tension-compression fatigue experiments in the five material orientations are summarized in Tables 4-8. The stress amplitudes and the mean stresses were taken at approximate half fatigue lives. The plastic strain energy density per loading cycle, ΔW^p, was calculated from the stress-strain hysteresis loop at approximate half fatigue life.

Table 4 Fatigue experiments of 0º (RD) specimens under fully reversed strain-controlled tension-compression loading.

Spec ID	f (Hz)	$\Delta\varepsilon/2$ (%)	σ_m (MPa)	$\Delta\sigma/2$ (MPa)	ΔW^p (MJ/m^3)	N_f (cycles)
3R0COM2	0.03	6.00	-39.7	309.8	39.498	1
3R0SII05	0.05	4.00	61.5	286.7	21.361	5.5
3R0SII06	0.08	3.00	27.7	239.5	13.709	48
3R0SII07	0.1	2.50	31.4	219.5	10.223	78
3R0SII01	0.1	2.00	42.7	209.7	6.867	180
3R31B0SS08	0.2	1.40	50.4	195.8	3.833	280
3R31B0SS03	0.2/0.3/0.2	1.00	54.3	185.1	2.011	455
3R31B0S24	0.2	1.00	62.0	193.8	1.938	460
3R31B0S13	0.25	0.75	54.6	178.1	1.047	880
3R31B0SS07	0.4	0.60	52.4	172.6	0.654	980
3R31B0S21	0.5	0.48	50.0	167.8	0.260	2,020
3R31B0SS09	1	0.42	42.2	149.9	0.177	2,340
3R31B0S32	1	0.40	30.5	138.6	0.172	4,900
3R31B0SS05	1.5/1.5	0.35	27.3	130.4	0.109	5,388
3R31B0SS06	1.5/1.5	0.35	24.9	128.6	0.119	5,800
3R31B0SS10	2	0.32	21.4	121.8	0.084	9,450
3R31B0S34	2.5	0.30	15.8	114.5	0.073	16,400
3R31B0SS11	3	0.28	10.7	109.7	0.060	17,600
3R31B0S31	1/4/5	0.27	7.0	107.1	0.052	44,300
3R31B0SS04	2/4	0.25	6.0	101.0	0.045	38,800
3R31B0S23	1/5	0.25	3.1	98.4	0.045	47,200
3R0SII03	2/10	0.22	4.1	91.1	0.024	78,032
3R31B0S12	2/8/10	0.22	-1.5	91.9	0.018	226,000
3R31B0S22	2/7.5/10	0.20	0.0	86.0	0.003	>769,000
3R0SII04	2/10/2/10	0.19	-4.5	82.5	0.002	>800,555

Note: f-frequency; $\Delta\varepsilon/2$-strain amplitude; σ_m-mean stress; $\Delta\sigma/2$-stress amplitude; ΔW^p-plastic strain energy density per loading cycle; N_f-number of loading cycles to failure.

Table 5 Fatigue experiments of 22.5º specimens under fully reversed strain-controlled tension-compression loading.

Spec ID	f (Hz)	$\Delta\varepsilon/2$ (%)	σ_m (MPa)	$\Delta\sigma/2$ (MPa)	ΔW^p (MJ/m^3)	N_f (cycles)
3R22COM2	0.03	6.00	-3.8	259.1	28.595	1.5
3R22SII12	0.05	4.00	28.2	237.0	20.488	8
3R22SII13	0.08	3.00	21.2	207.2	12.962	36
3R22SII14	0.1	2.50	22.8	177.7	9.386	48
3R22SII08	0.1	2.00	20.8	171.6	6.650	120
3R31B22S3-10	0.25	1.50	24.8	152.1	3.966	140
3R22SII01	0.2	1.00	17.0	135.0	2.050	332
3R31B22S2-3	0.25	1.00	23.5	139.8	1.970	410
3R22SII05	0.3	0.75	19.3	122.9	1.120	734
3R31B22S2-10	0.3	0.75	22.1	127.6	1.118	827
3R31B22S3-9	1/1	0.60	18.2	119.6	0.716	1,440
3R31B22S4-1	0.6	0.55	17.4	116.3	0.588	1,649
3R22SII03	0.5	0.50	9.2	104.6	0.493	2,619
3R31B22S2-4	0.75	0.50	10.5	107.2	0.473	3,100
3R31B22S3-3	1.25	0.40	5.2	96.9	0.309	5,100
3R22SII06	1.25/1.5	0.40	7.4	95.1	0.313	6,100
3R22SII04	2	0.30	0.2	86.3	0.173	12,080
3R31B22S2-8	3	0.30	-0.4	87.3	0.174	16,400
3R22SII07	4/2	0.25	-1.0	78.0	0.110	16,547
3R31B22S3-2	3	0.25	-0.9	82.7	0.106	54,844
3R31B22S2-9	4	0.22	-1.4	77.6	0.072	66,333
3R31B22S3-8	5	0.21	-1.1	76.9	0.055	127,000
3R22SII02	2/4	0.20	-3.2	71.8	0.050	34,453
3R22SII10	2/10	0.20	-6.0	73.6	0.049	52,000
3R31B22S2-7	2/4/8	0.20	2.1	79.6	0.027	637,500
3R31B22S3-7	2/4/6/10	0.19	0.9	75.6	0.024	564,600
3R31B22S3-4	2/5	0.18	-1.8	71.1	0.028	168,780
3R31B22S3-6	2/5/10	0.17	0.76	71.5	0.008	>1,037,000
3R31B22S3-5	2/5/5/10	0.16	-3.8	67.9	0.004	>1,112,820
3R22SII11	2/10	0.15	-3.0	61.0	0.009	77,000
3R31B22S2-5	2/5/8/2/8	0.15	-0.7	64.4	0.003	>1,000,000
3R22SII09	2/8/2/8	0.13	-9.6	56.0	0.001	395,136

Note: f-frequency; $\Delta\varepsilon/2$-strain amplitude; σ_m-mean stress; $\Delta\sigma/2$-stress amplitude; ΔW^p-plastic strain energy density per loading cycle; N_f-number of loading cycles to failure.

Table 6 Fatigue experiments of 45º specimens under fully reversed strain-controlled tension-compression loading.

Spec ID	f (Hz)	$\Delta\varepsilon/2$ (%)	σ_m (MPa)	$\Delta\sigma/2$ (MPa)	ΔW^p (MJ/m^3)	N_f (cycles)
3R45COM2	0.03	6.00	17.4	221.3	33.645	2.25
3R45SII12	0.05	4.00	3.2	180.0	17.550	12
3R45SII13	0.08	3.00	2.7	157.3	11.080	37
3R45SII09	0.1	2.00	2.1	127.7	5.635	80
3R45SII14	0.18	1.50	0.4	116.3	3.406	260
3R31B45S10	2/0.2	1.00	-1.1	104.4	1.699	560
3R45SII01	0.2	1.00	0.7	102.9	1.654	660
3R45SII07	0.3	0.75	1.2	91.8	0.989	1,060
3R31B45S09	2/0.3	0.75	-1.2	95.4	0.972	1,520
3R31B45S13	0.5	0.60	-1.0	89.5	0.667	2,140
3R31B45S07	2/0.7	0.50	-0.4	81.7	0.483	3,220
3R45SII02	0.5	0.50	-0.6	77.4	0.476	3,916
3R31B45S04	2/1	0.40	-1.0	76.1	0.340	5,820
3R45SII08	1	0.40	0.8	72.8	0.324	7,476
3R45SII03	1/2.5	0.30	1.7	67.7	0.206	11,650
3R31B45S05	2/2	0.30	-0.6	72.1	0.206	18,750
3R31B45S14	2	0.25	-6.2	68.3	0.140	44,650
3R31B45S16	3/4	0.22	-1.0	68.1	0.100	76,500
3R45SII04	2/4	0.20	1.6	61.2	0.077	24,500
3R31B45S06	2/2/4	0.20	-1.4	64.9	0.077	42,520
3R31B45S12	2/2/8	0.17	-0.7	61.9	0.040	110,900
3R45SII10	2/10	0.15	-2.1	57.0	0.026	93,272
3R45SII05	2/6	0.13	-0.8	50.8	0.010	98,024
3R45SII11	2/10	0.12	-1.9	49.6	0.003	133,000
3R45SII06	2/8/2	0.11	-2.5	47.6	0.001	>1,200,000

Note: f-frequency; $\Delta\varepsilon/2$-strain amplitude; σ_m-mean stress; $\Delta\sigma/2$-stress amplitude; ΔW^p-plastic strain energy density per loading cycle; N_f-number of loading cycles to failure.

Table 7 Fatigue experiments of 67.5º specimens under fully reversed strain-controlled tension-compression loading.

Spec ID	f (Hz)	$\Delta\varepsilon/2$ (%)	σ_m (MPa)	$\Delta\sigma/2$ (MPa)	ΔW^p (MJ/m^3)	N_f (cycles)
3R67COM5	0.03	6.00	-37.0	233.9	19.184	0.5
3R67COM3	0.05	4.00	-35.8	218.9	17.560	4
3R67SII07	0.08	3.00	-34.6	190.6	10.997	6.5
3R67SII03	0.1	2.00	-34.2	167.7	6.084	52
3R67SII08	0.18	1.50	-28.3	141.1	3.574	135
3R31B67S23	0.2	1.20	-23.8	133.9	2.619	300
3R67SII02	0.2	1.00	-23.1	121.5	1.797	260
3R31B67S21	0.25	1.00	-17.1	119.4	1.649	560
3R67SII05	0.3	0.75	-19.6	111.0	1.055	450
3R31B67S22	0.4	0.75	-21.1	118.7	1.125	780
3R31B67S08	0.5	0.60	-15.2	105.3	0.706	960
3R31B67S05	0.7	0.50	-12.6	99.6	0.513	1,420
3R67SII04	0.5	0.50	-11.8	97.8	0.486	2,100
3R31B67S16	1	0.45	-9.5	94.4	0.416	1,520
3R31B67S24	1	0.42	-7.3	92.8	0.363	5,040
3R67SII01	1	0.40	-9.0	89.8	0.317	3,700
3R31B67S17	1	0.40	-5.7	90.1	0.329	4,520
3R31B67S07	1.5	0.35	-3.8	84.0	0.260	4,280
3R31B67S04	2.5	0.30	-1.7	79.9	0.192	9,200
3R31B67S06	3	0.25	-2.3	75.4	0.126	15,320
3R31B67S13	4	0.20	-1.1	71.0	0.070	32,600
3R67SII06	2/4	0.20	-1.1	70.7	0.068	64,400
3R31B67S09	2/6	0.17	-0.6	67.1	0.036	66,950
3R31B67S14	2/5/5	0.16	-1.6	66.1	0.023	175,200
3R31B67S03	2/8/8/8	0.15	-2.8	65.6	0.010	604,100
3R31B67S15	5	0.145	-1.7	61.7	0.011	177,000
3R31B67S18	5/10	0.145	-2.1	61.8	0.011	190,000
3R31B67S19	5/10	0.135	-0.4	58.4	0.009	89,914
3R31B67S20	2/10	0.13	-2.2	58.9	0.005	>1,370,411

Note: f-frequency; $\Delta\varepsilon/2$-strain amplitude; σ_m-mean stress; $\Delta\sigma/2$-stress amplitude; ΔW^p-plastic strain energy density per loading cycle; N_f-number of loading cycles to failure.

Table 8 Fatigue experiments of 90º(ND) specimens under fully reversed strain-controlled tension-compression loading.

Spec ID	f (Hz)	$\Delta\varepsilon/2$ (%)	σ_m (MPa)	$\Delta\sigma/2$ (MPa)	ΔW^p (MJ/m^3)	N_f (cycles)
3R90COM3	0.03	6.00	-96.0	292.4	22.890	0.75
3R90COM2	0.05	4.00	-46.1	278.0	20.678	3
3R90SII04	0.08	3.00	-55.4	251.1	12.443	13
3R90SII07	0.1	2.00	-59.3	204.2	6.031	45
3R90SII01	0.1	2.00	-58.0	211.7	6.204	70
3R90SII06	0.18	1.50	-62.1	184.8	3.730	60
3R31B90SS17	0.2	1.00	-54.4	163.8	1.913	140
3R31B90S03	0.2	1.00	-55.2	162.8	1.865	180
3R31B90S06	0.25	0.75	-48.0	149.4	1.134	280
3R31B90S04	0.5	0.50	-37.0	132.3	0.469	820
3R31B90S12	1	0.40	-27.0	119.7	0.269	2,300
3R31B90SS20	1.5	0.36	-22.7	111.8	0.208	4,195
3R31B90S02	1/2.5	0.30	-13.8	98.5	0.145	5,250
3R31B90SS19	2.5	0.25	-23.6	75.6	0.062	10,852
3R31B90S08	1/4	0.25	-3.5	91.0	0.093	12,600
3R90SII03	4	0.20	-3.5	81.5	0.044	39,000
3R31B90S14	2/7.5	0.20	-4.3	82.6	0.039	40,560
3R31B90S01	2/8	0.17	-3.0	75.2	0.017	80,200
3R31B90S10	2/10	0.15	-2.9	67.5	0.006	161,920
3R31B90SS18	2/8	0.14	4.0	65.6	0.005	108,180
3R31B90S13	2/10/10	0.13	1.3	58.4	0.005	218,000
3R31B90S09	2/15/15	0.12	-1.1	55.4	0.002	>967,600

Note: f-frequency; $\Delta\varepsilon/2$-strain amplitude; σ_m-mean stress; $\Delta\sigma/2$-stress amplitude; ΔW^p-plastic strain energy density per loading cycle; N_f-number of loading cycles to failure.

The strain-life fatigue curves are shown in Fig. 6.1. An arrow after a data point denotes an experiment without fatigue failure after more than 10^6 loading cycles. The stress-life fatigue curves of the five material orientations are shown in Fig. 6.2.

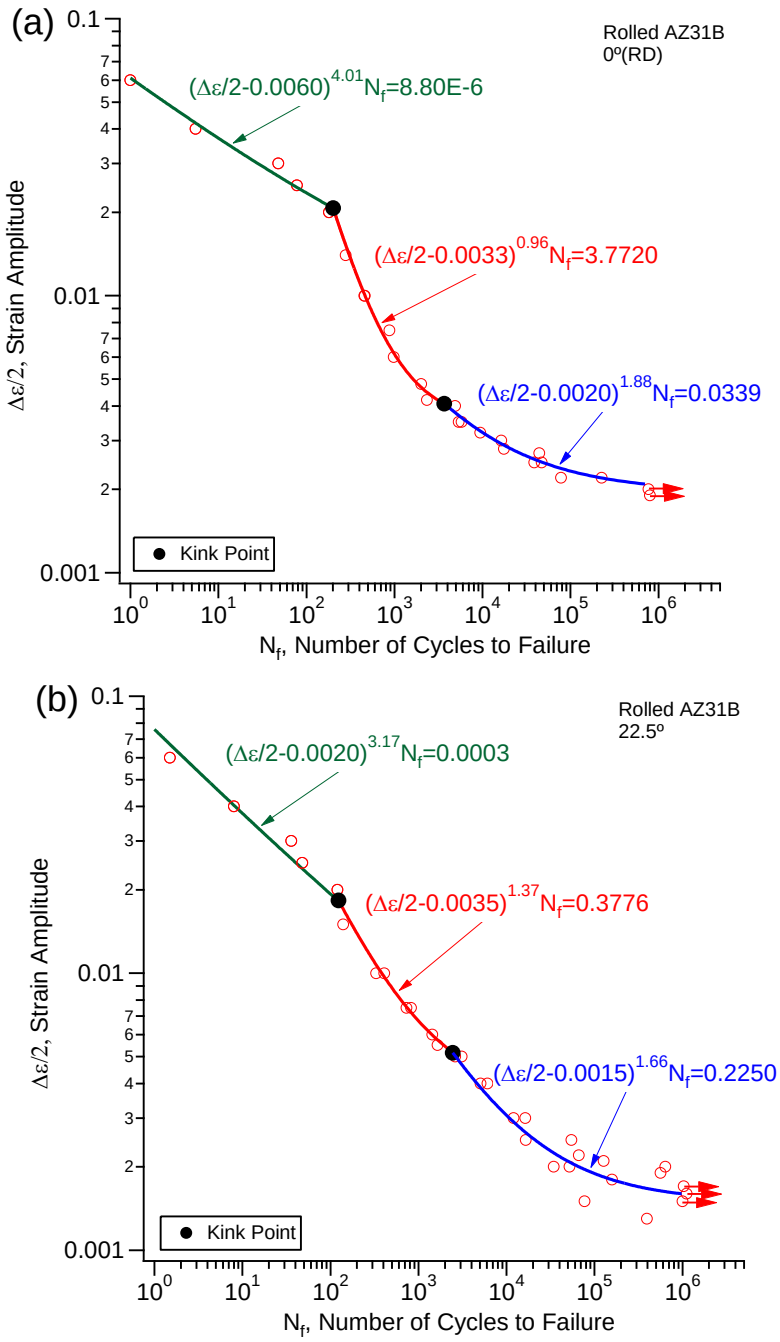
(a)
Rolled AZ31B
0º(RD)
(Δε/2-0.0060)^4.01 Nf=8.80E-6
(Δε/2-0.0033)^0.96 Nf=3.7720
(Δε/2-0.0020)^1.88 Nf=0.0339
Kink Point
Δε/2, Strain Amplitude
Nf, Number of Cycles to Failure
(b)
Rolled AZ31B
22.5º
(Δε/2-0.0020)^3.17 Nf=0.0003
(Δε/2-0.0035)^1.37 Nf=0.3776
(Δε/2-0.0015)^1.66 Nf=0.2250
Kink Point
Δε/2, Strain Amplitude
Nf, Number of Cycles to Failure

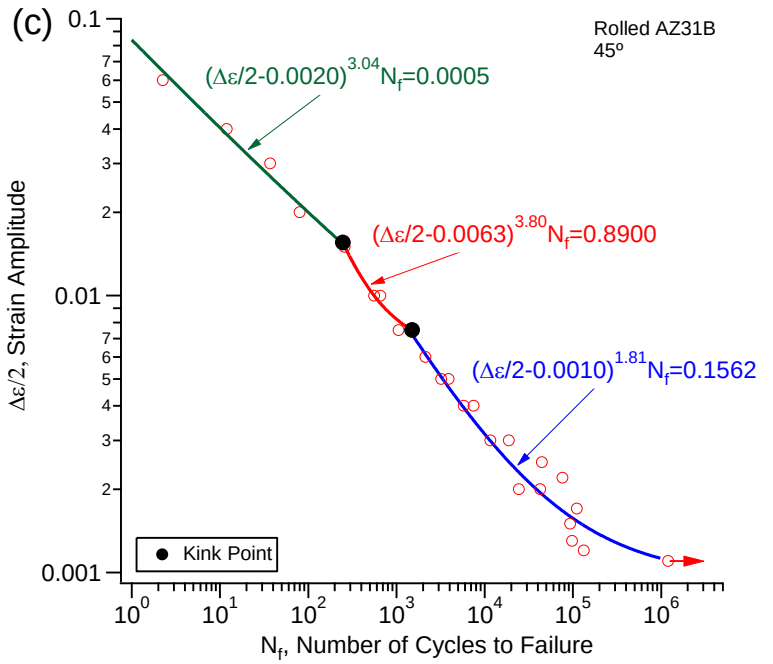
(c)
Rolled AZ31B
45º
(Δε/2-0.0020)^3.04 Nf=0.0005
(Δε/2-0.0063)^3.80 Nf=0.8900
(Δε/2-0.0010)^1.81 Nf=0.1562
Kink Point
Δε/2, Strain Amplitude
Nf, Number of Cycles to Failure

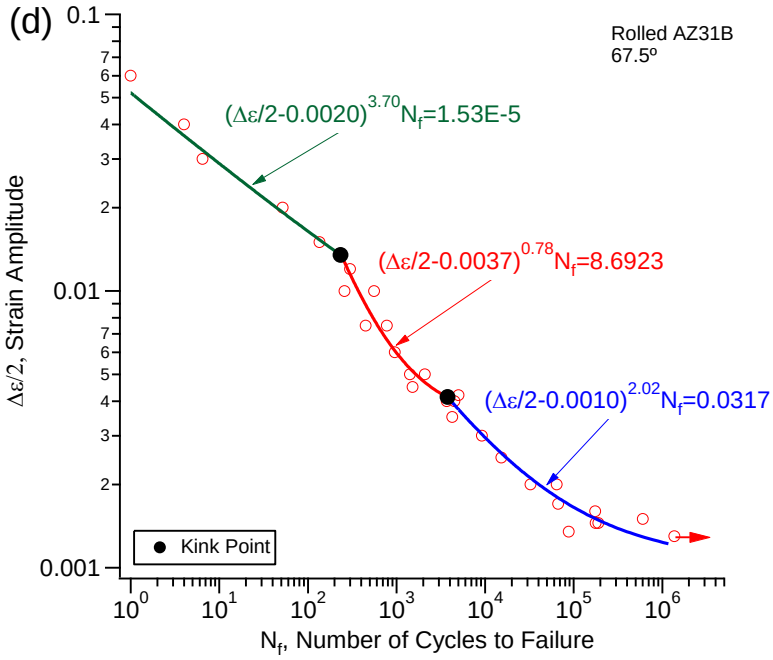
(d)
Rolled AZ31B
67.5º
(Δε/2-0.0020)^3.70 Nf=1.53E-5
(Δε/2-0.0037)^0.78 Nf=8.6923
(Δε/2-0.0010)^2.02 Nf=0.0317
Kink Point
Δε/2, Strain Amplitude
Nf, Number of Cycles to Failure

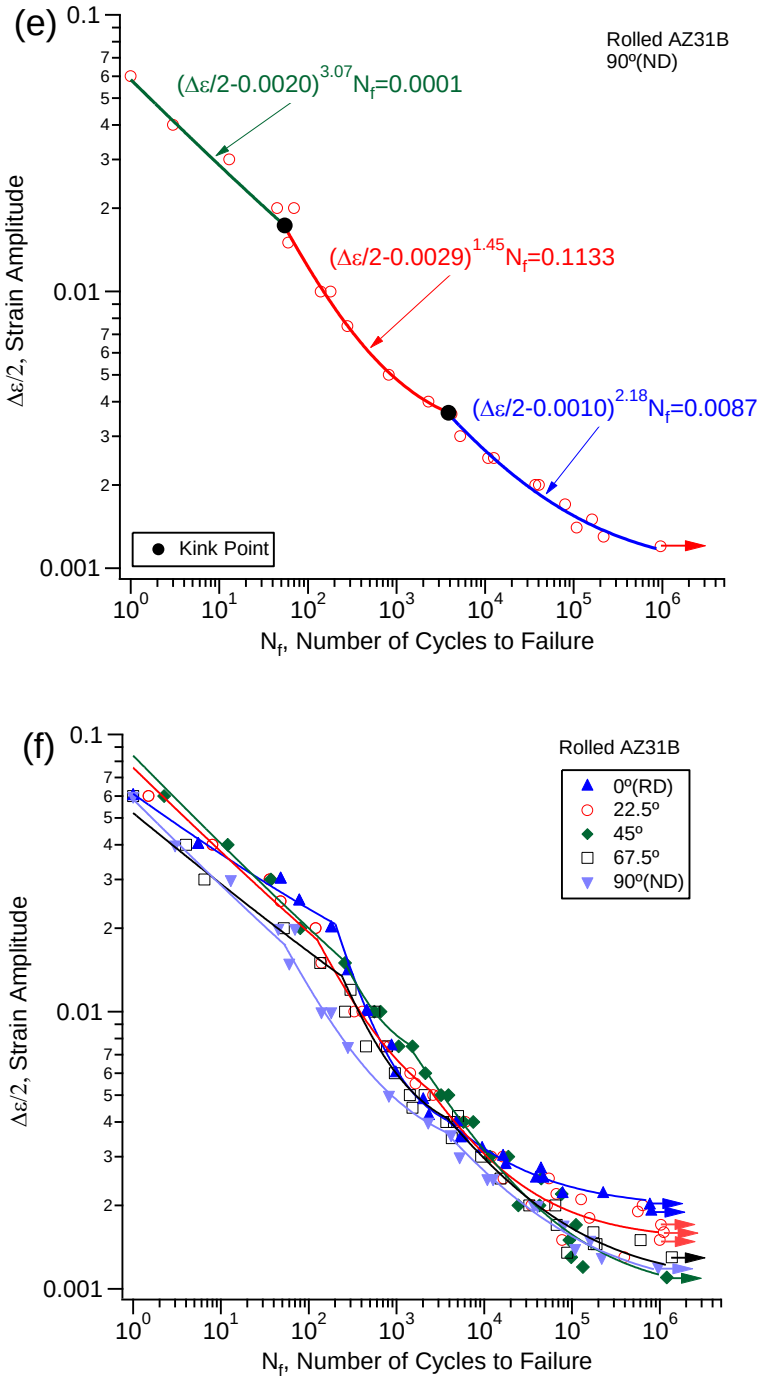

Fig. 6.1: Strain-life curves under fully reversed strain-controlled tension-compression for rolled AZ31B alloy: (a) 0º (RD), (b) 22.5º, (c) 45º, (d) 67.5º, (e) 90º (ND), and (f) all orientations.

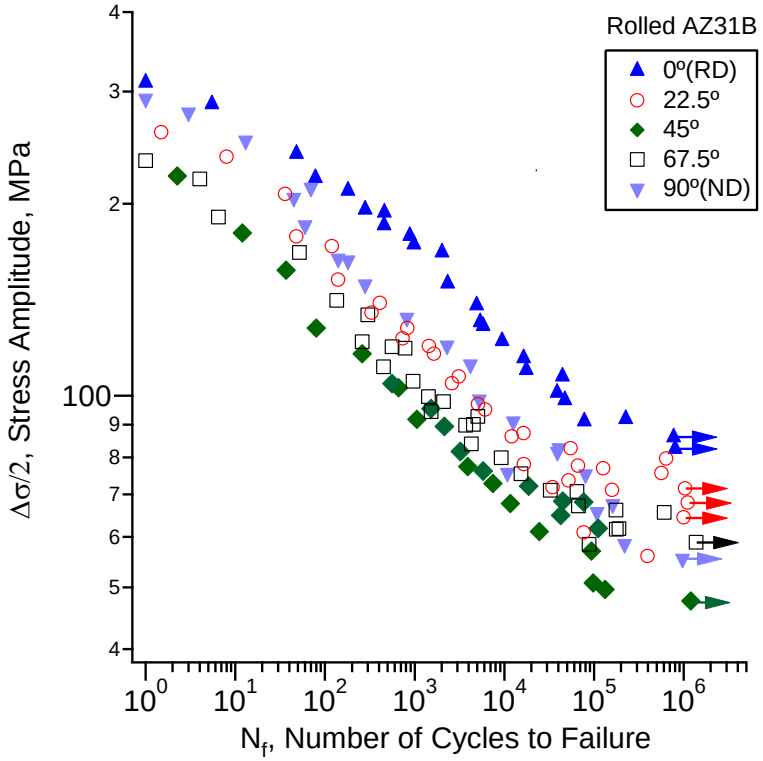

Fig. 6.2: Stress-life curves for rolled AZ31B magnesium alloy.

The strain-life fatigue curves of most metallic materials under fully reversed strain-controlled tension-compression loading can be described by the following three-parameter equation,

$$(\frac{\Delta\varepsilon}{2} - \varepsilon_0)^{\xi} N_f = C \tag{3}$$

where $\Delta\varepsilon/2$ is the strain amplitude, N_f is the number of loading cycles to failure, and ε_0, ξ, and C are the constants determined by fitting the experimental data. There are two kink points in each strain-life curve for a Mg alloy. As a result, three equations are needed to describe the whole strain-life curve with fatigue life ranging from a few loading cycles to over a million loading cycles. In Fig. 6.1, the kink points are denoted by black solid circles. The stress amplitudes, strain amplitudes, and fatigue lives corresponding to the kink points of all the five material orientations are summarized in Table 9.

Table 9 Kink points for different material orientations.

Material Orientation, °	Lower Kink Point			Upper Kink Point		
	$\Delta\varepsilon/2$, %	$\Delta\sigma/2$, MPa	N_f, cycles	$\Delta\varepsilon/2$, %	$\Delta\sigma/2$, MPa	N_f, cycles
0 (RD)	0.41	144	3,680	2.07	211	200
22.5	0.52	111	2,460	1.83	165	120
45	0.75	95	1,500	1.56	118	250
67.5	0.41	92	3,770	1.35	138	230
90 (ND)	0.37	112	3,870	1.73	197	50

Note: $\Delta\varepsilon/2$-strain amplitude; $\Delta\sigma/2$-stress amplitude; N_f-number of loading cycles to failure.

The kink points in a strain-life curve reflect the demarcation of dominating cyclic plastic deformation mechanisms. Earlier investigations on extruded Mg alloys tested in the extrusion direction reveal that kink points exist in the strain-life curves that demarcate the influence of twinning-detwinning deformation on fatigue [50,117,118]. The current study further suggests that two kink points exist in the strain-life fatigue curve of any given material orientation. Consistent with the previous observations, the lower kink point signifies the involvement of persistent twinning-detwinning deformation during fatigue loading. It can be noted in table 9 that the strain amplitude corresponding to the lower kink point in the strain-life curve for the θ = 45º is the highest among all material orientation. This observation is due to that with smaller SF, twinning is more difficult to occur in the θ = 45º specimens than the specimens of other material orientations.

When all the strain-life curves of the five material orientations are plotted together (Fig. 6.1f), the features with the kink points are lost but the presentation leads to an overall observation: all the strain-life curves fall in a relatively narrow band. The anisotropic fatigue properties are better reflected in the stress-life curves shown in Fig. 6.2. A glance of the results reveals that the RD material orientation has the highest stress-life curve and the 45º orientation has the lowest, with the results of the other three material orientations

falling in between. Both the stress-life curves and the strain-life curves show that the fatigue lives in the RD are longer than those in the ND at a given strain amplitude or stress amplitude. The fatigue results in the RD and ND in the current work are consistent with these reported earlier on a similar material [54,59]. However, a different tendency was reported by other researchers [48,64] on a similar rolled Mg alloy.

6.2 Fatigue damage: Influence of strain amplitude and material orientation

For all the specimens with different material orientations, fatigue cracks were initiated from the outer specimen surface, and the process was followed by crack propagation into the interior of the specimen till total fracture. As shown in Fig. 6.3, the three-dimensional schematics of fracture surfaces are inserted in the strain-life curves, under strain amplitudes taken from the three regimes divided by the two kink points. It can be seen from Fig. 6.3 that the overall fatigue cracking behavior is related to the upper kink point for all the five material orientations.

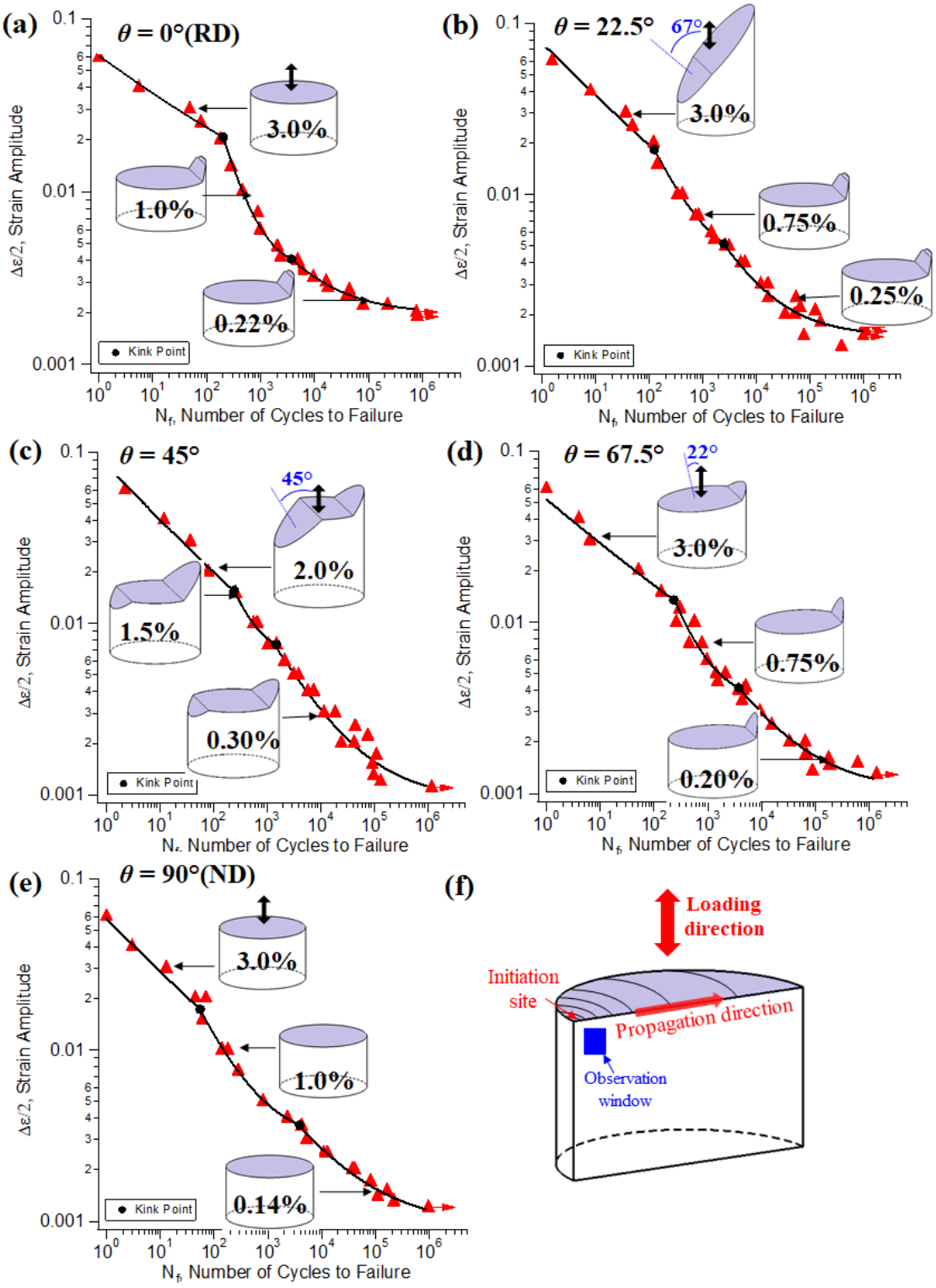

Fig. 6.3: Three-dimensional illustrations of the fracture profiles corresponding to selected strain amplitudes in strain-life curves: (a) θ = 0º (RD), (b) θ = 22.5º, (c) θ = 45º, (d) θ =

67.5º, (e) θ = 90º (ND), and (f) The sample was cut along the diametric direction, approximately following the propagation direction. The observation window is captured near the specimen surface, below the initiation site.

The microcracks in the local area near the initiation site are characterized by SEM and EBSD scanning to investigate the crack initiation mechanism as well as the early-stage crack growth mode. The samples for EBSD analysis were cut along the diametrical direction, approximately following the propagation direction. The observation window for microcracks is located near the specimen surface, below the fatigue crack initiation site, as indicated in Fig. 6.3f.

6.2.1 Fatigue damage at θ = 0º (RD)

Fig. 6.4 shows the low-magnification optical microscopy images for the side view of the fracture surface at the strain amplitudes of 3.0%, 1.0% and 0.22%. The macroscopic fracture surfaces for θ = 0º (RD) exhibit brittle-like features with early propagation surface perpendicular to the loading direction, regardless of the loading magnitude. Irregular-shaped ridge features are observed on the fracture surface. When the strain amplitude is 1.0%, multiple fatigue cracks can be observed on the specimen surface, as seen in Fig. 6.4b.

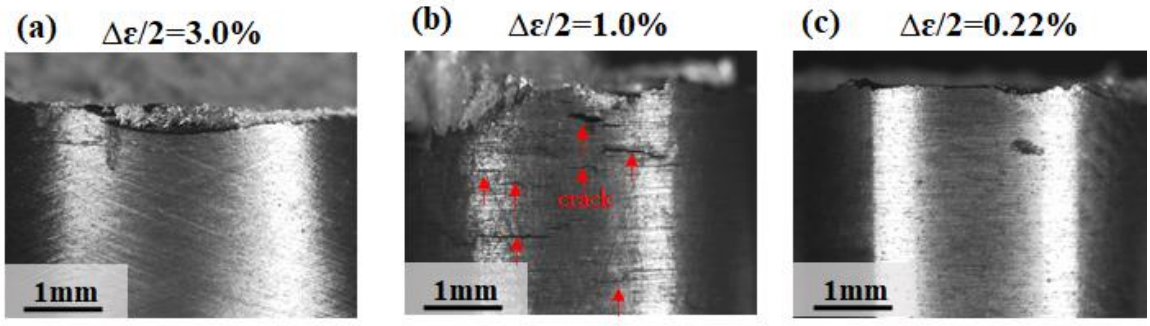

Fig. 6.4: Optical microscopy images for the side view of the fracture surface at the strain amplitude of (a) 3.0%, (b) 1.0% and (c) 0.22% for θ = 0º (RD). Red arrows show the fatigue cracks on the specimen surface.

Fig. 6.5 presents the SEM and EBSD characterization for the microcracks at the strain amplitude of 3.0% for θ = 0º (RD) after fatigue experiment. In Fig. 6.5a, the location of the fatigue crack initiation is indicated in the side view of the fracture surface. Figs. 6.5b-c present two microcracks located near the specimen surface, of which are sized 7 μm and 12 μm, respectively. EBSD characterization of the microstructure surrounding the microcrack reveals that both intergranular cracking (Fig. 6.5b) and transgranular cracking (Fig. 6.5c) can be detected in the local area near the initiation site. From Fig. 6.5b, the microcrack is developed at the GB between grain G1 and grain G2, where a triple joint met by grains G1, G2, and G3 is adjoined. The misorientation angles between the neighboring grains are 25º, 37º, and 17º for G1-G2 pair, G2-G3 pair, G3-G1 pair, respectively. This observation indicates that the GB cracking is favorable to be initiated from the high angle grain boundaries (HAGBs). In grain G4 as shown in Fig. 6.5c, the microcrack shows the same alignment with the trace of $(\bar{2}112)$ pyramidal <c+a> plane, as well as the trace of $(01\bar{1}2)$ tension twinning plane which is corresponding to the T2 variant. Interestingly, the T2 tension twin variant is observed in G4 with its tip connected to the microcrack.

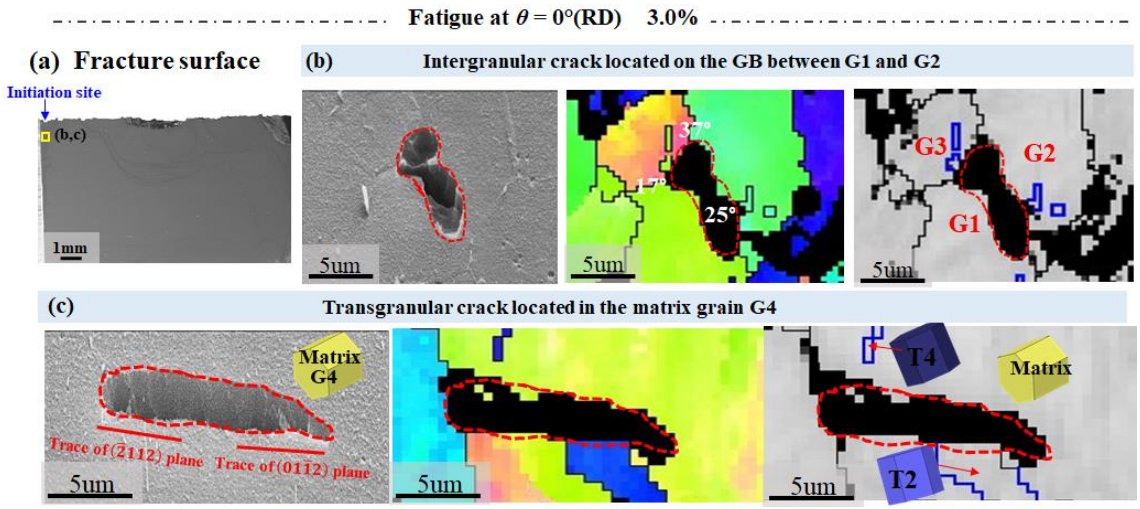

Fig. 6.5: Microcracks observed for the 0º (RD) specimen after fatigue experiment at the strain amplitude of 3.0%: (a) Side view of the fracture surface, (b) SEM image, IPF and IQ map for the intergranular crack located on the GB between G1 and G2, (c) SEM image, IPF and IQ map for the transgranular crack located in the matrix grain G4. In the IQ map, grain boundaries are denoted by black lines. Tension twin boundaries are colored in blue.

The fracture surface for θ = 0º (RD) specimen after fatigue experiment at the strain amplitude of 3.0% is examined by the SEM and shown in Fig. 6.6. The overview of the fracture surface is shown in Fig. 6.6a. The dash lines in Fig. 6.6a divide the fracture surface into zone I and zone II, which denotes the crack initiation region and early-stage propagation region, respectively. The high-resolution image for zone I is shown in Fig. 6.6b, it can be observed that multiple parallel traces spreading all over this region. The traces in the same arraying direction gathered within different individual small areas, of which the size is also in accordance with the average grain size. Therefore, the borders of the areas containing the same parallel traces can be presumably considered to be related to the GBs. Accordingly, the formation of the traces can be attributed to the cyclic deformation within the grains.

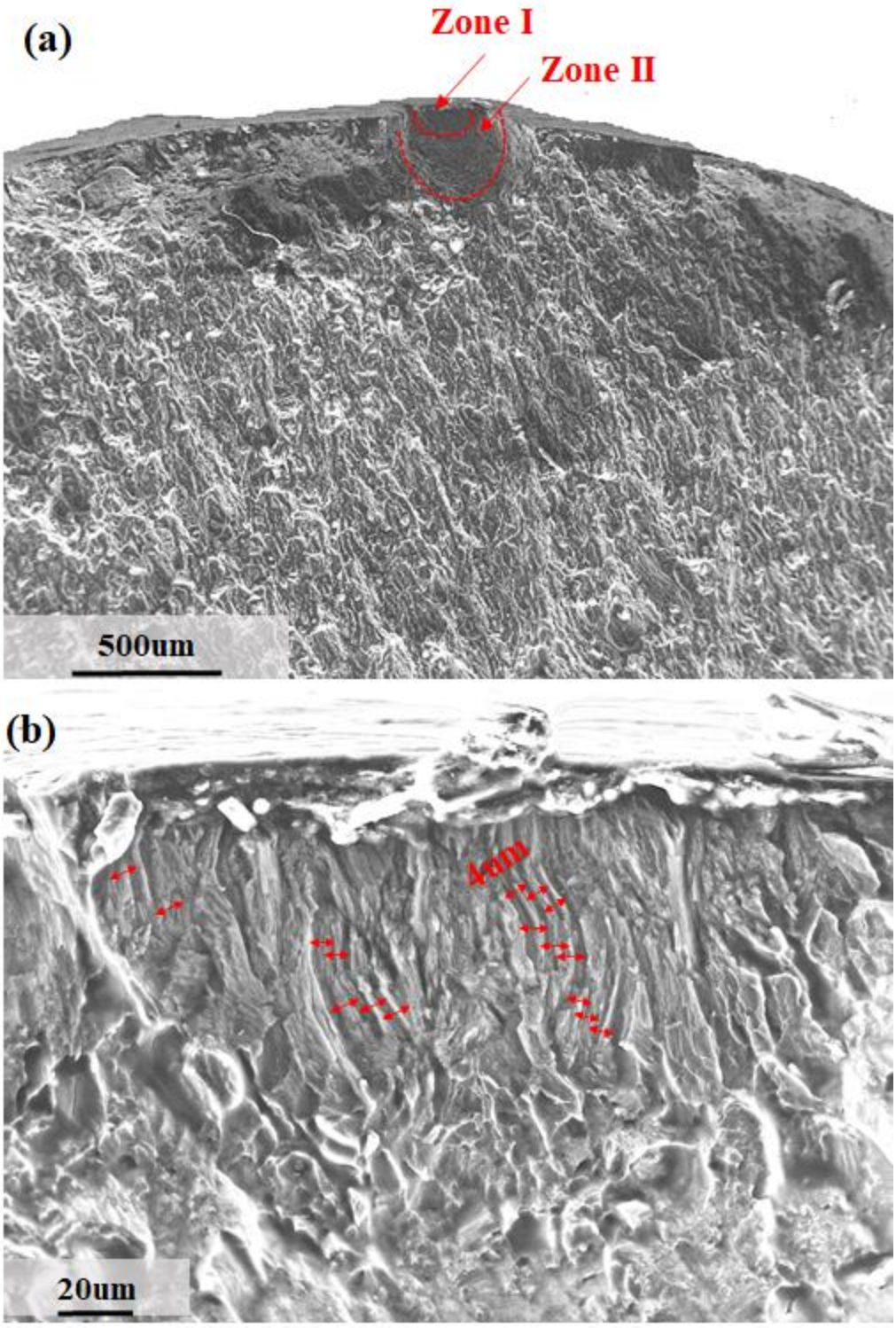

Fig. 6.6: SEM images showing the fracture surface for the 0º (RD) specimen after fatigue experiment at the strain amplitude of 3.0%: (a) Overview of the fatigue crack initiation

region (zone I) and early-stage propagation region (zone II) at the fracture surface and (b) High resolution image for the traces observed in Zone I. The traces are denoted by red double end arrows.

At the strain amplitude of 1.0%, the microcracks after fatigue experiment are presented in Fig. 6.7. As seen from the side view of the fracture surface in Fig. 6.7a, the regions of initiation site and early-stage propagation are perpendicular to the loading direction. At the local region near the initiation site, both intergranular and transgranular cracking can be detected. Fig. 6.7b shows a short microcrack sized approximately 5 μm located on the GB between grain G1 and grain G2, with a misorienation angle of 38º. The fatigue damage site is found to be on the GB attached by a tension twin tip. Our observation in Fig. 6.7b indicates that fatigue crack initiation for fatigue at θ = 0º (RD) might originate from the HAGBs. We further elucidate the early-stage propagation behavior by examining a longer crack sized approximately 20 μm, as shown in Fig. 6.7c. The microcrack penetrates the large matrix grain (G3) and shows good alignment with the trace of basal slip plane. The lower tip of the microcrack is located on the GB between grain G4 and G5, with a misorientation angle of 67º. The results in Fig. 7.3 indicate that the early-stage crack growth is proceed by alternative routes via transgranular cracking along the basal slip planes and intergranular cracking at HAGBs.

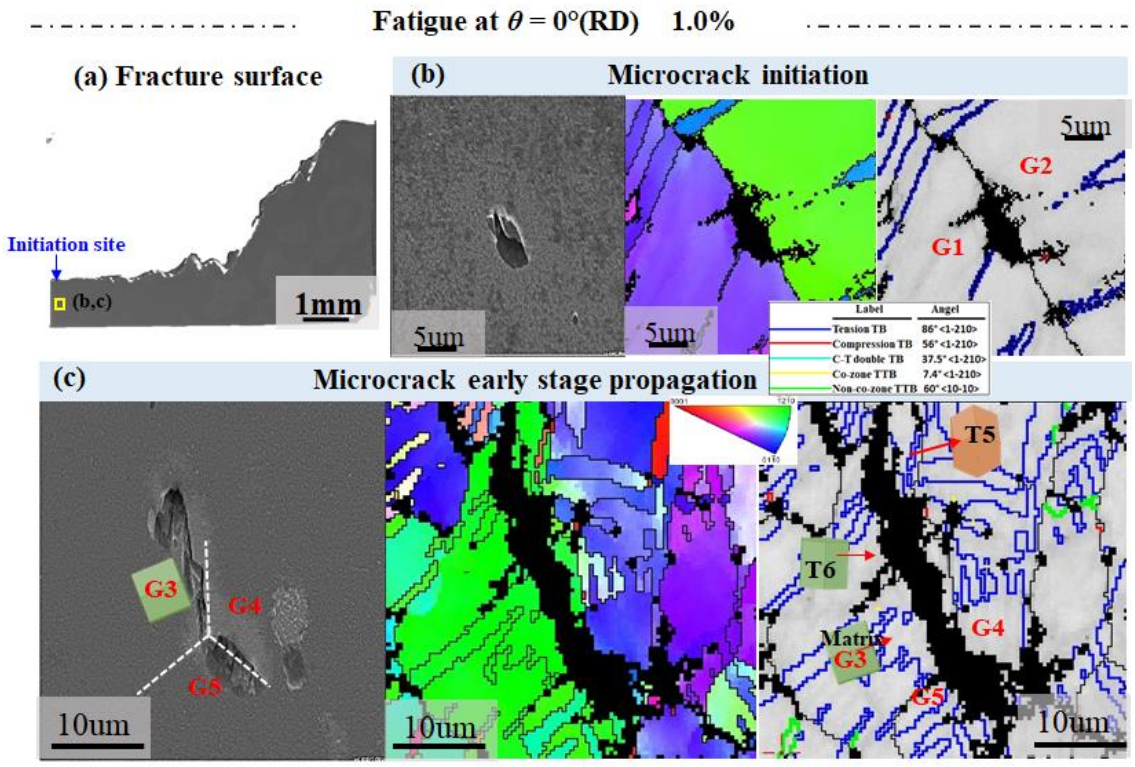

Fig. 6.7: Microcracks observed for the 0º (RD) specimen after fatigue experiment at the strain amplitude of 1.0%: (a) Side view of the fracture surface and (b,c) SEM image and EBSD results (IPF and IQ maps) showing the microstructural features surrounding the microcracks. In the IQ map, grain boundaries are denoted by black lines. Tension twin boundaries are colored in blue. Non-co zone twin-twin boundaries are delineated in green color.

When the strain amplitude is 0.22%, a microcrack sized within one grain is captured in Fig. 6.8a, which is observed to be align well with the trace of basal plane in grain G1. The microstructure in the vicinity of intermediate-sized microcrack which spans across several grains is characterized and shown in Fig. 6.8b. It is revealed that the microcrack propagated in either intergranular or transgranular mode. The intergranular paths were found inhabiting on the GBs with the misorientation angles higher than 18º. The transgranular path was found penetrating grain G2, following the basal plane.

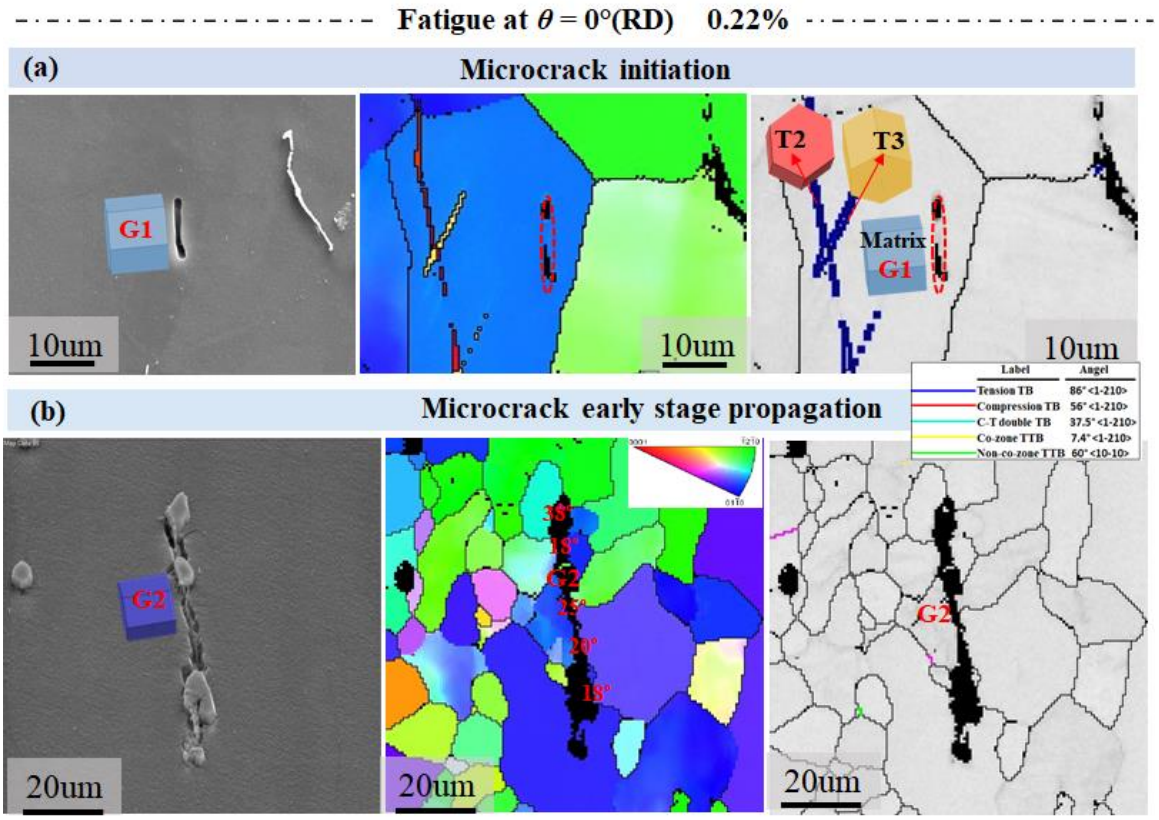

Fig. 6.8: Microcracks observed for the 0º(RD) specimen after fatigue experiment at the strain amplitude of 0.22%: (a,b) Side view of the fracture surface and (b,c) SEM image and EBSD results (IPF and IQ maps) showing the microstructural features surrounding the microcracks. In the IQ map, grain boundaries are denoted by black lines. Tension twin boundaries are colored in blue. The misorientation angles for the GBs between two neighboring grains are embedded in the IPF map.

6.2.2 Fatigue damage at θ = 22.5º

For material orientation θ = 22.5º, the overall macroscopic features of fracture surface depend on the strain amplitude (refer to Fig. 6.3). The low-magnification optical microscopic images for the side view of the fracture surface at the strain amplitudes of 3.0%, 0.75% and 0.25% are shown in Fig. 6.9. Under strain amplitude of 3.00%, the fracture surface exhibits an overall shear cracking behavior, with the normal direction for the early-stage propagation surface orientating approximately 67° to the loading direction. When the strain amplitude is 0.75% and 0.25%, an overall brittle-like fracture surface can be observed. Multiple fatigue cracks can be observed on the specimen surface when the strain amplitude is 1.0%, as seen in Fig. 6.9b.

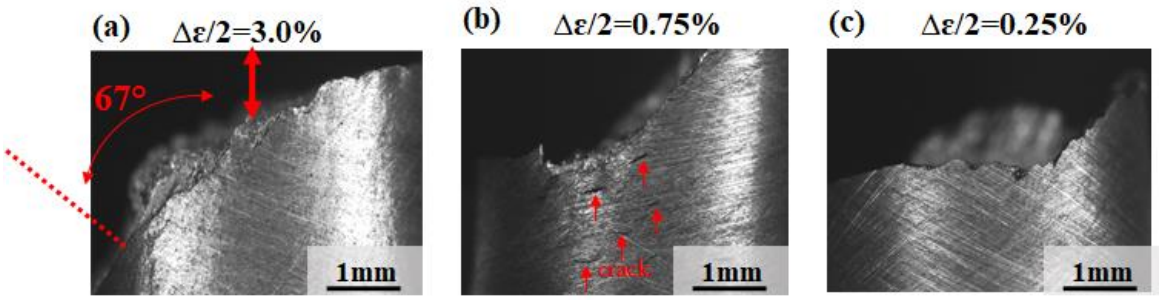

Fig. 6.9: Optical microscopic images for the side view of the fracture surface at the strain amplitude of (a) 3.0%, (b) 0.75% and (c) 0.25% for θ = 22.5º. Red arrows show the fatigue cracks on the specimen surface.

At the strain amplitude of 3.0%, the side view of fracture surface after fatigue experiment along with microcracks are presented in Fig. 6.10. The fracture surface near the specimen surface where the initiated site located with its normal direction tilts approximately 67° from the loading direction. Multiple microcracks can be detected at the local region below the initiation site. These microcracks orientate the same in-plane direction with respect to the initiation site region on the fracture surface.

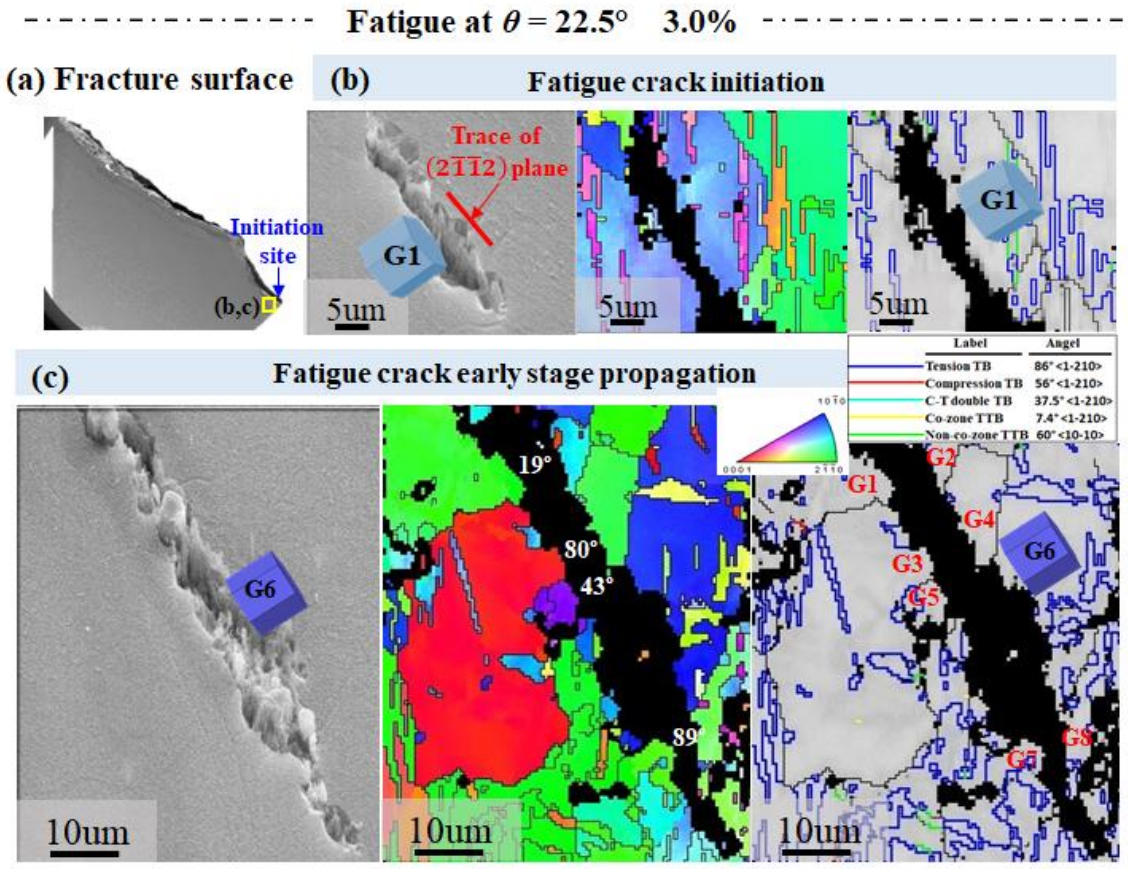

Fig. 6.10: Microcracks observed for the 22.5º specimen after fatigue experiment at 3.0% strain amplitude: (a) SEM image captured in the area near the fracture surface, which is sectioned by cutting the cylindrical specimen through its diameter and (b, c) SEM image along with EBSD results (IPF and IQ maps) showing the microstructural features surrounding the microcracks. The misorientation angles for the GBs between two neighboring grains are embedded in the IPF maps. In the IQ map, grain boundaries are denoted by black lines. Tension twin boundaries are colored in blue. Non co-zone twin-twin boundaries are delineated in green color.

A short microcrack sized approximately 20 μm observed in a single grain (G1) is shown in Fig. 6.10b. By conducting the trace analysis, it is found that the crystallographic plane

that the transgranular crack inhabited on is the basal (0001) plane and second-order pyramidal <c+a> $(2\bar{1}\bar{1}2)$ plane. The microstructure in the vicinity of intermediate-sized microcrack which spans several grains is shown in Fig. 6.10c. The microcrack propagates in either intergranular or transgranular mode. The intergranular paths are located on the GBs between G1-G2, G3-G4, G5-G4, and G7-G8, with the misorientation angles ranging from 19° to 89°. The transgranular path is observed to penetrating G6, following the basal plane. The observations in Fig. 6.10 indicate that the fatigue crack initiates from the cyclic slip bands of basal and pyramidal<c+a> slips, and propagates in either intergranular or transgranular mode.

As for the strain amplitude of 0.75%, the side view of the fracture surface and microcracks observed after the fatigue experiment are indicated in Fig. 6.11. Both transgranular cracking and intergranular cracking can be observed regardless of the applied strain amplitude. The misorientation angles for the GBs that the intergranular paths inhabiting on are embedded in the IPF maps. It can be observed in Figs. 6.11b-c that the transgranular paths for both microcrack A (located in G1) and microcrack B (located in G2) align well with the basal (0001) plane.

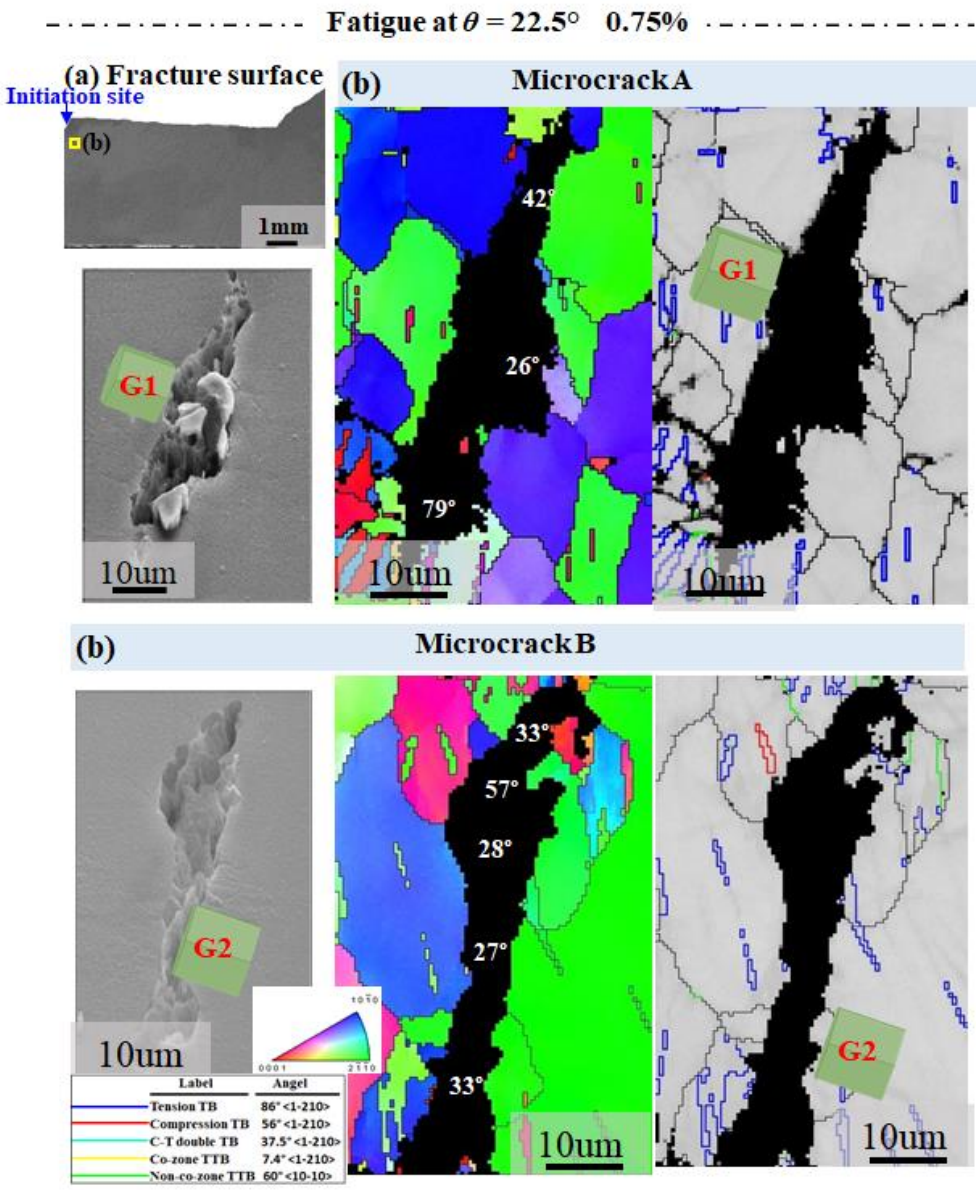

Fig. 6.11: Microcracks observed for the 22.5º specimen after fatigue experiment at the strain amplitude of 0.75%: (a) Side view of the fracture surface and (b,c) SEM image along with EBSD results (IPF and IQ maps) showing the microstructural features surrounding the microcracks. The misorientation angles for the GBs between two neighboring grains are embedded in the IPF maps. In the IQ map, grain boundaries are denoted by black lines. Tension and compression twin boundaries are colored in blue and red. Non co-zone twin-twin boundaries are delineated in green color.

Likewise, the microcrack observed after fatigue experiment at the strain amplitude of 0.25% propagates in either intergranular and transgranular mode, as shown in Fig. 6.12. The transgranular paths in G1, G2 and G3 follows the basal (0001) plane (Fig. 6.12b). The intergranular paths were located on the GBs with misorientation angles higher than 27°.

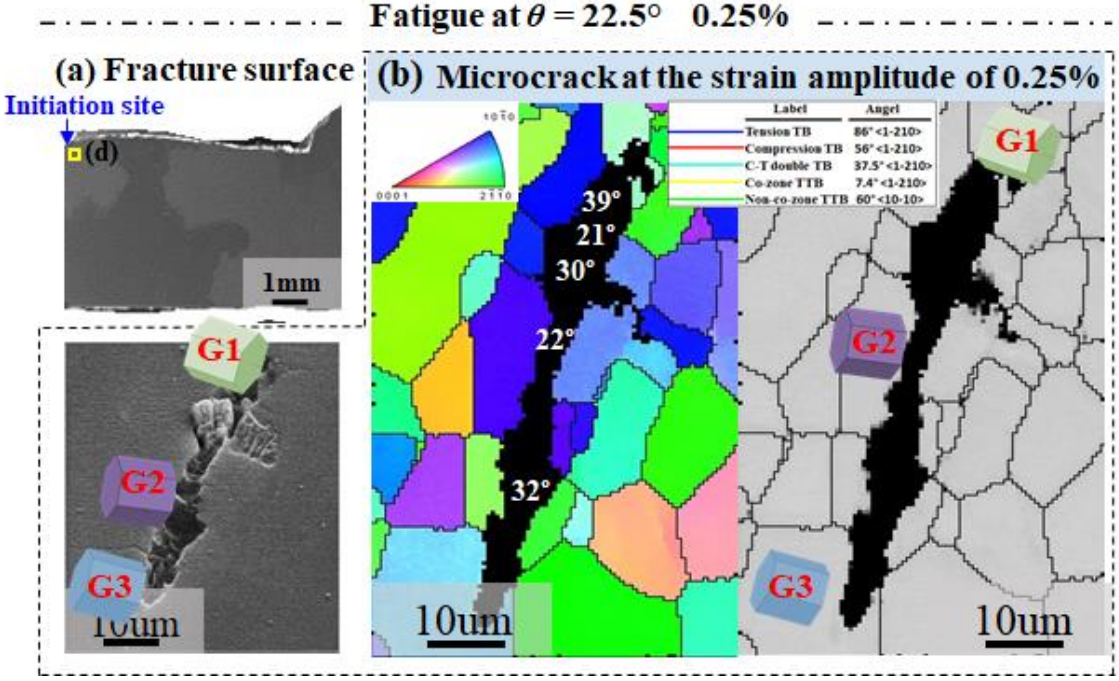

Fig. 6.12: Microcracks observed for the 22.5º specimen after fatigue experiment at the strain amplitude of 0.25%: (a) Side view of the fracture surface and (b) SEM image along with EBSD results (IPF and IQ maps) showing the microstructural features surrounding the microcrack. The misorientation angles for the GBs between two neighboring grains are embedded in the IPF maps. In the IQ map, grain boundaries are denoted by black lines.

6.2.3 Fatigue damage at θ = 45º

Distinguished from the brittle-like fracture mode for θ = 0º (RD), 67.5º and 90º (ND), the fracture mode for θ = 45º exhibit a shear cracking behavior at the strain amplitudes of 2.0%, 1.5% and 0.3% (refer to Fig. 6.3). The fracture surface near the specimen surface where the initiation site located tilts approximately 45° from the direction perpendicular to the loading direction, indicating that the fatigue crack may initiate and early propagate in a shearing mode along cyclic slip bands. Fig. 6.13 presents the optical microscopic images for the side view of fracture surface at the strain amplitude of 2.0%. 1.5% and 0.30%.

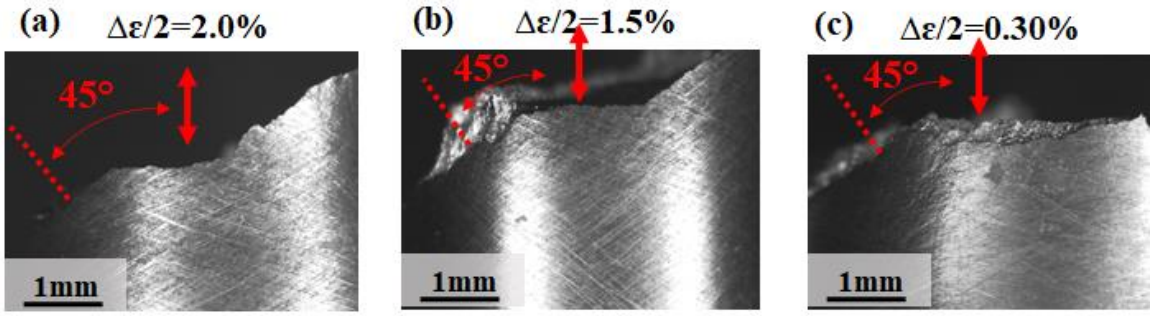

Fig. 6.13: Optical microscopic images for the side view of the fracture surface at the strain amplitude of (a) 2.0%, (b) 1.5% and (c) 0.30% for θ = 45º.

Fig. 6.14 presents the microcrack observed for the 45º specimen after fatigue experiment at the strain amplitude of 2.0%. From the side view of fracture surface as indicated in Fig. 6.14a, a shear macroscopic fracture behavior can be identified near the specimen surface. Multiple microcracks oriented approximately 45° from the loading direction can be observed at local region below the initiation site near the specimen surface. The region “b,c” in Fig. 6.14a is magnified in Fig. 6.14b and Fig. 6.14c and revealed by EBSD analysis to determine the microstructure surrounding the microcracks. In Fig. 6.14b, the transgranular microcrack penetrates grain 1(G1) and grain 2 (G2) orientated 45° from

the loading direction. Three different tension twin variants are activated in G1 and G2. Noticing that the lower tip of the microcrack is connected to the tension twin boundary of T2 in G1, while the upper tip of the microcrack coincided to be located on the non-co-zone twin-twin boundaries between T4 and T5 in G2. By conducting the trace analysis for G1, it was interesting to find that the habit plane of the microcrack is the basal (0001) plane with SF as high as 0.4755, and the pyramidal <c+a> $(2\bar{1}\bar{1}2)$ plane with SF of 0.3520. A longer crack with length of 50 μm is shown in Fig. 6.14c. The microcrack propagates in either intergranular or transgranular mode. For the transgranular cracking in G3, the trace analysis is conducted to determine the crystallographic plane that the crack inhabits on. It turns out that both the basal slip plane and the pyramidal <c+a> $(11\bar{2}2)$ plane coincides with the microcrack well. We conclude that the microcrack is likely nucleated from the local damage induced by the basal and pyramidal <c+a> slips and impingement damage of tension twins.

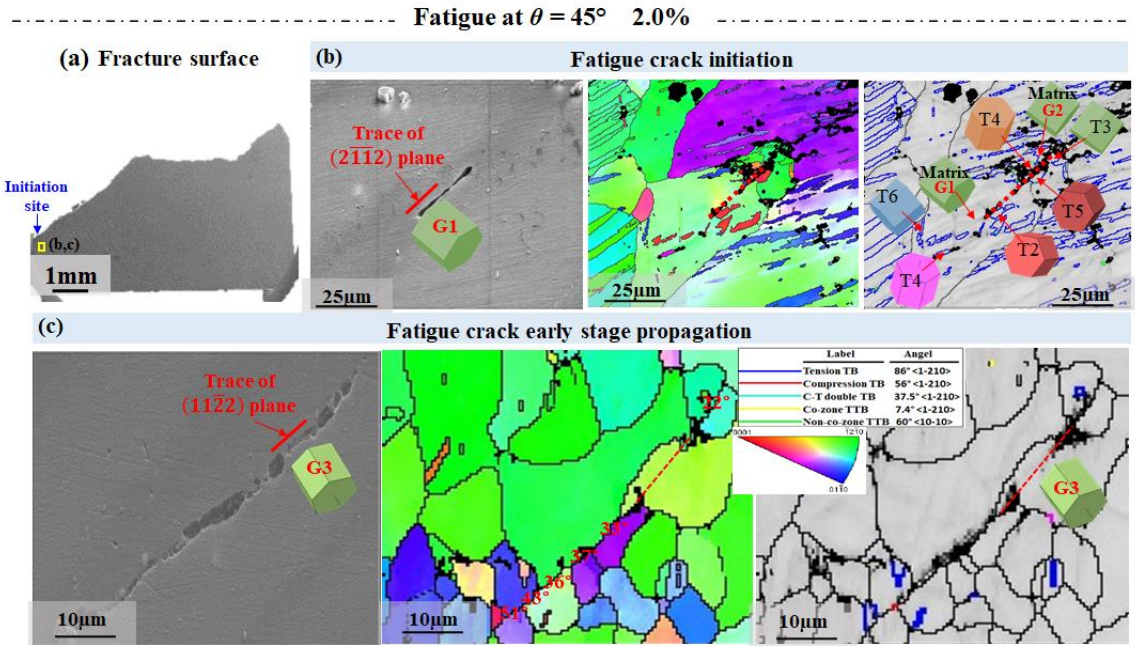

Fig. 6.14: Microcrack observed for the 45º specimen after fatigue experiment at the strain amplitude of 2.0%: (a) SEM image captured in the area near the fracture surface, which is sectioned by cutting the cylindrical specimen through its diameter and (b, c) SEM image along with EBSD results (IPF and IQ maps) showing the microstructural features surrounding the microcracks. The trace of pyramidal <c+a> $(2\bar{1}\bar{1}2)$ plane for G1 and the trace of pyramidal <c+a> $(11\bar{2}2)$ plane for G3 are embedded in (b) and (c), respectively.

When the strain amplitude is 1.5%, the microcracks after fatigue experiment are shown in Fig. 6.15. Similar to the case at the strain amplitude of 2.0%, the fracture surface of specimen at 1.5% strain amplitude also comprises of shear cracking behavior near the specimen surface, as shown in Fig. 6.15a. A short microcrack sized approximately 10 μm observed in a single grain is shown in Fig. 6.15b. As viewed in the IPF and IQ maps, pronounced tension twins are developed in a single grain and connected with tension twin and compression-tension (C-T) double twin. Different from the case with strain amplitude of 2.0%, the trace of the microcrack in Fig. 6.15b only coincides with the basal (0001) plane. It can be concluded that the microcrack is likely nucleated from the local damage

induced by the impingement of tension and/or double twin on the basal slip bands. For the early stage propagation path, both transgranular cracking and intergranular cracking can be observed in Fig. 6.15c. The transgranular cracking is along the basal plane penetrating G2. The intergranular cracking is observed to be located on the GBs.

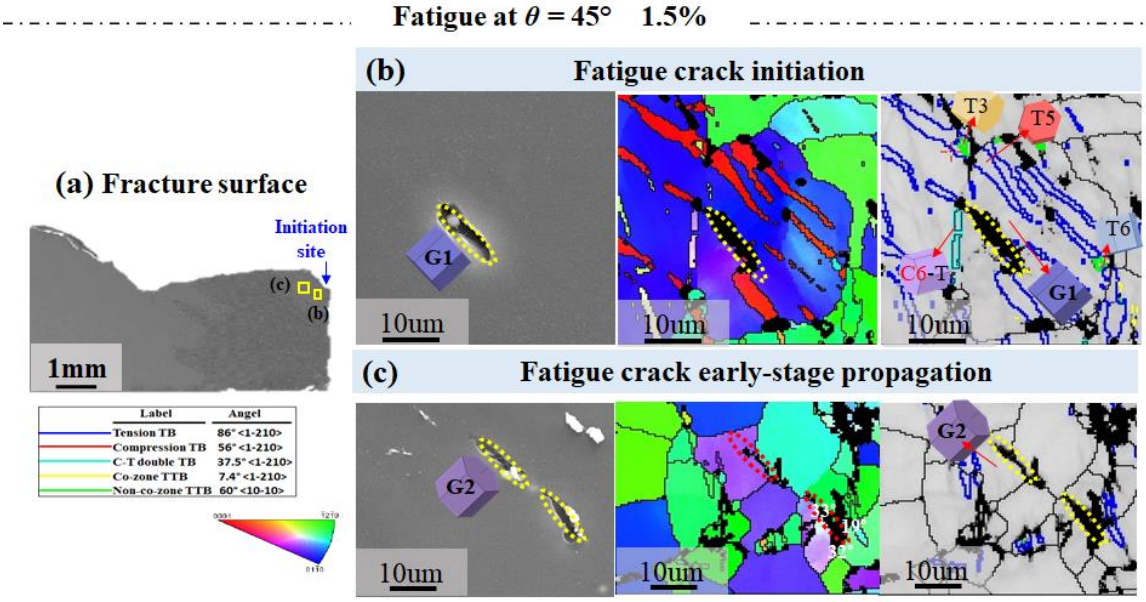

Fig. 6.15: Microcracks observed for the 45° specimen after fatigue experiment at 1.5%: At the strain amplitude of 1.5%, (a) side view of the fracture surface and (b,c) SEM image along with EBSD results (IPF and IQ) maps) showing the microstructural features surrounding the microcracks.

As for the strain amplitude of 0.3%, the side view of the fracture surface and fatigue microcrack is presented in Fig. 6.16a. Shear cracking can be observed near the specimen surface on the right side in Fig. 6.16a. Short and long cracks with the lengths ranging from 10 μm to 150 μm are observed at the local region near the specimen surface. From Fig. 6.16b, a microcrack with length of 10 μm is located inside the matrix grain following the basal plane. By examining a large microcrack spanning over several grains (Fig. 6.16c), the propagation path is both transgranular and intergranular. The misorientation angle

distributions for the GBs where the microcrack propagates along with is also shown in Fig. 6.16c. A fraction peak is located at the angles between 30° and 35°. It is suggested that for the 45º specimen at small strain amplitude of 0.3%, the fatigue crack is induced by basal slips and tends propagate along the GBs and basal planes.

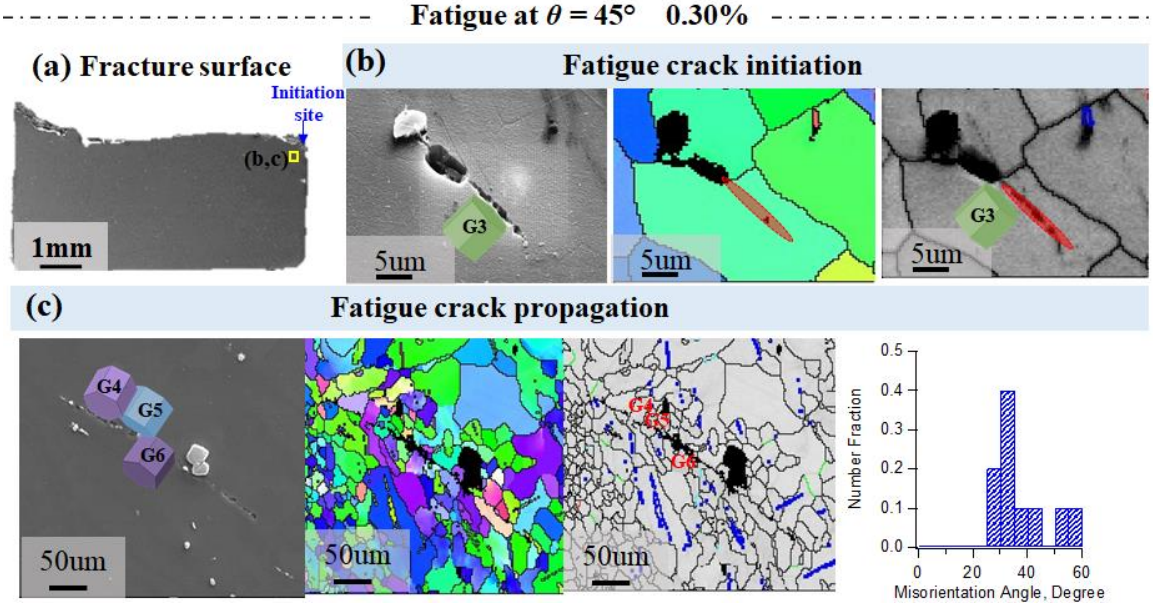

Fig. 6.16: Microcracks observed for the 45º specimen after fatigue experiment at 0.30%: (a) Side view of the fracture surface and (b,c) SEM image along with EBSD results (IPF and IQ) maps) showing the microstructural features surrounding the microcracks.

In summary, for material orientation θ = 45º, transgranular cracking can be observed regardless of applied strain amplitude. When the strain amplitude is 2.00% the transgranular cracking is induced by both basal and pyramidal <c+a> slips. While when the strain amplitude is 1.5% and 0.3%, the transgranular cracking is induced by only basal slip.

6.2.4 Fatigue damage at θ = 67.5º

Fig. 6.17 shows the low-magnification optical microscopic images for the side view of the fracture surface at the strain amplitudes of 3.0%, 0.75% and 0.20% for θ = 67.5º. The

fracture surface is oriented with normal direction tilting approximately 20° from the loading direction at the strain amplitude of 3.0%, as seen in Fig. 6.17a. When the strain amplitude is 0.75% and 0.20%, the fracture surface is oriented perpendicular to the loading direction (refer to Figs. 6.17b-c).

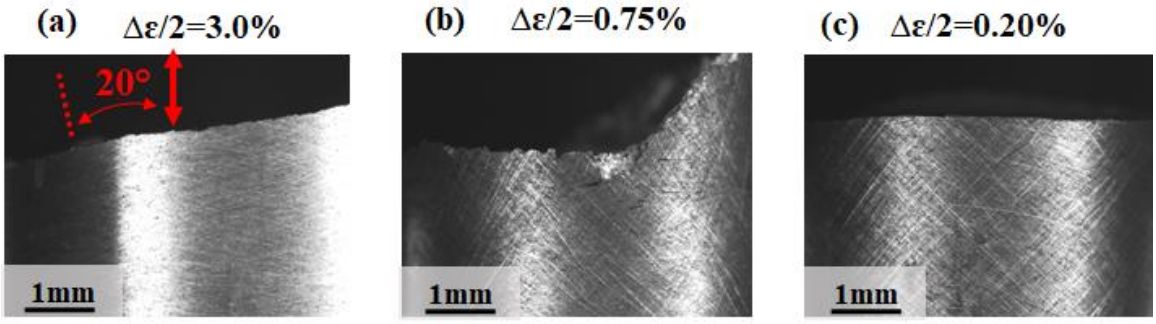

Fig. 6.17: Optical microscopic images for the side view of the fracture surface at the strain amplitude of (a) 3.0%, (b) 0.75% and (c) 0.20% for θ = 67.5º.

As for θ = 67.5º, the microcracks after fatigue experiments at the strain amplitude of 3.0%, 0.75% and 0.20% are presented in Fig. 6.18. When the strain amplitude is 3.0%, the side view of the side view of the fracture surface is shown in Fig. 6.18a, together with the microcracks observed near the specimen surface presented in Fig. 6.18b and Fig. 6.18c. The EBSD characterization for the micro-crack in Fig. 6.18b indicates that the fatigue damage initiated from the grain boundary between two neighboring grains with misorientation angle of 51°. From Fig. 6.18c, the microcrack propagates in either intergranular or transgranular mode. The intergranular cracking is inhabited on the grain boundaries with misorientation angles ranging from 19° to 35°. The transgranular cracking penetrates grain1 (G1) along the cyclic slip band. The crystallographic plane where transgranular cracking inhabited is revealed by conducting the trace analysis. For Grain 1, the traces of both the basal plane and pyramidal <c+a> $(2\bar{1}\bar{1}2)$ show the same alignment

with the microcrack. It can be concluded that the transgranular crack propagation inhabits on the basal or pyramidal <c+a> plane.

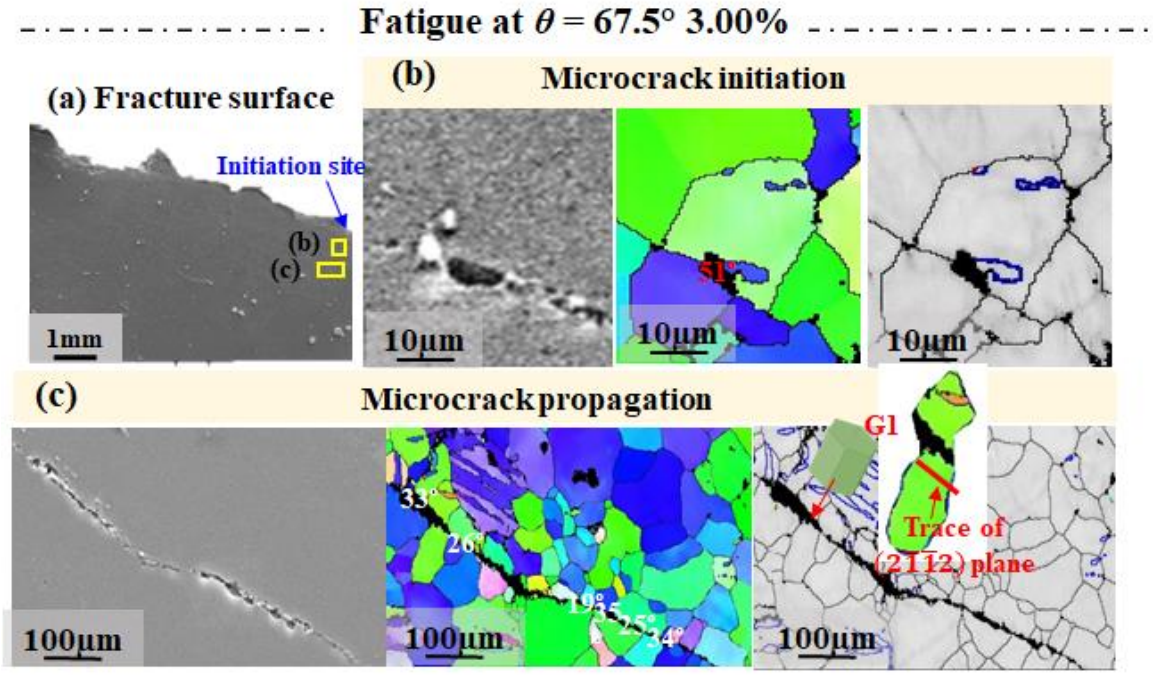

Fig. 6.18: Microcracks observed for the 67.5º specimen after fatigue experiment at 3.0%: (a) Side view of the fracture surface and (b,c) SEM image along with EBSD results (IPF and IQ) maps) showing the microstructural features surrounding the microcracks.

When the strain amplitude is 0.75%, the fracture surface including the region of initiation cite is perpendicular to the loading direction (refer to Fig. 6.19a). The microcrack is observed to be located on the triple joint of three neighboring grains, with misorientation angle of two neighboring grains ranging from 15° to 23°. Another longer microcrack is found to be located on the GBs with misorientation angles larger than 23°. This finding indicates that the fatigue crack initiates and propagates from the GBs. No transgranular cracking is found under this strain amplitude. As for the strain amplitude of 0.20%, the

fatigue crack propagation mode is found to be pure intergranular, as evidenced in Fig. 6.20, with misorientation angles ranging from 16° to 39°.

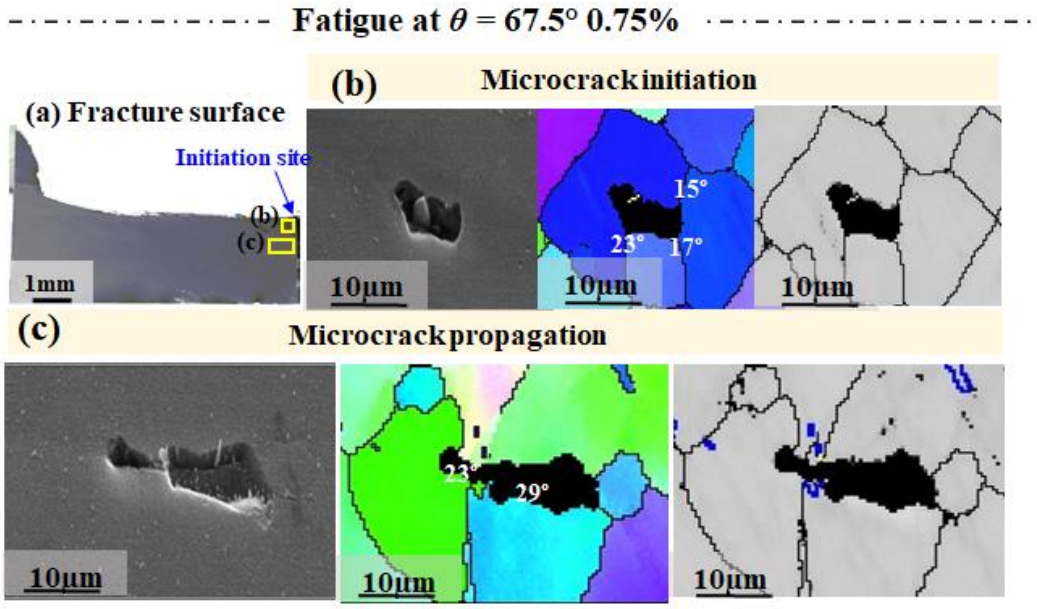

Fig. 6.19: Microcracks observed for the 67.5º specimen after fatigue experiment at 0.75%: (a) Side view of the fracture surface and (b,c) SEM image along with EBSD results (IPF and IQ) maps) showing the microstructural features surrounding the microcracks.

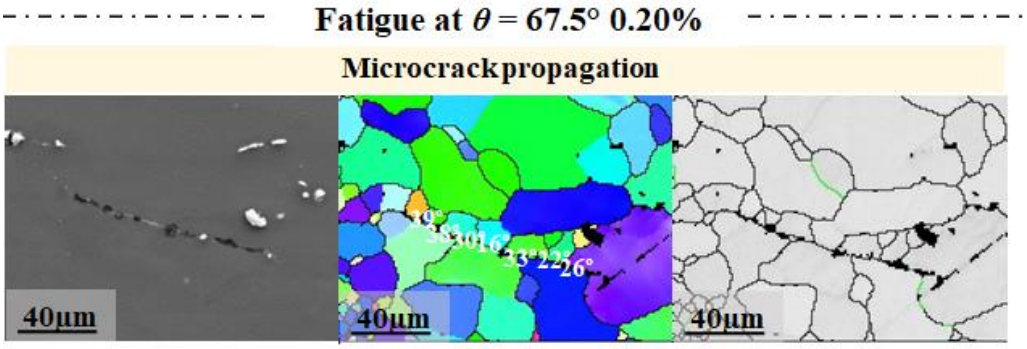

Fig. 6.20: Microcrack observed for the 67.5º specimen after fatigue experiment at 0.20%: SEM image along with EBSD results (IPF and IQ) maps) showing the microstructural features surrounding the microcrack.

6.2.5 Fatigue damage at θ = 90º (ND)

The fracture surfaces obtained from fatigue experiments at θ = 90º (ND) exhibit brittle-like features with fracture surface perpendicular to the loading direction (Z-axis), regardless of applied strain amplitude. Fig. 6.21a presents the side view of fracture surface together with microcracks observed for the 90º (ND) specimen after the fatigue experiment at 3.0% strain amplitude. The sample was cut along the diametric direction, approximately following the propagation direction. The fatigue crack initiation site is on the right side of the side view as being indicated in Fig. 6.21a. The observation window for the microcrack is captured near the specimen surface, below the initiation site. Multiple microcracks were detectable at local regions near the specimen surface. Two featuring regions, namely 'b' and 'c', were focus and magnified, as illustrated in Fig. 6.21b and Fig. 6.21c, respectively.

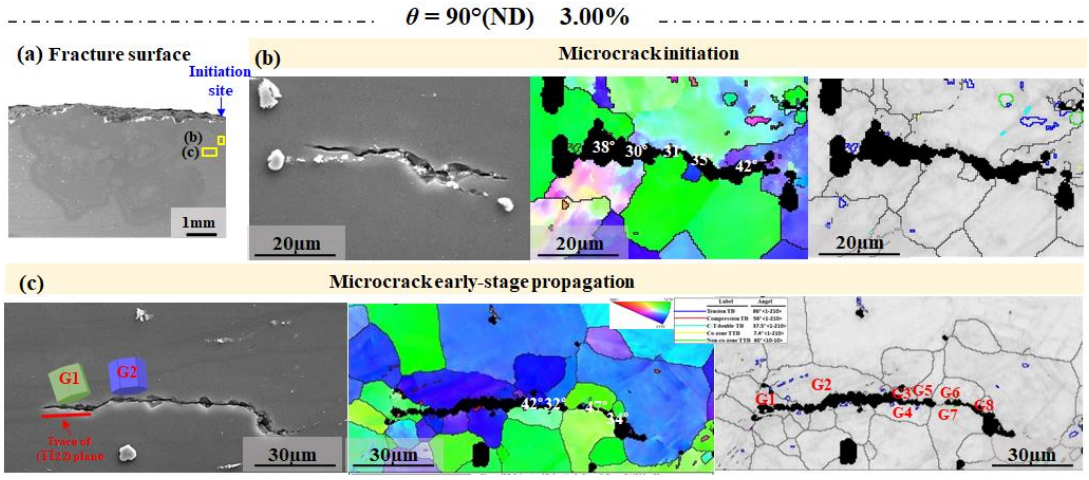

Fig. 6.21: Microcracks observed for the 90º (ND) specimen after fatigue experiment at 3.0% strain amplitude: (a) SEM image captured in the area near the fracture surface, which is sectioned by cutting the cylindrical specimen through its diameter and (b, c) SEM image along with EBSD results (IPF and IQ maps) showing the microstructural features surrounding the microcracks, the misorientation angles on the grain boundaries between

two neighboring grains are embedded in the IPF maps. The trace of the $(\bar{1}\bar{1}22)$ plane for G1 is also presented in the SEM image in Fig. 6.21c.

In order to clarify the fatigue crack initiation mode, the microstructure in the vicinity of a short microcrack sized approximately 50 μm passing along two grains is characterized in Fig. 6.21b. As viewed in the IPF and IQ maps in Fig. 6.21b, limited residual twins are developed in the grains. Further EBSD characterization reveals that the microcrack is located on the grain boundaries. The misorientation angles between two neighboring grains are embedded in the IPF map. The result indicates that the fatigue crack is favorable to be originated from high angle grain boundaries (HAGBs) with misorientation angles higher than 30°. To further elucidate the crack propagation mode, in particular during the early-growth stage, we characterized the microstructure in the vicinity of intermediate-sized microcrack which spans several grains, as shown in Fig. 6.21c. It is revealed that the microcrack propagated in both intergranular and transgranular mode, spanning over eight grains, namely from "Grain1 (G1)" to "Grain 8 (G8)". For the intergranular cracking along the GBs between "G3-G4", "G5-G4", "G6-G7", "G8-G7" pairs, the misorientation angles between two neighboring grains are ranging from 32° to 47°. Transgranular propagation mode is observed in G1 and G2. Noting that no twin boundary cracking was detected after fatigue experiment. To further identify the crystal plane on which microcrack propagates, trace analysis is conducted by comparing the projection of crystallographic plane with the projection of the microcrack. As indicated in Fig. 3c, the trace of second-order pyramidal <c+a> $(\bar{1}\bar{1}22)$ plane shows the same alignment with the microcrack for Grain1, with the Schmid factor (SF) value as high as 0.4827. For grain 2, the trace of basal (0001) plane shows the same alignment with the microcrack. This finding indicates that the transgranular

crack propagation inhabits on the basal or pyramidal <c+a> plane. The fatigue damage is induced by the stress concentration on the persistent slip bands formed by the accumulated basal slips and pyramidal slips during cyclic loading.

Fig. 6.22 presents the microcracks for the 90º (ND) specimen at 1.0% strain amplitude. When the strain amplitude is 1.0%, Fig. 6.22a shows the SEM images and EBSD results for a microcrack from a specimen which was fatigue tested after 60%N_f. Several fatigue cracks were detected on the specimen surface. The sample for EBSD analysis was cut along the diametrical direction, passing through one major fatigue crack. The microcrack in Fig. 6.22a with a length of 30 μm is located on the GBs with misorientation angles ranging from 21°to 40°. The fatigue damage after fatigue failure at the strain amplitude of 1.0% is indicated in Figs. 6.22(b-d). As shown in Fig. 6.22b, brittle-like features with fracture surface perpendicular to the loading direction is exhibited. The microstructure in the vicinity of microvoid near the specimen surface is characterized in Fig. 6.22c. It can be concluded that the microvoid is initiated from the triple joint of Grain1 (G1), Grain2 (G2) and Grain3 (G3), and developed at the GB between G2 and G3. The misorientation angles between the neighboring grains are 33°, 41° and 38° for G1-G2 pair, G2-G3 pair and G1-G3 pair. In Fig. 6.22d, the fatigue crack propagation mode is found to be pure intergranular. The histogram for the misorientation angles of GBs where the fatigue crack located on is also shown in Fig. 6.22d. A fraction peak is located at the angles between 15° and 20°.

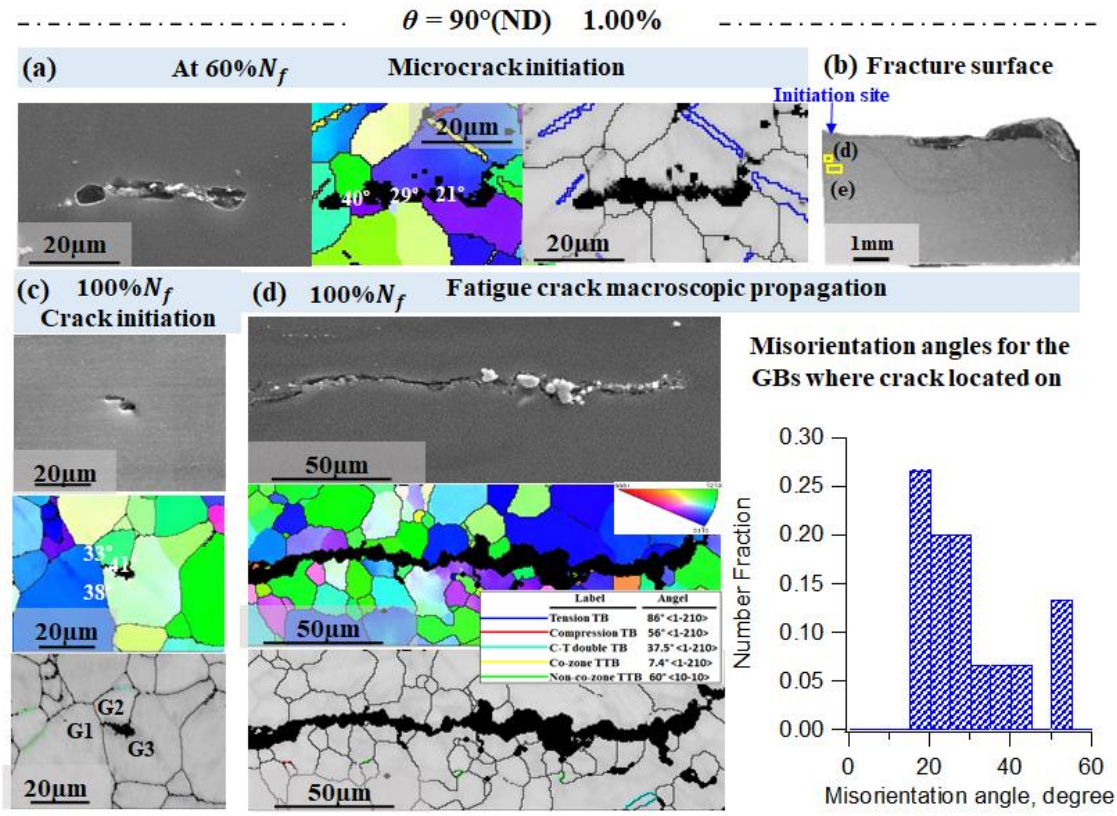

Fig. 6.22: Microcracks observed for the 90º (ND) specimen at the strain amplitude of 1.0%: (a) SEM image with EBSD results for the microcrack after 60%N_f, (b) side view of the fracture surface after fatigue experiment and (c,d) SEM image along with EBSD results (IPF and IQ maps) showing the microstructure features surrounding the microcracks after fatigue experiment.

At the strain amplitude of 0.14%, only microcracks with lengths larger than 50 μm are detectable, since the fatigue damage has been thoroughly developed during the high loading cycles at small strain amplitude. The microstructure surrounding a microcrack with length of 80 μm is revealed by EBSD analysis as indicated in Fig. 6.23. The misorientation angle distributions for the GBs where the microcrack propagates along with is also shown in Fig. 6.23. A fraction peak is located at the angles between 15° and 20°, and the angles between 50° and 55°.

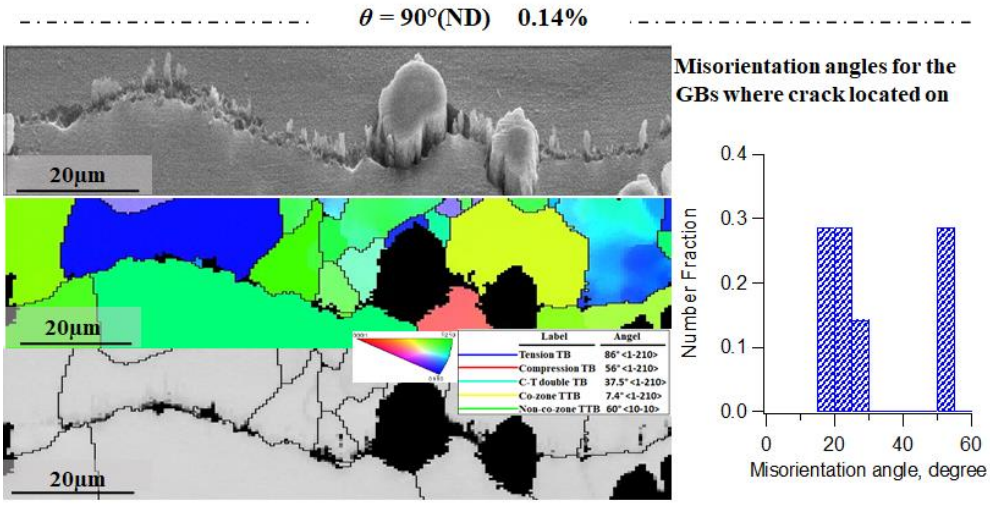

Fig. 6.23: The SEM image with EBSD results for Microcrack observed for the 90º (ND) specimen at the strain amplitude of 0.14, as well as the distribution of misorientation angles for the GBs between two neighboring grains where the fatigue crack located on.

To summarize, for material orientation θ = 90º, the fatigue crack initiates from GB regardless of loading magnitude. However, the applied strain amplitude can influence the fatigue crack early-stage propagation behavior. When the strain amplitude is 3.0%, both intergranular and transgranular cracking can be observed and the transgranular cracking is induced by both basal and pyramidal <c+a> slips. When the strain amplitude is 1.0% and 0.14%, only intergranular cracking can be observed. The intergranular cracking tends to located on the HAGBs with misorientation angles larger than 15°. No twin boundary cracking is detected.

The material orientation of θ = 67.5º exhibit similar fatigue damage initiation and early stage propagation behavior as θ = 90º (ND). However the macroscopic fracture feature for this two material orientation is slightly different when the strain amplitude is 3.0% (above the upper kink point). Comparing with the ND with fracture surface perpendicular to the loading direction, the fracture surface of θ = 67.5º oriented with normal direction tilting

approximately 20° from the loading direction. It is important to note that the transgranular cracking is inhabited on the basal plane or pyramidal <c+a> plane, resulting in the preferred macroscopic propagation direction for $\theta = 67.5^{o}$ and 90^{o} (ND). For $\theta = 90^{o}$ (ND), the majority of the texture has basal planes perpendicular to the loading direction, leading to the preferred macroscopic propagation direction perpendicular to the loading direction. However, for $\theta = 67.5^{o}$ with *c*-axis of texture tilting by approximately 20° from the loading direction, thus the transgranular cracking path will be oriented with approximately 22° from the direction perpendicular to the loading direction.

6.3 Summary

A comprehensive experimental study of the material orientation effect on the fatigue properties of a rolled AZ31B Mg alloy was performed with fully reversed strain-controlled tension-compression fatigue experiments in five material orientations with fatigue lives ranging from few loading cycles to over 10^6 cycles. The following conclusions can be drawn from the study,

1) Overall, the strain-life fatigue curves of all the five material orientations fall in a relatively narrow band. Anisotropic fatigue properties are reflected in the stress-life curves. The RD material orientation has the highest stress-life curve and the 45º orientation has the lowest.
2) The loading magnitude and material orientation affects the macroscopic fracture features at the initiation and early-stage propagation region on the fracture surface. Fatigue at θ = 0º (RD), 67.5º and 90º (ND) results in brittle-like fracture surfaces, while fatigue at θ = 22.5º and 45º displays shear macroscopic cracking behavior at the local region. The overall fatigue cracking behavior is related to the upper kink point for all the five material orientations.
3) For θ = 67.5º and 90º(ND), grain boundary microcrack initiation is persistent under three different strain amplitudes. However, the early stage microcrack propagation modes are dependent on the cyclic loading amplitude. Transgranular cracking only occurs when the strain amplitude is above the upper kink point, which is induced by the basal and non-basal cyclic slip bands. Grain boundary cracking exists regardless of the strain amplitudes. No twin boundary cracking is identified.

4) For $\theta = \theta = 0^{o}$ (RD), 22.5^{o} and 45^{o}, both intergranular and transgranular crack growth modes exist at different loading amplitudes. However, the mechanism of early-stage transgranular crack propagation are different at high and low strain amplitudes. When the strain amplitude is above the upper kink point, the transgranular cracking inhabits on both basal slip bands and non-basal slip bands. As for the strain amplitude below the upper kink point, the transgranular cracking is only induced by basal slip.

7 Conclusions

In the current research, monotonic tension, monotonic compression, and cyclic fully reversed strain-controlled tension-compression experiments were carried out on rolled AZ31B Mg alloy specimens taken from five different material orientations: θ = 0º, 22.5º, 45º, 67.5º and 90º with respect to the rolled direction (RD). θ denotes the angle between the axial direction of the testing specimen and the rolled direction of the material. The monotonic deformation and fracture, cyclic deformation and fatigue behavior, as well as detailed associated orientation-dependent microscopic mechanisms are comprehensively studied for the first time in five material orientations. Based on the experimental results, major conclusions are drawn as follows:

1. For the static properties, the elastic limit under tension is identical to that under compression for any given material orientation with the highest to lowest following the order 0°(RD), 90°(ND), 67.5°, 22.5°, and 45°. The ultimate strength and true fracture strength are higher under compression than these under tension for a given material orientation. The true fracture stress and ductility are the highest in the RD (0°). Significant tension-compression asymmetry can be identified in the stress-strain curves due to the strong texture. Microyielding is induced by the activation of basal slips.
2. The material orientation affects the macroscopic fracture behavior under monotonic tension. Tension at θ = 0º, 67.5, and 90º results in irregular-shaped brittle-like features composed of ridges and islands. While tension at θ = 22.5º and 45 ° displays flat shear fracture behavior.

3. The microstructural origins of brittle-like cracking are different between the case of tension at θ = 0º and that of tension at θ = 67.5º and 90º. Twin boundary cracking in compression and/or compression-tension double twins is commonly detected in tension at $\theta = 0°$ whereas high-angle grain boundary cracking, which is facilitated by the impingements of tension-compression-tension tertiary twins and the none co-zone twin-twin boundaries, acts as the crack initiation mode in tension at θ = 67.5º and 90º. Crack initiation under tension at θ = 22.5º and 45º is originated from shear deformation in the basal slip bands at local damages induced by impingement of tension, compression and/or compression-tension twins. Crack extension is driven by localized shear deformation in basal slip bands which can be transmitted across neighboring grains, resulting in a final crack path following basal plane traces.
4. The strain-life fatigue curve of any given material orientation is characterized by two kink points. The cyclic stress-strain hysteresis loop is symmetric when strain amplitude is lower than the lower kink point. When the strain amplitude is in between the upper and lower kink points, the asymmetric stress-strain hysteresis loop contains one inflection point which signifies completion of detwinning and start of non-basal slips. When the strain amplitude is higher than the upper kink point, the stress-strain hysteresis loop tends to be symmetric with both upper and lower branches having a sigmodal shape. Cyclic hardening is proportional to the loading amplitude and is observed for all the five material orientations when the strain amplitude is higher than the lower kink point. Positive mean stresses are shown in the $\theta < 45^{\circ}$ material orientations and compressive mean stresses are found in the $\theta > 45^{\circ}$ material orientations. The $\theta = 45^{\circ}$ material orientation has virtually zero mean stresses.

5. Significant anisotropy is exhibited in the detailed plastic deformation. For the material orientation $\theta \neq 45^{o}$, the deformation mechanism exhibits a pronounced tension-compression asymmetry, which is reflected by the different evolution behavior of elastic limit range on the tension and compression reversals, with respect to the number of loading cycles and loading magnitude. The value of elastic limit range on the loading reversals which is favorable for detwinning, is intrinsically related to the twin volume fraction at the peak stress prior to the loading reversal. A strong material dependence can be observed in the elastic limit range during cyclic loading, revealed by its highest value at $\theta = 0^{o}$ and lowest value at $\theta = 45^{o}$.
6. For the material orientation $\theta = 45^{o}$, the values of elastic limit range on the tension and compression reversals are approximately identical irrespective of the number of loading cycles and loading magnitude. Twinning occurs in one group of grains and simultaneously detwinning occurs in another group of grains during loading and during reversed loading. The Schmid factor for twinning is statistically low in the 45° orientation specimens, thus low percentage of grains favorable for twinning, as compared with the other material orientations. Consequently, the strain amplitude corresponding to the lower kink point in the strain-life fatigue curve in the 45° material orientation is the highest among all the material orientations.
7. As for the fatigue properties, the strain-life fatigue curves of all the five material orientations fall in a relatively narrow band. The strain-life fatigue curve of any given material orientation is characterized by two kink points. Anisotropic fatigue properties are reflected in the stress-life curves. The RD material orientation has the highest stress-life curve and the 45° orientation has the lowest.

8. The loading magnitude and material orientation affects the macroscopic fracture features at the initiation and early-stage propagation region on the fracture surface. Fatigue at $\theta = 0^{o}$ (RD), 67.5^{o} and 90^{o} (ND) results in brittle-like fracture surfaces, while fatigue at $\theta = 22.5^{o}$ and 45^{o} displays shear macroscopic cracking behavior at the local region.
9. For $\theta = 0^{o}$ (RD), 22.5^{o} and 45^{o} both intergranular and transgranular crack growth modes exist at different loading amplitudes. However, the mechanism of early-stage transgranular crack propagation are different at high and low strain amplitudes. When the strain amplitude is above the upper kink point, the transgranular cracking inhabits on both basal slip bands and non-basal slip bands. As for the strain amplitude below the upper kink point, the transgranular cracking is only induced by basal slip.
10. Pertaining to the fatigue damage for $\theta = 67.5^{o}$ and 90^{o} (ND), grain boundary microcrack initiation is persistent under three different strain amplitudes. However, the early stage microcrack propagation modes are dependent on the cyclic loading amplitude. Transgranular cracking only occurs when the strain amplitude is above the upper kink point, which is induced by the basal and non-basal cyclic slip bands. Grain boundary cracking exists regardless of the strain amplitudes. No twin boundary cracking is identified.

References

[1] B.L. Mordike, T. Ebert, Magnesium Properties - applications - potential, Mater. Sci. Eng. A. 302 (2001) 37–45. https://doi.org/10.1016/S0921-5093(00)01351-4.

[2] T.M. Pollock, Weight loss with magnesium alloys, Science (80-.). 328 (2010) 986–987. https://doi.org/10.1126/science.1182848.

[3] S. Lee, H.J. Ham, S.Y. Kwon, S.W. Kim, C.M. Suh, Thermal conductivity of magnesium alloys in the temperature range from -125 C to 400 C, Int. J. Thermophys. 34 (2013) 2343–2350. https://doi.org/10.1007/s10765-011-1145-1.

[4] S. Wu, Z. Ji, T. Zhang, Microstructure and mechanical properties of AZ31B magnesium alloy recycled by solid-state process from different size chips, J. Mater. Process. Technol. 209 (2009) 5319–5324. https://doi.org/10.1016/j.jmatprotec.2009.04.002.

[5] C.J. Bettles, M.A. Gibson, Current wrought magnesium alloys: Strengths and weaknesses, Jom. 57 (2005) 46–49. https://doi.org/10.1007/s11837-005-0095-0.

[6] G.S. Frankel, Magnesium alloys: Ready for the road, Nat. Mater. 14 (2015) 1189–1190. https://doi.org/10.1038/nmat4453.

[7] D.S. Mehta, S.H. Masood, W.Q. Song, Investigation of wear properties of magnesium and aluminum alloys for automotive applications, J. Mater. Process. Technol. (2004). https://doi.org/10.1016/j.jmatprotec.2004.04.247.

[8] M.P. Staiger, A.M. Pietak, J. Huadmai, G. Dias, Magnesium and its alloys as orthopedic biomaterials: A review, Biomaterials. 27 (2006) 1728–1734. https://doi.org/10.1016/j.biomaterials.2005.10.003.

[9] L.Y. Chen, J.Q. Xu, H. Choi, M. Pozuelo, X. Ma, S. Bhowmick, J.M. Yang, S. Mathaudhu, X.C. Li, Processing and properties of magnesium containing a dense uniform dispersion of nanoparticles, Nature. 528 (2015) 539–543. https://doi.org/10.1038/nature16445.

[10] S.R. Agnew, Wrought magnesium: A 21st century outlook, Jom. 56 (2004) 20–21. https://doi.org/10.1007/s11837-004-0120-8.

[11] S. Yi, J. Bohlen, F. Heinemann, D. Letzig, Mechanical anisotropy and deep drawing behaviour of AZ31 and ZE10 magnesium alloy sheets, Acta Mater. 58 (2010) 592–605. https://doi.org/10.1016/j.actamat.2009.09.038.

[12] S.H. Park, J.H. Lee, B.G. Moon, B.S. You, Tension-compression yield asymmetry in as-cast magnesium alloy, J. Alloys Compd. 617 (2014) 277–280. https://doi.org/10.1016/j.jallcom.2014.07.164.

[13] Z. Wu, W.A. Curtin, The origins of high hardening and low ductility in magnesium, Nature. 526 (2015) 62–67. https://doi.org/10.1038/nature15364.

[14] G. Nayyeri, W.J. Poole, C.W. Sinclair, S. Zaefferer, Measurement of the critical resolved shear stress for basal slip in magnesium alloys using instrumented indentation, Scr. Mater. 156 (2018) 37–41. https://doi.org/10.1016/j.scriptamat.2018.07.003.

[15] J.D. Robson, N. Stanford, M.R. Barnett, Effect of precipitate shape on slip and twinning in magnesium alloys, Acta Mater. 59 (2011) 1945–1956. https://doi.org/10.1016/j.actamat.2010.11.060.

[16] M. Arul Kumar, A.K. Kanjarla, S.R. Niezgoda, R.A. Lebensohn, C.N. Tomé, Numerical study of the stress state of a deformation twin in magnesium, Acta Mater. 84 (2015) 349–358. https://doi.org/10.1016/j.actamat.2014.10.048.
[17] K.H. Kim, J.B. Jeon, N.J. Kim, B.J. Lee, Role of yttrium in activation of "c + a" slip in magnesium: An atomistic approach, Scr. Mater. 108 (2015) 104–108. https://doi.org/10.1016/j.scriptamat.2015.06.028.
[18] R.E. Smallman, Plasticity of crystals with special reference to metals by E. Schmid and W. Boas , Acta Crystallogr. Sect. A. 25 (1969) 587–588. https://doi.org/10.1107/s0567739469001306.
[19] E.C. Burke, W.R. Hibbard, Plastic Deformation of Magnesium Single Crystals, JOM. 4 (1952) 295–303. https://doi.org/10.1007/BF03397694.
[20] P.W. Bakarian, Glide and Twinning in Magnesium Single Crystals at Elevated Temperatures, Yale University, 1941.
[21] H. Asada, H. Yoshinaga, Temperature and orientation dependence of the plasticity of magnesium single crystals, J. Japan Inst. Met. 23 (1959) 649–652.
[22] B. Bhattacharya, M. Niewczas, Work-hardening behaviour of Mg single crystals oriented for basal slip, Philos. Mag. 91 (2011) 2227–2247.
[23] R.E. Reed-Hill, W.D. Robertson, Deformation of magnesium single crystals by nonbasal slip, Jom. 9 (1957) 496–502.
[24] A. Chapuis, J.H. Driver, Temperature dependency of slip and twinning in plane strain compressed magnesium single crystals, Acta Mater. 59 (2011) 1986–1994. https://doi.org/10.1016/j.actamat.2010.11.064.
[25] B.C. Wonsiewicz, Plasticity of magnesium crystals., Massachusetts Institute of Technology, 1966.
[26] T. Obara, H. Yoshinga, S. Morozumi, ${$11$\bar{2}$2$}$< 1123> Slip system in magnesium, Acta Metall. 21 (1973) 845–853.
[27] R.E. Reed-Hill, W.D. Robertson, Additional modes of deformation twinning in magnesium, Acta Metall. 5 (1957) 717–727.
[28] H. Miura*, X. Yang, T. Sakai, H. Nogawa, S. Miura, Y. Watanabe, J.J. Jonas, High temperature deformation and extended plasticity in Mg single crystals, Philos. Mag. 85 (2005) 3553–3565.
[29] Q. Yu, J. Zhang, Y. Jiang, Direct observation of twinning--detwinning--retwinning on magnesium single crystal subjected to strain-controlled cyclic tension--compression in [0 0 0 1] direction, Philos. Mag. Lett. 91 (2011) 757–765.
[30] H. Yoshinaga, R. Horiuchi, Deformation mechanisms in magnesium single crystals compressed in the direction parallel to hexagonal axis, Trans. Japan Inst. Met. 4 (1963) 1–8.
[31] G.E. Mann, T. Sumitomo, C.H. Cáceres, J.R. Griffiths, Reversible plastic strain during cyclic loading-unloading of Mg and Mg-Zn alloys, Mater. Sci. Eng. A. 456 (2007) 138–146. https://doi.org/10.1016/j.msea.2006.11.160.
[32] C.H. Cáceres, T. Sumitomo, M. Veidt, Pseudoelastic behaviour of cast magnesium AZ91 alloy under cyclic loading-unloading, Acta Mater. 51 (2003) 6211–6218. https://doi.org/10.1016/S1359-6454(03)00444-0.
[33] S.M. Yin, H.J. Yang, S.X. Li, S.D. Wu, F. Yang, Cyclic deformation behavior of as-extruded Mg-3%Al-1%Zn, Scr. Mater. 58 (2008) 751–754.

https://doi.org/10.1016/j.scriptamat.2007.12.020.
[34] F. Wang, S. Sandlöbes, M. Diehl, L. Sharma, F. Roters, D. Raabe, In situ observation of collective grain-scale mechanics in Mg and Mg-rare earth alloys, Acta Mater. 80 (2014) 77–93. https://doi.org/10.1016/j.actamat.2014.07.048.
[35] D. Hou, T. Liu, H. Chen, D. Shi, C. Ran, F. Pan, Analysis of the microstructure and deformation mechanisms by compression along normal direction in a rolled AZ31 magnesium alloy, Mater. Sci. Eng. A. 660 (2016) 102–107. https://doi.org/10.1016/j.msea.2016.02.020.
[36] B. Song, R. Xin, G. Chen, X. Zhang, Q. Liu, Improving tensile and compressive properties of magnesium alloy plates by pre-cold rolling, Scr. Mater. 66 (2012) 1061–1064. https://doi.org/10.1016/j.scriptamat.2012.02.047.
[37] S. Niknejad, S. Esmaeili, N.Y. Zhou, The role of double twinning on transgranular fracture in magnesium AZ61 in a localized stress field, Acta Mater. 102 (2016) 1–16. https://doi.org/10.1016/j.actamat.2015.09.026.
[38] J. Koike, R. Ohyama, Geometrical criterion for the activation of prismatic slip in AZ61 Mg alloy sheets deformed at room temperature, Acta Mater. 53 (2005) 1963–1972. https://doi.org/10.1016/j.actamat.2005.01.008.
[39] X.Y. Lou, M. Li, R.K. Boger, S.R. Agnew, R.H. Wagoner, Hardening evolution of AZ31B Mg sheet, Int. J. Plast. 23 (2007) 44–86. https://doi.org/10.1016/j.ijplas.2006.03.005.
[40] C. Guo, R. Xin, C. Ding, B. Song, Q. Liu, Understanding of variant selection and twin patterns in compressed Mg alloy sheets via combined analysis of Schmid factor and strain compatibility factor, Mater. Sci. Eng. A. 609 (2014) 92–101. https://doi.org/10.1016/j.msea.2014.04.103.
[41] H. Yu, C. Li, Y. Xin, A. Chapuis, X. Huang, Q. Liu, The mechanism for the high dependence of the Hall-Petch slope for twinning/slip on texture in Mg alloys, Acta Mater. 128 (2017) 313–326. https://doi.org/10.1016/j.actamat.2017.02.044.
[42] Z.Z. Shi, X.F. Liu, Characteristics of cross grain boundary contraction twin pairs and bands in a deformed Mg alloy, J. Alloys Compd. 692 (2017) 274–279. https://doi.org/10.1016/j.jallcom.2016.09.024.
[43] N. V. Dudamell, I. Ulacia, F. Gálvez, S. Yi, J. Bohlen, D. Letzig, I. Hurtado, M.T. Pérez-Prado, Twinning and grain subdivision during dynamic deformation of a Mg AZ31 sheet alloy at room temperature, Acta Mater. 59 (2011) 6949–6962. https://doi.org/10.1016/j.actamat.2011.07.047.
[44] M. Hou, H. Zhang, J. Fan, Q. Zhang, L. Wang, H. Dong, B. Xu, Microstructure evolution and deformation behaviors of AZ31 Mg alloy with different grain orientation during uniaxial compression, J. Alloys Compd. 741 (2018) 514–526. https://doi.org/10.1016/j.jallcom.2017.12.312.
[45] H. Wang, C.J. Boehlert, Q.D. Wang, D.D. Yin, W.J. Ding, In-situ analysis of the tensile deformation modes and anisotropy of extruded Mg-10Gd-3Y-0.5Zr (wt.%) at elevated temperatures, Int. J. Plast. 84 (2016) 255–276. https://doi.org/10.1016/j.ijplas.2016.06.001.
[46] C.J. Boehlert, Z. Chen, I. Gutiérrez-Urrutia, J. Llorca, M.T. Pérez-Prado, In situ analysis of the tensile and tensile-creep deformation mechanisms in rolled AZ31, Acta Mater. 60 (2012) 1889–1904. https://doi.org/10.1016/j.actamat.2011.10.025.

[47] A. Chakkedath, T. Maiti, J. Bohlen, S. Yi, D. Letzig, P. Eisenlohr, C.J. Boehlert, Contraction Twinning Dominated Tensile Deformation and Subsequent Fracture in Extruded Mg-1Mn (Wt Pct) at Ambient Temperature, Metall. Mater. Trans. A Phys. Metall. Mater. Sci. 49 (2018) 2441–2454. https://doi.org/10.1007/s11661-018-4557-8.

[48] S.H. Park, S.G. Hong, W. Bang, C.S. Lee, Effect of anisotropy on the low-cycle fatigue behavior of rolled AZ31 magnesium alloy, Mater. Sci. Eng. A. 527 (2010) 417–423. https://doi.org/10.1016/j.msea.2009.08.044.

[49] S. Begum, D.L. Chen, S. Xu, A.A. Luo, Effect of strain ratio and strain rate on low cycle fatigue behavior of AZ31 wrought magnesium alloy, Mater. Sci. Eng. A. 517 (2009) 334–343. https://doi.org/10.1016/j.msea.2009.04.051.

[50] Y. Xiong, Q. Yu, Y. Jiang, Cyclic deformation and fatigue of extruded AZ31B magnesium alloy under different strain ratios, Mater. Sci. Eng. A. 649 (2016) 93–103. https://doi.org/10.1016/j.msea.2015.09.084.

[51] S.H. Park, S.G. Hong, J. Yoon, C.S. Lee, Influence of loading direction on the anisotropic fatigue properties of rolled magnesium alloy, Int. J. Fatigue. 87 (2016) 210–215. https://doi.org/10.1016/j.ijfatigue.2016.01.026.

[52] J.B. Jordon, H.R. Brown, H. El Kadiri, H.M. Kistler, R.L. Lett, J.C. Baird, A.A. Luo, Investigation of fatigue anisotropy in an extruded magnesium alloy, Int. J. Fatigue. 51 (2013) 8–14. https://doi.org/10.1016/j.ijfatigue.2013.01.006.

[53] S. Ishihara, S. Taneguchi, H. Shibata, T. Goshima, A. Saiki, Anisotropy of the fatigue behavior of extruded and rolled magnesium alloys, Int. J. Fatigue. 50 (2013) 94–100. https://doi.org/10.1016/j.ijfatigue.2012.02.011.

[54] L. Wu, S.R. Agnew, Y. Ren, D.W. Brown, B. Clausen, G.M. Stoica, H.R. Wenk, P.K. Liaw, The effects of texture and extension twinning on the low-cycle fatigue behavior of a rolled magnesium alloy, AZ31B, Mater. Sci. Eng. A. 527 (2010) 7057–7067. https://doi.org/10.1016/j.msea.2010.07.047.

[55] C. Wang, T.J. Luo, J.X. Zhou, Y.S. Yang, Anisotropic cyclic deformation behavior of extruded ZA81M magnesium alloy, Int. J. Fatigue. 96 (2017) 178–184. https://doi.org/10.1016/j.ijfatigue.2016.11.020.

[56] S.M. Yin, F. Yang, X.M. Yang, S.D. Wu, S.X. Li, G.Y. Li, The role of twinning-detwinning on fatigue fracture morphology of Mg-3%Al-1%Zn alloy, Mater. Sci. Eng. A. 494 (2008) 397–400. https://doi.org/10.1016/j.msea.2008.04.056.

[57] M. Huppmann, M. Lentz, K. Brömmelhoff, W. Reimers, Fatigue properties of the hot extruded magnesium alloy AZ31, Mater. Sci. Eng. A. 527 (2010) 5514–5521. https://doi.org/10.1016/j.msea.2010.05.036.

[58] Y. Xiong, X. Gong, Y. Jiang, Effect of initial texture on fatigue properties of extruded ZK60 magnesium alloy, Fatigue Fract. Eng. Mater. Struct. 41 (2018) 1504–1513. https://doi.org/10.1111/ffe.12792.

[59] Y. Xiong, Y. Jiang, Cyclic deformation and fatigue of rolled AZ80 magnesium alloy along different material orientations, Mater. Sci. Eng. A. 677 (2016) 58–67. https://doi.org/10.1016/j.msea.2016.09.031.

[60] J. Albinmousa, H. Jahed, S. Lambert, Cyclic behaviour of wrought magnesium alloy under multiaxial load, Int. J. Fatigue. 33 (2011) 1127–1139. https://doi.org/10.1016/j.ijfatigue.2011.01.009.

[61] D. Hou, T. Liu, L. Luo, L. Lu, H. Chen, D. Shi, Twinning behaviors of a rolled AZ31 magnesium alloy under multidirectional loading, Mater. Charact. 124 (2017) 122–128. https://doi.org/10.1016/j.matchar.2016.11.046.

[62] Y. Xiong, Q. Yu, Y. Jiang, Multiaxial fatigue of extruded AZ31B magnesium alloy, Mater. Sci. Eng. A. 546 (2012) 119–128. https://doi.org/10.1016/j.msea.2012.03.039.

[63] F. Yang, S.M. Yin, S.X. Li, Z.F. Zhang, Crack initiation mechanism of extruded AZ31 magnesium alloy in the very high cycle fatigue regime, Mater. Sci. Eng. A. 491 (2008) 131–136. https://doi.org/10.1016/j.msea.2008.02.003.

[64] S.G. Hong, S. Hyuk Park, Y.H. Huh, C. Soo Lee, Anisotropic fatigue behavior of rolled Mg-3AI-1Zn alloy, J. Mater. Res. 25 (2010) 966–971. https://doi.org/10.1557/jmr.2010.0123.

[65] Y.J. Wu, R. Zhu, J.T. Wang, W.Q. Ji, Role of twinning and slip in cyclic deformation of extruded Mg-3%Al-1%Zn alloys, Scr. Mater. 63 (2010) 1077–1080. https://doi.org/10.1016/j.scriptamat.2010.08.008.

[66] F. Lv, F. Yang, Q.Q. Duan, Y.S. Yang, S.D. Wu, S.X. Li, Z.F. Zhang, Fatigue properties of rolled magnesium alloy (AZ31) sheet: Influence of specimen orientation, Int. J. Fatigue. 33 (2011) 672–682. https://doi.org/10.1016/j.ijfatigue.2010.10.013.

[67] A.A. Roostaei, H. Jahed, Role of loading direction on cyclic behaviour characteristics of AM30 extrusion and its fatigue damage modelling, Mater. Sci. Eng. A. 670 (2016) 26–40. https://doi.org/10.1016/j.msea.2016.05.116.

[68] P. Liu, Y.C. Xin, Q. Liu, Plastic anisotropy and fracture behavior of AZ31 magnesium alloy, Trans. Nonferrous Met. Soc. China (English Ed. 21 (2011) 880–884. https://doi.org/10.1016/S1003-6326(11)60797-8.

[69] T.S. Srivatsan, S. Vasudevan, M. Petraroli, The tensile deformation and fracture behavior of a magnesium alloy, J. Alloys Compd. 461 (2008) 154–159. https://doi.org/10.1016/j.jallcom.2007.07.061.

[70] Y.Z. Lit, Q.D. Wang, W.J. Ding, X.Q. Zeng, Y.P. Zhu, Fracture behavior of AZ91 magnesium alloy, Mater. Lett. 44 (2000) 265–268. https://doi.org/10.1016/S0167-577X(00)00041-0.

[71] N.S. Prasad, N. Naveen Kumar, R. Narasimhan, S. Suwas, Fracture behavior of magnesium alloys - Role of tensile twinning, Acta Mater. 94 (2015) 281–293. https://doi.org/10.1016/j.actamat.2015.04.054.

[72] J. Kang, D.S. Wilkinson, R.K. Mishra, J.D. Embury, E. Essadiqi, A. Javaid, Microstructural aspects of damage and fracture in AZ31 sheet materials, J. Mater. Eng. Perform. 22 (2013) 1386–1395. https://doi.org/10.1007/s11665-012-0399-5.

[73] M.J. Nemcko, D.S. Wilkinson, On the damage and fracture of commercially pure magnesium using x-ray microtomography, Mater. Sci. Eng. A. 676 (2016) 146–155. https://doi.org/10.1016/j.msea.2016.08.095.

[74] S.H.M. Azghandi, M. Weiss, B.D. Arhatari, J. Adrien, E. Maire, M.R. Barnett, A rationale for the influence of grain size on failure of magnesium alloy AZ31: an in situ X-ray microtomography study, Acta Mater. 200 (2020) 619–631. https://doi.org/10.1016/j.actamat.2020.09.016.

[75] Q. Ma, H. El Kadiri, A.L. Oppedal, J.C. Baird, M.F. Horstemeyer, M. Cherkaoui,

Twinning and double twinning upon compression of prismatic textures in an AM30 magnesium alloy, Scr. Mater. 64 (2011) 813–816. https://doi.org/10.1016/j.scriptamat.2011.01.003.

[76] T. Al-Samman, G. Gottstein, Room temperature formability of a magnesium AZ31 alloy: Examining the role of texture on the deformation mechanisms, Mater. Sci. Eng. A. 488 (2008) 406–414. https://doi.org/10.1016/j.msea.2007.11.056.

[77] D. Ando, J. Koike, Y. Sutou, Relationship between deformation twinning and surface step formation in AZ31 magnesium alloys, Acta Mater. 58 (2010) 4316–4324. https://doi.org/10.1016/j.actamat.2010.03.044.

[78] P. Cizek, M.R. Barnett, Characteristics of the contraction twins formed close to the fracture surface in Mg-3Al-1Zn alloy deformed in tension, Scr. Mater. 59 (2008) 959–962. https://doi.org/10.1016/j.scriptamat.2008.06.041.

[79] M.R. Barnett, Twinning and the ductility of magnesium alloys. Part II. "Contraction" twins, Mater. Sci. Eng. A. 464 (2007) 8–16. https://doi.org/10.1016/j.msea.2007.02.109.

[80] M. Lentz, M. Risse, N. Schaefer, W. Reimers, I.J. Beyerlein, Strength and ductility with {10 11}-{1012} double twinning in a magnesium alloy, Nat. Commun. 7 (2016) 1–7. https://doi.org/10.1038/ncomms11068.

[81] D. Ando, J. Koike, Y. Sutou, The role of deformation twinning in the fracture behavior and mechanism of basal textured magnesium alloys, Mater. Sci. Eng. A. 600 (2014) 145–152. https://doi.org/10.1016/j.msea.2014.02.010.

[82] M.R. Barnett, Twinning and the ductility of magnesium alloys. Part I: "Tension" twins, Mater. Sci. Eng. A. 464 (2007) 1–7. https://doi.org/10.1016/j.msea.2006.12.037.

[83] J. Koike, Y. Sato, D. Ando, Origin of the anomalous {10$\bar{1}$2} twinning during tensile deformation of mg alloy sheet, Mater. Trans. 49 (2008) 2792–2800. https://doi.org/10.2320/matertrans.MRA2008283.

[84] V. Kaushik, R. Narasimhan, R.K. Mishra, Experimental study of fracture behavior of magnesium single crystals, Mater. Sci. Eng. A. 590 (2014) 174–185. https://doi.org/10.1016/j.msea.2013.10.018.

[85] S. Ishihara, Z. Nan, T. Goshima, Effect of microstructure on fatigue behavior of AZ31 magnesium alloy, Mater. Sci. Eng. A. 468–470 (2007) 214–222. https://doi.org/10.1016/j.msea.2006.09.124.

[86] C. Chen, T. Liu, C. Lv, L. Lu, D. Luo, Study on cyclic deformation behavior of extruded Mg-3Al-1Zn alloy, Mater. Sci. Eng. A. 539 (2012) 223–229. https://doi.org/10.1016/j.msea.2012.01.084.

[87] C.J. Geng, B.L. Wu, X.H. Du, Y.D. Wang, Y.D. Zhang, F. Wagner, C. Esling, Low cycle fatigue behavior of the textured AZ31B magnesium alloy under the asymmetrical loading, Mater. Sci. Eng. A. 560 (2013) 618–626. https://doi.org/10.1016/j.msea.2012.10.004.

[88] G. Kang, C. Yu, Y. Liu, G. Quan, Uniaxial ratchetting of extruded AZ31 magnesium alloy: Effect of mean stress, Mater. Sci. Eng. A. 607 (2014) 318–327. https://doi.org/10.1016/j.msea.2014.04.023.

[89] G.S. Duan, B.L. Wu, X.H. Du, X. Zhao, Y.D. Zhang, L. Zuo, C. Esling, The cyclic frequency sensitivity of low cycle fatigue (LCF) behavior of the AZ31B magnesium

alloy, Mater. Sci. Eng. A. 603 (2014) 11–22. https://doi.org/10.1016/j.msea.2014.02.074.
[90] S. Begum, D.L. Chen, S. Xu, A.A. Luo, Low cycle fatigue properties of an extruded AZ31 magnesium alloy, Int. J. Fatigue. 31 (2009) 726–735. https://doi.org/10.1016/j.ijfatigue.2008.03.009.
[91] L. Nascimento, S. Yi, J. Bohlen, L. Fuskova, D. Letzig, K.U. Kainer, High cycle fatigue behaviour of magnesium alloys, Procedia Eng. 2 (2010) 743–750. https://doi.org/10.1016/j.proeng.2010.03.080.
[92] M. Huppmann, M. Lentz, S. Chedid, W. Reimers, Analyses of deformation twinning in the extruded magnesium alloy AZ31 after compressive and cyclic loading, J. Mater. Sci. 46 (2011) 938–950. https://doi.org/10.1007/s10853-010-4838-0.
[93] F. Lv, F. Yang, S.X. Li, Z.F. Zhang, Effects of hysteresis energy and mean stress on low-cycle fatigue behaviors of an extruded magnesium alloy, Scr. Mater. 65 (2011) 53–56. https://doi.org/10.1016/j.scriptamat.2011.03.006.
[94] J. Albinmousa, H. Jahed, S. Lambert, Cyclic axial and cyclic torsional behaviour of extruded AZ31B magnesium alloy, Int. J. Fatigue. 33 (2011) 1403–1416. https://doi.org/10.1016/j.ijfatigue.2011.04.012.
[95] X.P. Zhang, S. Castagne, X.F. Luo, C.F. Gu, Effects of extrusion ratio on the ratcheting behavior of extruded AZ31B magnesium alloy under asymmetrical uniaxial cyclic loading, Mater. Sci. Eng. A. 528 (2011) 838–845. https://doi.org/10.1016/j.msea.2010.10.016.
[96] J. Ozaki, M. Yosida, S. Horibe, The effect of pre-compressive strain on the fatigue life of the AZ31 magnesium alloy, Mater. Sci. Eng. A. 604 (2014) 192–195. https://doi.org/10.1016/j.msea.2014.03.027.
[97] X.Z. Lin, D.L. Chen, Strain controlled cyclic deformation behavior of an extruded magnesium alloy, Mater. Sci. Eng. A. 496 (2008) 106–113. https://doi.org/10.1016/j.msea.2008.05.016.
[98] S. Hasegawa, Y. Tsuchida, H. Yano, M. Matsui, Evaluation of low cycle fatigue life in AZ31 magnesium alloy, Int. J. Fatigue. 29 (2007) 1839–1845. https://doi.org/10.1016/j.ijfatigue.2006.12.003.
[99] D.W. Brown, A. Jain, S.R. Agnew, B. Clausen, Twinning and detwinning during cyclic deformation of Mg alloy AZ31B, in: Mater. Sci. Forum, 2007: pp. 3407–3413.
[100] Y. Xiong, Q. Yu, Y. Jiang, An experimental study of cyclic plastic deformation of extruded ZK60 magnesium alloy under uniaxial loading at room temperature, Int. J. Plast. 53 (2014) 107–124. https://doi.org/10.1016/j.ijplas.2013.07.008.
[101] Q. Li, Q. Yu, J. Zhang, Y. Jiang, Effect of strain amplitude on tension-compression fatigue behavior of extruded Mg6Al1ZnA magnesium alloy, Scr. Mater. 62 (2010) 778–781. https://doi.org/10.1016/j.scriptamat.2010.01.052.
[102] F. Wang, J. Dong, M. Feng, J. Sun, W. Ding, Y. Jiang, A study of fatigue damage development in extruded Mg–Gd–Y magnesium alloy, Mater. Sci. Eng. A. 589 (2014) 209–216. https://doi.org/10.1016/j.msea.2013.09.089.
[103] S.H. Park, Effect of initial twins on the stress-controlled fatigue behavior of rolled magnesium alloy, Mater. Sci. Eng. A. 680 (2017) 214–220. https://doi.org/10.1016/j.msea.2016.10.093.
[104] F. Lv, F. Yang, Q.Q. Duan, T.J. Luo, Y.S. Yang, S.X. Li, Z.F. Zhang, Tensile and

low-cycle fatigue properties of Mg-2.8% Al-1.1% Zn-0.4% Mn alloy along the transverse and rolling directions, Scr. Mater. 61 (2009) 887–890. https://doi.org/10.1016/j.scriptamat.2009.07.023.

[105] S. Ghorbanpour, B.A. McWilliams, M. Knezevic, Low-cycle fatigue behavior of rolled WE43-T5 magnesium alloy, Fatigue Fract. Eng. Mater. Struct. 42 (2019) 1357–1372. https://doi.org/10.1111/ffe.12992.

[106] Y.C. Lin, X.M. Chen, Z.H. Liu, J. Chen, Investigation of uniaxial low-cycle fatigue failure behavior of hot-rolled AZ91 magnesium alloy, Int. J. Fatigue. 48 (2013) 122–132. https://doi.org/10.1016/j.ijfatigue.2012.10.010.

[107] F.A. Mirza, K. Wang, S.D. Bhole, J. Friedman, D.L. Chen, D.R. Ni, B.L. Xiao, Z.Y. Ma, Strain-controlled low cycle fatigue properties of a rare-earth containing ME20 magnesium alloy, Mater. Sci. Eng. A. 661 (2016) 115–125. https://doi.org/10.1016/j.msea.2016.03.024.

[108] K. Hazeli, H. Askari, J. Cuadra, F. Streller, R.W. Carpick, H.M. Zbib, A. Kontsos, Microstructure-sensitive investigation of magnesium alloy fatigue, Int. J. Plast. 68 (2015) 55–76. https://doi.org/10.1016/j.ijplas.2014.10.010.

[109] J.B. Jordon, J.B. Gibson, M.F. Horstemeyer, H. El Kadiri, J.C. Baird, A.A. Luo, Effect of twinning, slip, and inclusions on the fatigue anisotropy of extrusion-textured AZ61 magnesium alloy, Mater. Sci. Eng. A. 528 (2011) 6860–6871. https://doi.org/10.1016/j.msea.2011.05.047.

[110] Y. Ling, A.A. Roostaei, G. Glinka, H. Jahed, Fatigue of ZEK100-F magnesium alloy: Characterisation and modelling, Int. J. Fatigue. 125 (2019) 179–186. https://doi.org/10.1016/j.ijfatigue.2019.04.001.

[111] Y. Wang, D. Culbertson, Y. Jiang, An experimental study of anisotropic fatigue behavior of rolled AZ31B magnesium alloy, Mater. Des. 186 (2020) 108266. https://doi.org/10.1016/j.matdes.2019.108266.

[112] L. Chen, C. Wang, W. Wu, Z. Liu, G.M. Stoica, L. Wu, P.K. Liaw, Low-cycle fatigue behavior of an As-extruded AM50 magnesium alloy, Metall. Mater. Trans. A Phys. Metall. Mater. Sci. 38 A (2007) 2235–2241. https://doi.org/10.1007/s11661-007-9181-y.

[113] T.S. Shih, W.S. Liu, Y.J. Chen, Fatigue of as-extruded AZ61A magnesium alloy, Mater. Sci. Eng. A. 325 (2002) 152–162. https://doi.org/10.1016/S0921-5093(01)01411-3.

[114] A.N. Chamos, S.G. Pantelakis, G.N. Haidemenopoulos, E. Kamoutsi, Tensile and fatigue behaviour of wrought magnesium alloys AZ31 and AZ61, Fatigue Fract. Eng. Mater. Struct. 31 (2008) 812–821. https://doi.org/10.1111/j.1460-2695.2008.01267.x.

[115] K. Shiozawa, J. Kitajima, T. Kaminashi, T. Murai, T. Takahashi, Low-cycle fatigue deformation behavior and evaluation of fatigue life on extruded magnesium alloys, Procedia Eng. 10 (2011) 1244–1249. https://doi.org/10.1016/j.proeng.2011.04.207.

[116] M. Matsuzuki, S. Horibe, Analysis of fatigue damage process in magnesium alloy AZ31, Mater. Sci. Eng. A. 504 (2009) 169–174. https://doi.org/10.1016/j.msea.2008.10.034.

[117] Y. Xiong, Y. Jiang, Fatigue of ZK60 magnesium alloy under uniaxial loading, Int. J. Fatigue. 64 (2014) 74–83. https://doi.org/10.1016/j.ijfatigue.2014.02.019.

[118] S. Dong, Y. Jiang, J. Dong, F. Wang, W. Ding, Cyclic deformation and fatigue of extruded ZK60 magnesium alloy with aging effects, Mater. Sci. Eng. A. 615 (2014) 262–272. https://doi.org/10.1016/j.msea.2014.07.074.
[119] F. Castro, Y. Jiang, Fatigue of extruded AZ31B magnesium alloy under stress- and strain-controlled conditions including step loading, Mech. Mater. 108 (2017) 77–86. https://doi.org/10.1016/j.mechmat.2017.03.002.
[120] S. Dong, Q. Yu, Y. Jiang, J. Dong, F. Wang, L. Jin, W. Ding, Characteristic cyclic plastic deformation in ZK60 magnesium alloy, Int. J. Plast. 91 (2017) 25–47. https://doi.org/10.1016/j.ijplas.2017.01.005.
[121] Q. Yu, J. Zhang, Y. Jiang, Fatigue damage development in pure polycrystalline magnesium under cyclic tension-compression loading, Mater. Sci. Eng. A. 528 (2011) 7816–7826. https://doi.org/10.1016/j.msea.2011.06.064.
[122] B. Wen, F. Wang, L. Jin, J. Dong, Fatigue damage development in extruded Mg-3Al-Zn magnesium alloy, Mater. Sci. Eng. A. 667 (2016) 171–178. https://doi.org/10.1016/j.msea.2016.05.009.
[123] Z. Wang, S. Wu, G. Kang, H. Li, Z. Wu, Y. Fu, P.J. Withers, In-situ synchrotron X-ray tomography investigation on damage mechanism of an extruded magnesium alloy in uniaxial low-cycle fatigue with ratchetting, Acta Mater. 211 (2021) 116881. https://doi.org/10.1016/j.actamat.2021.116881.
[124] D.K. Xu, E.H. Han, Relationship between fatigue crack initiation and activated {1 0 1¯2} twins in as-extruded pure magnesium, Scr. Mater. 69 (2013) 702–705. https://doi.org/10.1016/j.scriptamat.2013.08.006.
[125] K. Tokaji, M. Kamakura, Y. Ishiizumi, N. Hasegawa, Fatigue behaviour and fracture mechanism of a rolled AZ31 magnesium alloy, Int. J. Fatigue. 26 (2004) 1217–1224. https://doi.org/10.1016/j.ijfatigue.2004.03.015.
[126] S. Zheng, Q. Yu, Y. Jiang, An experimental study of fatigue crack propagation in extruded AZ31B magnesium alloy, Int. J. Fatigue. 47 (2013) 174–183. https://doi.org/10.1016/j.ijfatigue.2012.08.010.
[127] D. Culbertson, Y. Jiang, An experimental study of the orientation effect on fatigue crack propagation in rolled AZ31B magnesium alloy, Mater. Sci. Eng. A. 676 (2016) 10–19. https://doi.org/10.1016/j.msea.2016.08.088.
[128] T.R. Long, C.S. Smith, Single-crystal elastic constants of magnesium and magnesium alloys, Acta Metall. 5 (1957) 200–207.
[129] G. Simmons, Single crystal elastic constants and calculated aggregate properties, 1965.
[130] P.G. Partridge, The crystallography and deformation modes of hexagonal close-packed metals, Metall. Rev. 12 (1967) 169–194.
[131] M.H. Yoo, Slip, twinning, and fracture in hexagonal close-packed metals, Metall. Trans. A. 12 (1981) 409–418. https://doi.org/10.1007/BF02648537.
[132] J. Koike, Enhanced deformation mechanisms by anisotropic plasticity in polycrystalline Mg alloys at room temperature, Metall. Mater. Trans. A Phys. Metall. Mater. Sci. 36 (2005) 1689–1696. https://doi.org/10.1007/s11661-005-0032-4.
[133] O. Muránsky, D.G. Carr, P. Šittner, E.C. Oliver, In situ neutron diffraction investigation of deformation twinning and pseudoelastic-like behaviour of extruded AZ31 magnesium alloy, Int. J. Plast. 25 (2009) 1107–1127.

https://doi.org/10.1016/j.ijplas.2008.08.002.
[134] S.R. Agnew, D.W. Brown, C.N. Tomé, Validating a polycrystal model for the elastoplastic response of magnesium alloy AZ31 using in situ neutron diffraction, Acta Mater. 54 (2006) 4841–4852. https://doi.org/10.1016/j.actamat.2006.06.020.
[135] L. Jiang, J.J. Jonas, R.K. Mishra, A.A. Luo, A.K. Sachdev, S. Godet, Twinning and texture development in two Mg alloys subjected to loading along three different strain paths, Acta Mater. 55 (2007) 3899–3910. https://doi.org/10.1016/j.actamat.2007.03.006.
[136] X. Zhu, Y. Wang, L. Carneiro, H. Wang, Y. Jiang, Evaluation of elastic-viscoplastic self-consistent models for a rolled AZ31B magnesium alloy under monotonic loading along five different material orientations and free-end torsion, J. Magnes. Alloy. (2021). https://doi.org/10.1016/j.jma.2021.07.023.
[137] T. Mukai, M. Yamanoi, H. Watanabe, K. Ishikawa, K. Higashi, Effect of grain refinement on tensile ductility in ZK60 magnesium alloy under dynamic loading, Mater. Trans. 42 (2001) 1177–1181.
[138] Q. Yu, J. Zhang, Y. Jiang, Q. Li, An experimental study on cyclic deformation and fatigue of extruded ZK60 magnesium alloy, Int. J. Fatigue. 36 (2012) 47–58. https://doi.org/10.1016/j.ijfatigue.2011.08.016.
[139] F. Wang, M. Liu, J. Sun, M. Feng, L. Jin, J. Dong, Y. Jiang, Effects of initial {10-12} twins on cyclic deformation and fatigue of magnesium alloy at low strain amplitudes, Mater. Charact. 149 (2019) 118–123. https://doi.org/10.1016/j.matchar.2019.01.017.
[140] J. Albinmousa, M.J. Adinoyi, N. Merah, Multiaxial fatigue of extruded ZK60 magnesium alloy, Fatigue Fract. Eng. Mater. Struct. 42 (2019) 2276–2289. https://doi.org/10.1111/ffe.13048.
[141] L.H. Song, B.L. Wu, L. Zhang, X.H. Du, Y.N. Wang, Y.D. Zhang, C. Esling, Cyclic deformation behaviors of AZ31B magnesium alloy in two different asymmetric loading manners, Mater. Sci. Eng. A. 689 (2017) 134–141. https://doi.org/10.1016/j.msea.2017.02.046.
[142] Y. Xiong, Microstructure damage evolution associated with cyclic deformation for extruded AZ31B magnesium alloy, Mater. Sci. Eng. A. 675 (2016) 171–180. https://doi.org/10.1016/j.msea.2016.08.043.
[143] A.H. Pahlevanpour, S.B. Behravesh, S. Adibnazari, H. Jahed, Characterization of anisotropic behaviour of ZK60 extrusion under stress-control condition and notes on fatigue modeling, Int. J. Fatigue. 127 (2019) 101–109. https://doi.org/10.1016/j.ijfatigue.2019.05.030.
[144] J.J. Jonas, S. Mu, T. Al-Samman, G. Gottstein, L. Jiang, E. Martin, The role of strain accommodation during the variant selection of primary twins in magnesium, Acta Mater. 59 (2011) 2046–2056. https://doi.org/10.1016/j.actamat.2010.12.005.
[145] S. Godet, L. Jiang, A.A. Luo, J.J. Jonas, Use of Schmid factors to select extension twin variants in extruded magnesium alloy tubes, Scr. Mater. 55 (2006) 1055–1058. https://doi.org/10.1016/j.scriptamat.2006.07.059.